GOETHE UNIVERSITY FRANKFURT

MASTER'S THESIS

Investigation of Intermolecular Coulombic Decay in small hydrogen bonded systems

---

Author:
Jonathan NEFF

Assessor:
Prof. Dr. Reinhard DÖRNER

Second Assessor:
PD Dr. Till JAHNKE

Supervisor at LBNL:
Dr. Thorsten WEBER

A thesis submitted in fulfilment of the requirements
for the degree of Master of Science

in the

Experimental Atomic Physics Group
Department of Nuclear Physics

July 10, 2016

Declaration of Authorship

Erklärung nach §30 Absatz 12 der Ordnung für den Bachelor- und den Masterstudiengang Physik der Johann Wolfgang Goethe-Universität vom 24.04.2013

Hiermit erkläre ich, Jonathan NEFF, dass ich die vorliegende Arbeit selbständig und ohne Benutzung anderer als der angegebenen Quellen und Hilfsmittel verfasst habe. Alle Stellen der Arbeit, die ich wörtlich oder sinngemäß aus Veröffentlichungen oder aus anderen fremden Texten entnommen habe, sind von mir als solche kenntlich gemacht worden. Ich habe die Arbeit nicht, auch nicht auszugsweise, für eine andere Prüfung verwendet.

Signed: ______________________________

Date: ______________________________

Acknowledgements

At first, I want to thank my professor Reinhard Dörner for accepting me to the Experimental Atomic Physics Group at Frankfurt University. Already during my studies and work at Max-Planck Institute for Nuclear Physics in Heidelberg I heard a lot about his work which finally convinced me to begin my master studies in Frankfurt. I am grateful to him for having given me the opportunity to go to Berkeley, where I not only had a great time doing research, but also traveling and enjoying one of the best places in the world. With his supportive character and pleasant personality, Reinhard creates an atmosphere every single member of the group enjoys working in thereby making the group so successful as it is today.

I am grateful to Thorsten Weber, my supervisor at Lawrence Berkeley National Laboratory. He accepted me to his international group, organized the invitation and made all other necessary arrangements. Thanks to his critical questions concerning the data analysis, I learned to work accurately and structured which in hindsight was crucial to the success of my work. He gave me the opportunity to attend two beamtimes at the Advanced Light Source so that I did not have to work in front of the computer the whole time.

Without the instructive help of Bishwanat Gaire regarding the data analysis I certainly would have not made noticeable progress during my stay in Berkeley. His door was always open for questions and fruitful discussions about physics.

I would like to thank Averell Gatton for showing me how to effectively code in C++. His ideas and advice helped me to overcome the challenge of implementing the numerical momentum calculation.

I want to thank my second assessor Till Jahnke for his help with *lmf2root* and proofreading the thesis. Whenever I had a question it was a pleasure to ask Till. “ Don’t panic! Things will be fine.” always turned out to be a good advice.

Markus Schöffler is an exceptional member of the Experimental Atomic Physics Group. With his charisma he motivates students to keep being interested in physics. The first beamtime that I attended was at SOLEIL in France. Markus acquainted me with the setup of a COLTRIMS experiment and patiently explained to me each of its components.

I thank Achim Czasch for solving all the problems I had with *lmf2root*. He knows *lmf2root* like the back of his hand. Thus, he was able to precisely answer all my question regarding the billion lines of code.

I am particularly grateful to Natalie Segercrantz. She made my stay in California unforgetful. Whether running on the fire trail, relaxing in Dolores park while eating Bi-Rite ice cream or clubbing in Las Vegas, we always had a great time. Back in Germany, she supported me in writing the thesis by keeping pushing me whenever I got stuck. Due to her expertise in academic writing she was able to give valuable advice. I appreciate all the endurance she showed and hope that at some point I will have the chance to return the favor. Thank you, Natalie!

Last but not least, I am grateful to my parents, my sister and my brother for always having supported me no matter what I did. Their persistent support and trust are the foundation of all my achievements.

Contents

List of Figures

List of Tables

List of Abbreviations

QM	**Q**uantum **M**echanics
ICD	**I**ntermoleculer/-atomic **C**oulombic **D**ecay
TS1	**T**wo **S**tep **1**
TS2	**T**wo **S**tep **2**
LCOA	**L**inear **C**ombination (of) **A**tomic **O**rbitals
HF	**H**artree **F**ock
BO	**B**orn **O**ppenheimer (approximation)
DFT	**D**ensity **F**unctional **T**heory
PI	**P**hoto **I**onization
FC	**F**ranck **C**ondon (factor/principle)
IV	**O**uter **V**alence
OV	**I**nner **V**alence
KER	**K**inetic **E**nergy **R**elease
ALS	**A**dvanced **L**ight **S**ource
ToF	**T**ime-**o**f-**F**light
MCP	**M**icro **C**hannel **P**late
TDC	**T**ime (to) **D**igital **C**onverter
PIPICO	**P**hoto**I**on **P**hoto**I**on **CO**incidence
FWHM	**F**ull **W**idth **H**alf **M**aximum
DIP	**D**ouble **I**onization **P**otential
SIP	**S**ingle **I**onization **P**otential

Physical Constants

Speed of Light	$c = 2.997\,924\,58 \times 10^{8}\,\mathrm{m\,s^{-1}}$
Elementary charge	$e = 1.602\,176\,620\,8 \times 10^{-19}\,\mathrm{A\,s}$
Reduced Planck constant	$\hbar = 1.054\,571\,800 \times 10^{-34}\,\mathrm{J\,s}$
Electric constant	$\varepsilon_0 = 8.854\,187\,817 \times 10^{-12}\,\mathrm{C\,V^{-1}\,m^{-1}}$
Bohr radius	$a_0 = 5.291\,772\,109\,2 \times 10^{-11}\,\mathrm{m}$
Electron mass	$m_\mathrm{e} = 9.109\,382\,91 \times 10^{-31}\,\mathrm{kg}$
Proton mass	$m_\mathrm{p} = 1.672\,621\,777 \times 10^{-27}\,\mathrm{kg}$
Fine-structure constant	$\alpha = 7.297\,352\,569\,8 \times 10^{-3} \approx \frac{1}{137}$
Rydberg energy	$Ry = 13.60569253\mathrm{eV}$
Boltzmann constant	$k_\mathrm{B} = 1.380\,648\,52 \times 10^{-23}\,\mathrm{J\,K^{-1}}$

To my family…

Chapter 1

Introduction

1.1 Motivation

"ICD appears everywhere" – This statement, initially made by Ouchi et al. [1], reflects the current consensus in the field of atomic and molecular physics regarding the recently discovered intermolecular Coulombic decay (ICD). First theoretically predicted in 1997 by Cederbaum, Zobeley, and Tarantelli [2], ICD was verified in various experimental studies as a radiationless decay mechanism of weakly bound clusters (e.g. [3], [4]). During this process, an inner-valence vacancy, which was created after photoionization, is refilled by an outer-valence electron from the same atom. The energy thereby released is transferred via a virtual photon to the neighboring molecule, which uses it to emit one of its outer-valence electrons. The system remains in a doubly ionized state and subsequently undergoes a Coulomb explosion. When ICD is energetically allowed meaning that the single and double ionization potentials of the system are arranged correspondingly, its efficiency depends on the number of available decay channels. Hence, ICD turns out to be a very efficient and prominent decay mechanism, in particular in complex molecular systems such as Van der Waals bonded or hydrogen bonded clusters. Since most molecules in nature are compounded with other neighboring molecules thereby allowing intermolecular interaction, ICD indeed seems to appear everywhere.

Beside its prevalent occurrence in a manifold of molecular systems, ICD is also relevant due to its potential effect on biological systems. The electrons emitted upon de-excitation during ICD are generally low-energy (secondary) electrons which are proven to play a decisive role in most relevant chemical key processes associated with radiation chemistry, environmental chemistry, and chemical synthesis [5–8]. Consequently, after photoionization of a larger molecular system, ICD can initiate further mechanisms thereby causing complex chemical damage in secondary reactions. Therefore, studying ICD is not only important for a detailed understanding of certain photoionization mechanisms but is of great interest for photochemistry and radiation damage.

In order to explore the relevance of ICD in biochemical environments, firstly the ICD process needs to be investigated in isolated systems that represent common types of hydrogen bondings between biochemically relevant systems such as water and ammonia. ICD strongly depends on the energy levels in these clusters and on the internuclear distance of the atoms participating in the decay. Thus, the composition and structure of the cluster have a direct influence on quantities that can be experimentally observed, such as the fragmentation rates, the energy spectrum of the emitted ICD electrons and the kinetic energy release of the ionic fragments.

Secondly, it is important to understand how the molecular environment affects the likelihood of certain decay mechanisms occurring in these small hydrogen bonded systems. Recently, it was shown theoretically that protonation and deptrotonation of ammonia clusters alter the electronic structure of the system so that ICD is enhanced or terminated, respectively [9]. This result nourishes the presumption that in nature the production of low energy electrons, which are essential to biochemical processes, is controlled through changes of the molecular environment of the corresponding system.

The experiment presented in this thesis is dedicated to the investigation of the different decay mechanisms of the isolated hydrogen bonded systems $NH_3 \cdots NH_3$ and $NH_3 \cdots H_2O$, in particular the intermolecular Coulombic decay. Theoretical calculations have shown that the double ionization potentials of both systems happen to lie above the inner-valence single ionization potential of the nitrogen and oxygen, respectively [9, 10]. Hence, the clusters are not only energetically allowed to decay through double ionization but also to undergo ICD. By using the Cold Target Recoil Ion Momentum Spectroscopy (COLTRIMS) technique the 3d-momenta of both emitted electrons and two fragment ions of the cluster can be measured simultaneously. Thereby, it is possible to isolate different molecular breakup channels. Moreover, the responsible decay mechanisms can be identified by measuring their energetics, examining the nuclear dynamics of the recoiling ions of the dimers and exploring the emission angular distribution of the electrons.

1.2 Structure of the thesis

The thesis is structured into four major parts. In the first part, Chapter 2, theoretical background information is given. Although many effects in atomic physics can approximately be treated semiclassically, the structure of atomic systems must be described quantum mechanically. Therefore, the basics of the quantum mechanical description of atomic and molecular systems are introduced. Thereafter, the models of different mechanisms of interaction between light and matter are discussed. Finally, the characteristics of the target systems $NH_3 \cdots NH_3$ and $NH_3 \cdots H_2O$ and their energetic structure is presented.

The experiment was performed at the synchrotron Advanced Light Source (ALS) at Lawrence Berkeley National Laboratory at beamline 10.0.1. Hence, a brief introduction of the production of synchrotron light and its characteristics, which are important for the success of the experiment, is given in Chapter 3. In addition, the COLTRIMS technique and its components are explained in detail.

In Chapter 4 the data analysis is presented step by step. To obtain the initial 3d-momenta of each particle from their time-of-flight from the reaction zone onto the detector and the information of the position of their impact on the detector, several calculations need to be performed. The correctness of these calculations is ensured by a thorough calibration of the spectrometer. For that purpose, the well understood energetics of the single photoionization of helium and the double ionization of the nitrogen molecule with subsequent fragmentation serve as a reference. In order to account for inhomogeneities in the electric field of the spectrometer the standard analytical approach of the momentum calculation must be modified into a numerical procedure. After the calibration, the data is presorted thereby reducing the data significantly. Taking advantage of momentum conservation in a ionic fragmentation, the reactions of interest are identified by applying corresponding conditions on the time-of-flight of the recoil ions.

Finally, the results of the data analysis are presented in Chapter 5. The energetics of the identified breakups including electron energies, emission angular distributions and kinetic energy release of the ionic fragments are discussed by comparing these results with either previous measurements or *ab initio* calculations. Furthermore, corresponding conclusions are drawn. In addition to the investigation of the identified breakups, the molecular composition of the gas jet is examined and discussed.

Chapter 2

Theoretical Background

The following chapter provides theoretical background information that is useful to understand the experiment, the data analysis and the conclusions which are drawn. First, a short overview is given on how quantum mechanics (QM) is used to describe atoms and molecules. QM is one of the most successful theories in physics. The theory is capable, for instance, to completely describe the hydrogen atom disregarding effects of quantum electrodynamics and quantum field theory. However, already for a system of slightly higher complexity consisting of one nucleus and two electrons an analytical solution does not exist anymore. Therefore in order to understand and explain the dynamics, that are studied in the field of atomic and molecular physics, approximations are needed. The most important ones are discussed briefly in the following sections. Furthermore, different mechanisms of interaction between light and matter are explained, in particular the intermolecular Coulombic decay (ICD). The characteristics of the ammonia dimer $NH_3 \cdots NH_3$ and ammonia water dimer $NH_3 \cdots H_2O$ are discussed, in particular with respect to their geometrical and electronic structure.

2.1 Quantum mechanics

2.1.1 Fundamental basics

The development of quantum mechanics in the beginning of the 20th century changed the view of the world from the perspective of physics radically. The theory states, that the motion of a particle can no longer be described by certain coordinates in space-time, which means that a prediction of its trajectory (i.e. motion in space-time) is not possible given the equations of motion. This profound perception even one of the greatest physicists of modern history, Albert Einstein, struggled to accept.[1] Instead, according to QM the motion and properties of a particle can be characterized as a state by a space- and time-dependent wave function $\Psi(\vec{r},t)$ which only determines the probability of a particle being in a certain volume element at a certain time.

The basics of QM are derived from first principles using abstract mathematical concepts which are called Dirac formalism named after the British physicist Paul Dirac. All possible states $|\Psi\rangle$ of a system are considered as elements of an infinitely dimensional linear vector space, the so called Hilbert space $\mathscr{H}$. Each state can be constructed by a complete set of orthonormal basis vectors $|\Psi\rangle = \sum_n c_n |\phi\rangle$ with complex numbers $c_n = \langle c_n | \Psi \rangle$.[2] Furthermore operators (linear transformations) $\hat{A} = \sum_j a_j |a_j\rangle\langle a_j|$, that act on states, are defined. The vectors $|a_j\rangle$ represent the complete orthonormal set of eigenvectors of $\hat{A}$, and a_j are the corresponding eigenvalues. In order to predict experimental findings using QM a link between theory and experiment must be

---

[1] With his famous quote "God doesn't play dice" Albert Einstein expressed his discontent with quantum mechanics undermining classical determinism.

[2] For a continuous basis the sum must be replaced with an integral.

established. The following postulates allow a physical interpretation of quantum theory to be made [11, chapter 3.3]:

1. Each measuring instrument for a specific physical variable corresponds to a linear, hermitian operator[3].
2. A pure state is represented by a vector $|\Psi\rangle$ in Hilbert space $\mathscr{H}$.
3. The measurement (i.e. an interaction between the system and the instrument) corresponds to an operator $\hat{A}$ acting on the state $|\Psi\rangle$: $\hat{A}|\Psi\rangle = \sum_j a_j |a_j\rangle\langle a_j|\Psi\rangle = |a_n\rangle\langle a_n|\Psi\rangle$.
4. The result of a measurement is the eigenvalue a_j of the operator A.
5. The probability to measure a_j is given by $p(a_j|\Psi) = |\langle a_j|\Psi\rangle|^2$.
6. The time evolution of a pure state $|\Psi(t)\rangle$ is given by the time dependent Schrödinger equation:
$$i\hbar\frac{\partial}{\partial t}|\Psi(t)\rangle = \hat{H}(t)|\Psi(t)\rangle \tag{2.1}$$

As one of the central elements in atomic physics, the Schrödinger equation is used for calculating electronic states in atoms and molecules. The operator $\hat{H}(\vec{r},t)$ on the right side of Equation 2.1 is the Hamilton operator. By analogy with the Hamiltonian in classical mechanics, it is the sum of kinetic and potential energy $\hat{H} = \hat{T} + \hat{V}$. However, since $\hat{T}$ in QM is an operator, the momentum p in $T = \frac{p^2}{2m}$ has to be replaced with the corresponding operator $\hat{p} = -i\hbar\vec{\nabla}$ (correspondence principle[4]). For a particle with mass m in a potential $V(\vec{r})$ the Schrödinger equation is an inhomogeneous differential equation of second order:

$$i\hbar\frac{\partial}{\partial t}|\Psi(\vec{r},t)\rangle = \left(-\frac{\hbar^2}{2m}\nabla^2 + V(\vec{r})\right)|\Psi(\vec{r},t)\rangle \tag{2.2}$$

For stationary problems, where momentum and energy do not depend on time, the wave function is chosen as $\Psi(\vec{r},t) = \Psi(\vec{r})f(t)$ thereby separating the differential equation into a time-dependent and a space-dependent part. The general solution for the time-dependent part turns out to be $f(t) = exp(-\frac{i}{\hbar}Et)$ with the constant total energy E. The space-dependent part is then:

$$E|\Psi(\vec{r})\rangle = \left(-\frac{\hbar^2}{2m}\nabla^2 + V(\vec{r})\right)|\Psi(\vec{r})\rangle\ . \tag{2.3}$$

The expression $exp(-\frac{i}{\hbar}Et)$ is called phase factor. It only affects the phase of the wave function so that the probability $|\Psi|^2$ remains constant.

2.1.2 Quantum mechanical description of atoms

The Hydrogen atom

The hydrogen atom is the simplest atomic system and the only system that has an analytical solution to the Schrödinger equation. Hence, it serves as paradigm for systems of higher complexity.

---

[3] An operator $\hat{A}$ is hermitian if it has the property $\hat{A} = \hat{A}^+$ with $\hat{A}^+$ the adjoint operator.

[4] In the context of QM often also referred to as Bohr's correspondence principle. The principle states that the behavior of systems in QM corresponds to classical physics in the limit of large quantum numbers.

To solve the Schrödinger equation describing the complete hydrogen atom (i.e. electron and proton) the relative motion is separated from the motion of the center of mass by making a corresponding transformation of the coordinate system.[5] While the solution for the center of mass turns out to be a simple plain wave, the relative part does not have such a simple solution. Its Hamiltonian contains the radially symmetric Coulomb potential $V(r) = -\frac{e^2}{r}$:

$$E|\Psi(\vec{r})\rangle = \left(-\frac{\hbar^2}{2\mu}\nabla^2 + V(r)\right)|\Psi(\vec{r})\rangle, \tag{2.4}$$

where μ denotes the reduced mass and $\vec{r}$ the relative coordinates in the center of mass system (CMS). In spherical coordinates the wave function $\Psi(r,\vartheta,\varphi) = R(r)\Theta(\vartheta)\Phi(\varphi)$ is used to solve the radial, azimuthal and polar part of the wave function separately.[6] The wave function of a particle with mass μ and charge e in the Coulomb potential is found to be

$$\Psi_{n,l,m}(r,\vartheta,\varphi) = R_{n,l}(r)Y_l^m(\vartheta,\varphi)\ . \tag{2.5}$$

The radial part of the wave function $R_{n,l}$ is described by the *Laguerre Polynomials* which are proportional to $r^l exp(-\frac{r}{a_0 n}) \cdot \text{Polynom}(r)$. They are normalized to one and vanish for $r \longrightarrow \infty$, thus ensuring the local character of the bound particle. $Y_l^m(\vartheta,\varphi)$ are the surface spherical harmonics. They form an orthonormal set of functions which means that $\int_0^{2\pi}\int_0^{\pi} Y_{l_1}^{m_1} Y_{l_2}^{m_2} d\vartheta d\varphi = 1$ for $m_1 = m_2$ and $l_1 = l_2$, else 0. The shape of the probability density $|\Psi|^2$ depends on the numbers l and m.

Quantum numbers and orbitals

Within Schrödinger's theory each electronic state is distinctly characterized by three quantum numbers n, l and m. The principal quantum number $n \in \mathbb{N}$ specifies the energy $E_n = -\frac{\mu e^4}{8\varepsilon_0 h^2 n^2}$. For each energy eigenvalue E_n, which can be obtained by calculating the expectation value of the Hamilton operator $\langle\Psi_n|\hat{H}|\Psi_n\rangle$, there are $\sum_{l=0}^{n-1}(2l+1) = n^2$ different states Ψ_n, thus E_n is degenerated. Transitions between states with different quantum numbers $n_1 \longrightarrow n_2$ correspond to an absorption or emission of a photon with energy $\Delta E = E_2 - E_1 = Ry(\frac{1}{n_1} - \frac{1}{n_2})$. Here, Ry denotes the Rydberg energy[7]. By calculating these state transitions the spectral series of hydrogen, such as the Balmer-, Paschen or Back-series, can be explained.

The azimuthal quantum number l is associated with the angular momentum operator $\hat{l}(\vec{r})$ by its expectation value $\langle\Psi_{n,l}|\hat{l}^2|\Psi_{n,l}\rangle = l(l+1)\hbar^2$. It mainly defines the shape of the probability density. Its possible values $l = 0,1,2,...,n-1$ are limited by the principal quantum number. One-electron wave functions characterized by l are called atomic orbitals.

The magnetic quantum number $-l \leq m \leq l$ is defined by the orientation of the angular momentum relative to the quantization axis which is usually the z-axis. The z-component of the angular momentum operator $\hat{l}_z$ corresponds to measuring the projection of $\vec{l}$ on the quantization axis z. Its expectation value is $\langle\Psi_{n,l,m}|\hat{l}_z|\Psi_{n,l,m}\rangle = m\hbar$. In the presence of an external magnetic field the degenerated energy levels for given values n and l split into $2m+1$ different levels. This phenomenon is called the Zeeman effect. The summation of all wave functions for a given

---

[5] A detailed approach can be found in standard literature, e.g. [12, p.145ff].

[6] Details can be found in [12, p.133ff].

[7] $Ry = \frac{\mu e^4}{8\varepsilon_0^2 h^2} \approx 13.6eV$ is the energy that is needed to lift the electron in hydrogen from the ground state ($n = 0$) into the continuum.

principal quantum number $\Psi_n = \sum_{0\leq l\leq n-1}\sum_{-l\leq m\leq l}\Psi_{n,l,m}$ yields to a state n which always has a spherically symmetric probability density. These states are therefore often called shell.

Shell model and nomenclature for one-electron systems

As it turned out, Schrödinger's theory does not fully describe the structure of the hydrogen atom. In fact, there is noticeable discrepancy between experimental results and theoretical predictions. For example, the state energies not only seem to depend on the principal quantum number n but also on the azimuthal quantum number l. The missing piece in the puzzle of QM was found by Paul Dirac. He predicted the existence of the spin $\vec{s}$, which is often referred to as an internal magnetic moment of elementary particles. Relative to the quantization axis the spin can only have two possible directions, up and down. Its z-component is $s_z = \pm\frac{\hbar}{2}$, with the spin quantum number $m_s = \pm\frac{1}{2}$. This quantization was first verified by Stern and Gerlach in 1921, who discovered that neutral silver atoms passing an inhomogeneous magnetic field were deflected in different directions depending on their total spin moment. Taking the spin moment into account, a spin-orbit interaction can be derived resulting in a shift in the energy levels by a term proportional to $\vec{l}\cdot\vec{s}$. This splitting is called fine structure. Due to the coupling of angular and spin momentum neither of the two quantities is conserved anymore, instead their sum $\vec{j} = \vec{l}+\vec{s}$ is now conserved. With the total momentum operator $\hat{j}$ the new magnetic quantum number $m_j = m_l + m_s$ with values $-j \leq m_j \leq j$ is obtained. With this set of quantum numbers n, j, m_j the electronic states are able to be completely described using the following notation:

$$nl_j \quad \text{for example} \quad 2p_{\frac{1}{2}} \, .$$

For historical reasons $l = s, p, d, ...$ are used for the symbol of the angular momentum.

Atoms with more electrons

For atoms with N electrons the wave function Ψ depends on the coordinates of all electrons $r_1, r_2, ..., r_N$. In addition to the kinetic energy and Coulomb potential between electron and nucleus, the Hamiltonian also includes all kind of interactions between the electrons themselves:

$$\hat{H} = \hat{T}_{\mathrm{e}} + \hat{V}_{\mathrm{ke}} + \hat{V}_{\mathrm{ee}} + \hat{V}_{ss} + \hat{V}_{ll} + \hat{V}_{sl} \, , \tag{2.6}$$

with

- the kinetic energy of the electrons:

$$\hat{T}_{\mathrm{e}} = \sum_{i=1}^{N}\left(-\frac{\hbar^2}{2m}\vec{\nabla}^2\right) \tag{2.7}$$

- the Coulomb attraction between nucleus and electrons:

$$\hat{V}_{\mathrm{ke}} = -\sum_{i=1}^{N}\frac{Ze^2}{r_i} \tag{2.8}$$

- the Coulomb repulsion between the electrons:

$$\hat{V}_{\mathrm{ee}} = \sum_{i=1}^{N}\sum_{j=1}^{i-1}\frac{e^2}{r_{ij}} \tag{2.9}$$

- the spin-spin interaction:

$$\hat{V}_{ss} = \frac{e^2}{m^2} \sum_{i=1}^{N} \sum_{j=1}^{i-1} \left(\frac{\vec{\sigma}_i \vec{\sigma}_j}{r_{ij}^3} - 3 \frac{(\vec{\sigma}_i \vec{r}_{ij})(\vec{\sigma}_j \vec{r}_{ij})}{r_{ij}^5} \right) \tag{2.10}$$

- the interaction between the angular momenta:

$$\hat{V}_{ll} = \sum_{i=1}^{N} \sum_{j=1}^{i-1} c_{ij} (\vec{l}_i \cdot \vec{l}_j) \tag{2.11}$$

- the interaction between spin and angular momentum:

$$\hat{V}_{sl} = -\frac{1}{2m^2c^2} \sum_{i=1}^{N} \frac{1}{r_i} \frac{dV(r)}{dr_i} (\vec{s}_i \cdot \vec{l}_j) \tag{2.12}$$

Because of their relatively small contribution, to the total energy the spin-spin interaction $\hat{V}_{ss}$, the interaction between angular momenta $\hat{V}_{ll}$ and the interaction between spin and angular momentum $\hat{V}_{sl}$ can be neglected in further considerations. The Hamiltonian reduces to:

$$\hat{H} = \hat{T}_{\mathrm{e}} + \hat{V}_{\mathrm{ke}} + \hat{V}_{\mathrm{ee}} \; . \tag{2.13}$$

An analytical solution of the Schrödinger equation for a system with more than one electron does not exist because the electron-electron interaction is not spherically symmetric. Therefore, for solving the equation for a many-body systems, approximations have to be made. The solution can be calculated either numerically based on the exact Hamiltonian $\hat{H}$ from Equation 2.13 or analytically based on an adjusted Hamiltonian.

In the **model of independent electrons** the interactions between the electrons is accounted for by calculating a spherically symmetric effective potential $V_{\mathrm{eff}}(r)$ for each electron. The Hamiltonian can then be written as the sum of all single Hamiltonians:

$$\hat{H} = \hat{H}_1 + \hat{H}_2 + ... + \hat{H}_N \; . \tag{2.14}$$

The total wave function is chosen as the product of all single electron wave functions. Taking the Pauli principle into account, which states that the total electronic wave function must be antisymmetric under commutation of two electrons, the wave function is written in form of the Slater determinant

$$\Psi(\vec{r}) = \frac{1}{\sqrt{N!}} \begin{vmatrix} \Psi_1(\vec{r}_1)\Upsilon_1(\vec{s}_1) & \cdots & \Psi_1(\vec{r}_N)\Upsilon_1(\vec{s}_N) \\ \vdots & \ddots & \vdots \\ \Psi_N(\vec{r}_1)\Upsilon_N(\vec{s}_1) & \cdots & \Psi_N(\vec{r}_N)\Upsilon_N(\vec{s}_N) \end{vmatrix} \tag{2.15}$$

with $\Upsilon_i(\vec{s}_i)$ denoting the spin. Using the Slater determinant allows the Schrödinger equation to be separated into N one-particle problems with corresponding analytical solutions. Consequently, the total energy of the system is given by the sum of all single energies

$$E = E_1 + E_2 + ... + E_N \; . \tag{2.16}$$

The difficulty in this model is to derive the effective potential V_{eff} since the wave functions $\Psi_i(\vec{r}_i)$ and the probability densities, respectively, are unknown.

A common approach to calculate electronic states and energies in multi-electron systems is the Hartree-Fock (HF) method. This method is an iterative process in which the wave functions Ψ_i and corresponding energies E_i are repeatedly calculated until they converged within a given acceptance range. In each loop for each electron the so called shielding potential is calculated using the wave functions of all other electrons. For example the effective potential for electron i in the first loop is calculated as follows:

$$V_{\text{eff}}^{(1)}(r_i) = -e^2 \left(\frac{Z}{r_i} - \sum_{i \neq j} \int \frac{|\Psi_i^{(0)}(\vec{r}_i)|^2}{r_{ij}} d\tau_j \right) . \tag{2.17}$$

The corresponding wave function is then obtained by solving the one-particle Schrödinger equation:

$$i\hbar \frac{\partial}{\partial t} |\Psi_i^{(1)}(\vec{r}_i)\rangle = \left(-\frac{\hbar^2}{2m} \nabla^2 + V_{\text{eff}}^{(1)}(\vec{r}_i) \right) |\Psi_i^{(1)}(\vec{r}_i)\rangle . \tag{2.18}$$

The shielding potentials are calculated in the order of descending binding energies of the electrons.

Nomenclature for multi-electron systems

Although the interaction terms $\hat{V}_{ss}$, $\hat{V}_{ll}$ and $\hat{V}_{sl}$ in Equation 2.6 can be neglected when solving the Schrödinger equation, they play an important role in how to describe the electronic state of the atom. In light atoms, such as nitrogen or oxygen, the interaction between spin and angular momentum $\hat{V}_{sl}$ of each electron i is weaker than the spin-spin interaction $\hat{V}_{ss}$ and the interaction between angular momenta $\hat{V}_{ll}$. As a consequence all electron spins $\vec{s}_i$ couple and the total spin of the system becomes the vectorial sum $\vec{S} = \vec{s}_1 + \vec{s}_2 + ... + \vec{s}_N$ with its absolute value $\vec{S}^2 = \vec{S}(\vec{S}+1)\hbar^2$. Analogously the angular momenta $\vec{l}_i$ add up to the total orbital angular momentum $\vec{L} = \vec{l}_1 + \vec{l}_2 + ... + \vec{l}_N$. Its absolute value is $\vec{L}^2 = \vec{L}(\vec{L}+1)\hbar^2$. Together both vectors form the total angular momentum $\vec{J} = \vec{L} + \vec{S}$ which is also assigned to the number $\vec{J}^2 = \vec{J}(\vec{J}+1)\hbar^2$. Since $\vec{L}$ and $\vec{S}$ are well defined, both can be measured at the same time meaning that L, S and J respectively are good quantum numbers fully describing the atom. This type of angular momentum coupling is called LS coupling (or Russell-Saunders coupling) and only holds for light atoms. For heavy atoms with high nuclear charge Z the interaction between spin and angular momentum V_{sl} of each electron is dominant. Hence, the angular momenta $\vec{j}_i$ combine and form $\vec{J}$, whereas the total orbital momentum $\vec{L}$ is not anymore defined. This so called jj coupling is not further discussed here. For describing the electronic states of a multi-electron system usually the following term symbols are used:

$$n^{2S+1}L_J \quad \text{for example} \quad 2^4S_{\frac{3}{2}} .$$

Its components are explicitly explained in Table 2.1

2.1.3 Quantum mechanical description of molecules

Schrödinger equation for molecules

In order to describe molecules quantum mechanically, the Hamilton operator in Equation 2.13 must be expanded the by kinetic energy of K nuclei $\hat{T}_{\text{k}}$ and their Coulomb interaction $\hat{V}_{\text{kk}}$. Whereas the potential energy only depends on the relative position of the particles, the kinetic energy varies depending on the chosen coordinate system. In order to consider a stationary molecule usually the CMS is chosen as a coordinate system that moves with the molecule in

Table 2.1: Quantum numbers for characterizing atoms with more than one electron.

n	is the energy level of the outermost electron located in the valence shell.
$2S+1$	is called the (spin) multiplicity and indirectly denotes the total spin.
L	stands for the total orbital momentum. Instead of numbers $0,1,2...$ the symbols $S,P,D,...$ are used.
J	denotes the total angular momentum. For an even number of electrons it is an integral number, for an odd number of electrons a half-integral, respectively.

space. However, because observables, such as the energy, are measured in the laboratory system, in the following theoretical consideration the molecule is simply assumed to be fixed in space. The complete Hamiltonian then reads as follows:

$$\begin{aligned}\hat{H} &= \hat{T}_{\mathrm{e}} + \hat{T}_{\mathrm{k}} + \hat{V}(\vec{r},\vec{R}) \qquad (2.19)\\ &= -\frac{\hbar^2}{2m}\sum_{i=1}^{N}\vec{\nabla}_i^2 - \frac{\hbar^2}{2}\sum_{k=1}^{K}\frac{1}{M_k}\vec{\nabla}_k^2 + \hat{V}(\vec{r},\vec{R})\,,\end{aligned}$$

where $\vec{r}$ stands for the coordinates of electrons $\vec{r}_1,...,\vec{r}_N$ and $\vec{R}$ for those of the nuclei $\vec{R}_1,...,\vec{R}_K$, respectively. The potential energy $\hat{V}$ is composed of three contributions

$$\begin{aligned}\hat{V}(\vec{r},\vec{R}) &= \hat{V}_{\mathrm{ke}} + \hat{V}_{\mathrm{ee}} + \hat{V}_{\mathrm{kk}} \qquad (2.20)\\ &= e^2\left(-\sum_{k=1}^{K}\sum_{i=1}^{N}\frac{Z_k}{r_{i,k}} + \sum_{i'>i}\sum_{i=1}^{N}\frac{1}{r_{i',i}} + \sum_{k'>k}\sum_{k=1}^{K}\frac{Z_{k'}Z_k}{R_{k',k}}\right),\end{aligned}$$

with $r_{i',i} = |\vec{r}_i - \vec{r}_{i'}|$ and $R_{k',k} = |\vec{R}_k - \vec{R}_{k'}|$. This Hamiltonian is an exact description for non-rotating molecules fixed in space, if all types of angular momentum and spin interaction between electrons and nuclei are neglected. The corresponding Schrödinger equation can then in principle be solved in two ways:

1. The Schrödinger equation can be solved numerically, yet this approach does not always turn out to be the best. Depending on the complexity of the problem and the available computational power any numerical approach can take a huge amount of time given the desired accuracy. Furthermore, estimating calculation errors and interpreting results with regards to other systems might become difficult.

2. The Schrödinger equation can be simplified by making assumptions based on physical reasoning. The advantage of this approach is that, in order to achieve higher precision of the result, the model can be adjusted successively. Since every step in the approximation has a physical meaning, this approach also helps to better understand the problem.

Adiabatic approximation

A common approximation, which is used in atomic and molecular physics, is the so called adiabatic approximation. Due to the much higher mass of the nuclei ($M \approx 1836 \cdot (Z+N) \cdot m_e$) the nuclear motion (i.e. rotation and vibration) is assumed to be notably slower than the electronic motion. The lighter electrons follow the nuclear motion adiabatically. Hence, for every given nuclear configuration $\vec{R}$ a well-defined electron distribution $\Phi^{\mathrm{el}}(\vec{r},\vec{R})$ exists. The low kinetic energy of the nuclei is then considered as a perturbation of the electronic energy so that the Hamiltonian can be written as:

$$\hat{H} = \hat{H}_0 + \hat{H} \ , \tag{2.21}$$

where $\hat{H}_0 = \hat{T}_e + \hat{V}$ and $\hat{H}' = \hat{T}_n$. The undisturbed Schrödinger equation is

$$\hat{H}_0 |\Phi^{el}(\vec{r},\vec{R})\rangle = E^{(0)}(\vec{R}) |\Phi^{el}(\vec{r},\vec{R})\rangle \ , \tag{2.22}$$

with the solutions $\Phi_n^{\mathrm{el}}(\vec{r},\vec{R})$ describing the different electron configurations for a given nuclear constellation $\vec{R}$. If the electronic wave functions are chosen $\Phi_n^{\mathrm{el}}(\vec{r},\vec{R})$ in such way, that they form an orthonormal system, each total wave function can be written as an infinite sum

$$\Psi(\vec{r},\vec{R}) = \sum_m \chi_m(\vec{R}) \Phi_m^{el}(\vec{r},\vec{R}) \ . \tag{2.23}$$

Using this total wave function in the disturbed Schrödinger equation leads to the system of coupled equations:

$$\begin{aligned} &(1) \qquad \hat{H}_0 \Phi^{\mathrm{el}}(\vec{r},\vec{R}) = E^{(0)}(\vec{R}) \cdot \Phi^{\mathrm{el}}(\vec{r},\vec{R}) \\ &(2) \quad \hat{H}' \chi_n(\vec{R}) + \textstyle\sum_m (c_{nm} \chi_m(\vec{R})) = (E - E_n^{(0)}(\vec{R})) \chi_n(\vec{R}) \ , \end{aligned} \tag{2.24}$$

with the coefficients $\chi_{nm} = \chi_{nm}(\Phi)$ depending on the electronic state Φ^{el} and thus causing the coupling between the nuclear and the electronic motion. Considering only the diagonal elements of the sum, which can be shown to be

$$c_{nn} = \sum_{k=1}^{K} \frac{\hbar^2}{2M_k} \int \left(\frac{\partial \Phi_n^{\mathrm{el}}}{\partial \vec{R}_k} \right) d\vec{r} \ , \tag{2.25}$$

Equation 2.24 can be written as

$$(\hat{H}' + \hat{U}_n(\vec{R})) \chi_n = E \cdot \chi_n \ , \tag{2.26}$$

with the potential

$$U_n'(\vec{R}) = E_n^{(0)}(\vec{R}) + \sum_{k=1}^{K} \frac{\hbar^2}{2M_k} \int \left(\frac{\partial \Phi_n^{\mathrm{el}}}{\partial \vec{R}_k} \right) d\vec{r} \ .$$

In the adiabatic approximation the electronic states do not evolve instantaneously for a given nuclear configuration but with a small delay. The potential $U_n'(\vec{R})$ is considered as the effective potential and affects the nuclear state χ_n. Therefor the nuclei feel the potential stemming from the electron distribution, however their motion does not reciprocally affect the electronic state.

Born-Oppenheimer approximation

If in addition to neglecting the non-diagonal elements in Equation 2.24 the diagonal elements c_{nn} are also set to zero, the nuclear and electronic motion decouple completely. Equation 2.24 simplifies to

$$(\hat{H}' + E_n^{(0)}(\vec{R})) \chi_n(\vec{R}) = E \cdot \chi_n(\vec{R}) \tag{2.27}$$

and the potential to

$$U_n'(\vec{R}) = E_n^{(0)}(\vec{R}) \ , \tag{2.28}$$

which is the total potential energy of the molecule (i.e. the eigenvalue of the undisturbed Hamiltonian $\hat{H}_0$ in Equation 2.22). Using the concept of a disturbed Hamiltonian the complete Schrödinger equation of a molecule separates into two independent equations describing the nuclear and the electronic motion:

$$\begin{aligned} &(1) \quad \hat{H}_0 \Phi_n^{\mathrm{el}}(\vec{r},\vec{R}) = E^{(0)}(\vec{R}) \cdot \Phi_n^{\mathrm{el}}(\vec{r},\vec{R}) \\ &(2) \quad (\hat{T}_\mathrm{k} + E_n^{(0)})\chi_n(\vec{R}) = E_{n,\nu} \cdot \chi_{n,\nu}(\vec{R}) \; . \end{aligned} \tag{2.29}$$

The function Φ_n^{el} describes the electronic state n for the given nuclear configuration $\vec{R}$. The wave function $\chi_{n,\nu}$ describes the nuclear motion for energy state ν of the nuclei given the electronic state n. Eventually, applying the Born-Oppenheimer (BO) approximation means to separate the Schrödinger using the product of the nuclear and electronic wave function as the total wave function:

$$\Psi_{n,\nu}(\vec{r},\vec{R}) = \Phi_n^{\mathrm{el}}(\vec{r}) \cdot \chi_{n,\nu}(\vec{R}) \tag{2.30}$$

In this case all interactions between the nuclear and the electronic motion are disregarded. Consequently, the total energy of the systems is composed of the kinetic energy of the nuclei $T_\mathrm{k}(\vec{R})$ and the electronic energy $E_n^{(0)}(\vec{R})$ which includes the Coulomb repulsion of all nuclei (see Equation 2.21):

$$E_{n,\nu} = T_\mathrm{k}(\vec{R}) + E_n^{(0)}(\vec{R}) \; . \tag{2.31}$$

Potential curves and nuclear dynamics

As mentioned above in the BO approximation the effective potential U', which the nuclei are moving in, is given by the total electronic energy $E_n^{(0)}(\vec{R})$, that only depends on the nuclear constellation $\vec{R} = (\vec{R}_1, ..., \vec{R}_K)$. Since the nuclear and the electronic part are considered separately, the electronic energy can be calculated for different nuclear constellations. In the simple case of a diatomic molecule the nuclear constellation $\vec{R}$ corresponds to the internuclear distance $R = |\vec{R}_2 - \vec{R}_1|$. Figure 2.1 schematically shows potential curves for different electronic states. The potential curve corresponding to the electronic state $n = 0$, also called the electronic ground state, has a minimum at R_0 and therefore depicts a binding state. In equilibrium the nuclei have an average nuclear distance of R_0. The depth of the binding potential is the zero-point energy D_e which the system is not allowed to reach due to Heisenberg's uncertainty principle. Consequently, the ground state energy including internal nuclear motion always lies slightly above zero-point energy. The energy, that is required to separate the nuclei from each other, is called the dissociation energy D_0 given by

$$D_0 = V(\infty) - V(R_0) \; . \tag{2.32}$$

An unbinding state, such as the state $n = 1$ in Figure 2.1, does not feature a minimum in the potential. The kinetic energy of the nuclei consist of a vibrational and a rotational part $T_\mathrm{k}(\vec{R}) = E_\mathrm{vib}(\vec{R}) + E_\mathrm{rot}(\vec{R})$. Thus for each electronic state there exist various vibrational states, characterized by the number $\nu = 0, 1, 2, ...$, and for each vibrational state there are different rotational states with the numbers $J = 0, 1, 2, ...$ The molecule can make a transition from the state $E_{n,\nu_i,J_j}(E_n^{\mathrm{el}}, E_\mathrm{vib}, E_\mathrm{rot})$ to $E_{m,\nu_k,J_l}(E_n^{\mathrm{el}}, E_\mathrm{vib}, E_\mathrm{rot})$ by absorbing (or emitting) a photon with the corresponding energy $h\nu = E_{nm} = E_m - E_n$. Hereby, the largest part of the energy is used for making the electronic transition, whereas for the vibrational and rotational transitions the energy is significantly smaller as can be seen in Figure 2.2. Generally the additional structure due to vibration and rotation of the nuclei forms a band system for electronic transitions. Hence,

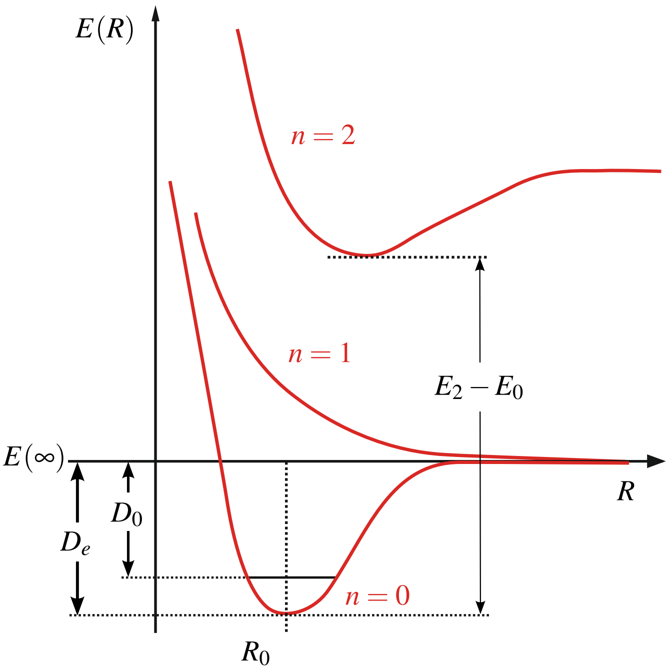

Figure 2.1: The potential energy of diatomic molecule depends on the nuclear distance R. If the molecule gains the energy $E = E_2 - E_0$, e.g. by impact of another particle or absorption of a photon, it is able to undergo an electronic transition from the ground state $n = 0$ to state $n = 2$.

measured energy values stemming from electronic transition are accompanied by uncertainty due to the additional vibrational transitions that are involved. Thus, these transitions are often referred to as "vibronic"[8] transitions. Transitions, which involve changes only of vibrational and rotational states, are abbreviated to "rovibrational"[9]. For molecules with more than two nuclei more-dimensional potential energy surfaces are considered since the constellation of the nuclei $\vec{R}$ contains further degrees of freedom. Correspondingly, the number of possible vibrational and rotational states increases and the transitions become non-trivial.

Calculation of molecular orbitals

In order to determine the electronic state of a molecule $\Phi^{\mathrm{el}}(\vec{r})$ for a given nuclear constellation $\vec{R}$, the electronic part of the Schrödinger equation has to be solved. Within the **molecular orbital theory** the electronic part of a molecule is considered as a superposition of molecular orbitals which can be illustrated as electron clouds. Thus, each electron is assigned to its own wave function $\Phi_i(\vec{r}_i, \vec{s}_i) = \phi_i(\vec{r}_i)\Upsilon_i(\vec{s}_i)$ describing its probability of presence $|\phi_i(\vec{r}_i)|^2$ and spin configuration $\Upsilon_i(\vec{s}_i)$. Since molecules consist of minimum three particles (two nuclei and one electron), the energy eigenvalues of the electric part $\Phi_n^{\mathrm{el}}(\vec{r})$ cannot be calculated analytically. Thus, approximations and numerical methods have to be considered. In principle there are two starting points where approximations can be made. On the one hand the Hamiltonian $\hat{H}$ of the system can be simplified based on reasonable assumptions, as it was for example done as part of the BO approximation in Section 2.1.3. On the other hand the electronic wave function $\Phi_n^{\mathrm{el}}(\vec{r})$ can be modified so that numeric calculations are efficiently feasible. As a first step the basis of molecular orbitals must be defined. Technically these can be random functions since only

---

[8] "Vibronic": abbreviation for electronic and vibrational.

[9] "Rovibrational": abbreviation for rotational and vibrational.

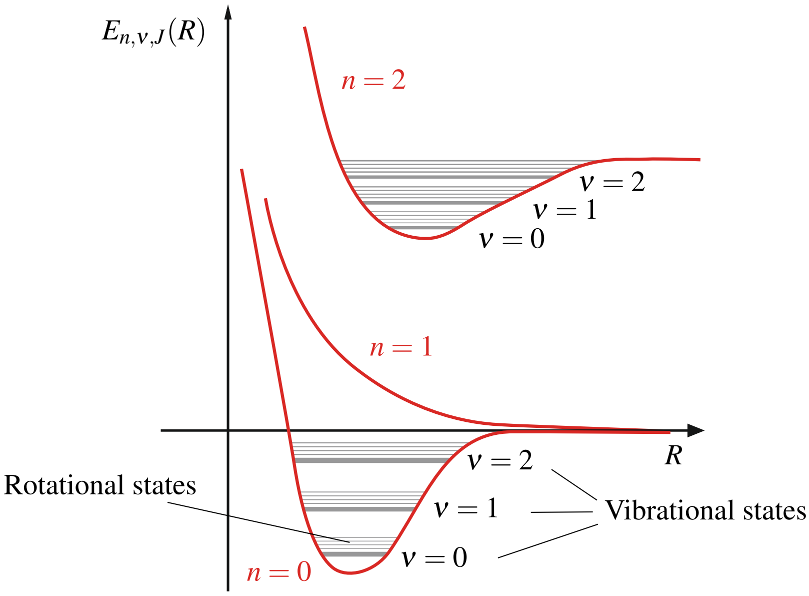

Figure 2.2: Each electronic state of a molecule consists of many vibrational and rotational states forming a band system. The energy required for transitions within these bands is much smaller compared to that required for electronic transitions.

the solution to the eigenvalue problem matters. However generally either functions with low computational costs or functions, that can be physically derived, are chosen.

Linear combination of atomic orbitals (LCAO) is a very simple approach to calculate a single molecular orbital. The idea of LCAO is that the atomic orbitals form molecular orbitals by overlapping with each other. Mathematically the orbital of a molecule with K nuclei is then described by a linear combination of K basic atomic wave functions ϕ_k^{el}. Usually analytical one-electron functions, such as the wave functions of the hydrogen atom, centered around the corresponding nucleus are used:

$$\Phi^{\text{el}} = \sum_{k=1}^{K} c_k \phi_k^{el} \, . \tag{2.33}$$

The optimal linear combination, meaning the optimal set of coefficients c_k, can be found by using the variation principle. Therefor the mean energy is derived to

$$\langle E \rangle = \langle \Phi | \hat{H} | \Phi \rangle \, , \tag{2.34}$$

with respect to the coefficients c_i and set to zero

$$\frac{\partial}{\partial c_k} \left(\int \Phi^* H \Phi d\tau \right) = 0; \qquad k = 1,2,\ldots,K \, . \tag{2.35}$$

Here, $d\tau$ denotes the infinitesimal volume element $d\tau = dr d\phi d\theta$. As a result a system of K linear equations with K unknown coefficients c_k is obtained. The equations also contain integrals of the form

$$\begin{aligned} H_{kl} = & \int \phi_k^* H \phi_l d\tau \quad \text{(Coulomb integral)} \\ S_{kl} = & \int \phi_k^* \phi_l d\tau \quad \text{(overlap integral)} \, , \end{aligned}$$

which can be calculated because the atomic wave functions ϕ_k are known. From this system of linear equations all K energy eigenvalues $E_k(\vec{R})$ and coefficients c_k for the given nuclear constellation $\vec{R}$ can be calculated. Using these results the molecular orbital Φ is conveniently constructed by combining the atomic orbitals φ_i weighted with their corresponding coefficient c_i. However, the simplicity of the method comes with a price. For certain ranges of nuclear constellations the energy eigenvalues belonging to LCAO orbitals show notable discrepancies compared with energy values which are numerically calculated for example with the HF method. These discrepancies mainly come from the fact that the distortion of the atomic orbitals by the Coulomb potential of all nuclei is not considered. Nevertheless, because of its intuitive approach and simplicity, the LCAO method remains a popular way to calculate single molecular orbitals.

For more complex molecules with a high number of electrons the LCAO method does not provide sufficient precision since it is not using more than one iteration. Nonetheless it serves well as a starting point for modern *ab initio* calculations. These numerical methods use the exact non-relativistic Hamiltonian from Equation 2.20 and an explicit set of basic molecular orbitals $\Phi_i(\vec{r}_i)^{(0)}$ in order to calculate more accurate molecular orbitals $\Phi_i(\vec{r}_i)^{(1)}$ and their corresponding energy eigenvalues $E_i(\vec{R})$. The basic assumption of these methods is to (partially) ignore the electron correlation which means to make use of the **single particle approximation**. In this case the second part of the potential energy in Equation 2.21 vanishes so that the electronic part of the potential energy only includes the Coulomb interaction between electrons and nuclei V_{ke}. The total electronic wave function for N electrons of the molecule can then be written as the product of all single-electron functions

$$\Phi_n^{\mathrm{el}}(\vec{r}) = \prod_{i=1}^{N} \Phi_i(\vec{r}_i) \tag{2.36}$$

and the Schrödinger equation separates into N partial equations, each for one electron. Consequently, the total energy is given by the sum

$$E = \sum_{i=1}^{N} \varepsilon_i \; . \tag{2.37}$$

The energy eigenvalues ε_i are now as precise as the molecular orbitals Φ_i have been constructed. If in addition the spin of the electrons is considered, the one-electron function reads

$$\Phi_i(\vec{r}_i, \vec{s}_i) = \phi_i(\vec{r}_i)\Upsilon_i(\vec{s}_i) \; . \tag{2.38}$$

As the total wave function the Slater determinant (see Equation 2.15) is used which accounts for the Pauli principle and decomposes into single-electron wave functions. As it is explained in the case of a multi-electron atom in Section 2.1.2, in each iteration step of the HF method an effective potential, that takes all other electrons with lower energy into account, is used to calculate a new single-electron wave function and energy eigenvalue. Since the effective potential is calculated by the average shielding of all lower energetic electrons using their probability of presence (compare Equation 2.17), the HF method does not consider the full electron correlation meaning the dynamic interaction between the electrons.

To account for the electron correlation the numerical approach was improved by developing the method **Configuration interaction (CI)** which is a variational method combined with Hartree-Fock. The total molecular wave function is expressed as a linear combination of different Slater determinants which are chosen by physical reasoning with respect to symmetry:

$$\Phi^{el} = \sum_k a_k \Phi_k \; . \tag{2.39}$$

Each Slater determinant is called configuration state function and is itself a linear combination of one-electron functions, e.g. Slater functions $\Psi = N \cdot r^n e^{-\alpha r} Y_l^m(\theta,\phi)$. These configurations Φ_k are optimized with the HF method. Finally, the variational principle

$$\frac{\partial}{\partial c_k} \langle \Phi^{el} | \hat{H} | \Phi^{el} \rangle = 0 \tag{2.40}$$

is used to find the optimal coefficients c_k and determine the most suitable total molecular function.

Another method, that accounts for electron correlation but uses perturbation theory instead of variational calculus, is the **Second order Møller–Plesset (MP2) perturbation theory**. The original Hamiltonian describing kinetic and potential energy of all electrons

$$\hat{H} = -\frac{\hbar^2}{2m} \sum_{i=1}^{N} \vec{\nabla}_i^2 + \hat{V}(\vec{r},\vec{R}) \tag{2.41}$$

is split into undisturbed and disturbed Hamiltonian

$$\hat{H} = \underbrace{\hat{F} + \langle \Phi | \hat{H} - \hat{F} | \Phi \rangle}_{\hat{H}^0} + \underbrace{\hat{H} - \hat{F} - \langle \Phi | \hat{H} - \hat{F} | \Phi \rangle}_{\hat{H}^1} \ , \tag{2.42}$$

where $\hat{F}$ is the Fock operator with the single electron wave function as eigenfunction with the property $\hat{F}|\Phi_i\rangle = \varepsilon_i |\Phi_i\rangle$. Following the concept of perturbation theory the eigenstates and eigenvalues are developed into a series of λ determining the perturbation:

$$\hat{H} = \hat{H}^{(0)} + \lambda \hat{H}^{(1)} \tag{2.43}$$

$$E = E^{(0)} + \lambda E^{(1)} + \lambda^{(2)} + ... \tag{2.44}$$

$$|\Phi\rangle = |\Phi^{(0)}\rangle + \lambda |\Phi^{(1)}\rangle + \lambda^2 |\Phi^{(2)}\rangle + ... \tag{2.45}$$

In MP2 perturbation theory the series is stopped after the second order. Nevertheless, in order to achieve higher precision further terms may be considered. The undisturbed energy eigenvalue $E^{(0)}$ in Equation 2.44 equals the energy $E_{HF} = 2\sum_i^{N/2} \varepsilon_i$ of the system obtained by the HF method

$$E_{MP0} = E^{(0)} = \langle |\Phi^{(0)} | \hat{H}1(0) | \Phi^{(0)} \rangle = H_{HF} \tag{2.46}$$

$$E_{MP1} = \langle |\Phi^{(0)} | \hat{H}1(1) | \Phi^{(0)} \rangle = 0 \tag{2.47}$$

$$E_{MP2} = \frac{1}{4} \sum_{i,j,a,b} \frac{|\langle \varphi_i \varphi_j | \hat{H}^{(1)} | \varphi_a \varphi_b \rangle|^2}{\varepsilon_i + \varepsilon_j - \varepsilon_a - \varepsilon_b} \ . \tag{2.48}$$

In MP2 perturbation theory only the second order makes a meaningful correction to the energy values of zero$^{\text{th}}$ order. Hereby all interactions between the electrons of occupied orbitals i, j and unoccupied (virtual) orbitals a, b are taken into account.

Compared to all previous methods the **Density Functional Theory (DFT)** follows a fundamentally different approach. Instead of using state functions the DFT uses the concept of functionals.

The central element is the spatially dependent electron density [13, 14]

$$\eta(\vec{r}) = N \int |\Phi^{\mathrm{el}}(\vec{r})|^2 d\vec{r} \tag{2.49}$$

normalized by the factor N which is given by the wave function Φ^{el}. It can be shown that in theory the ground-state wave function Φ_0^{el} can be calculated by using only the corresponding ground-state density $\eta_0(\vec{r})$ [15]. In the functional theory this means that for Φ_0^{el} a unique functional $\Phi[\eta_0]$ exists. Hence, there also exists a functional for the ground energy

$$E_0 = E[\eta_0] = \langle \Phi[\eta_0] | \hat{T} + \hat{V} | \Phi[\eta_0] \rangle \; . \tag{2.50}$$

Solving the so-called Kohn-Sham equations

$$\left(-\frac{\hbar^2}{2m} \vec{\nabla}^2 + V_{\mathrm{eff}} \vec{r} \right) \Phi_i(\vec{r}) = \varepsilon_i \Phi_i(\vec{r}) \tag{2.51}$$

yields to the orbitals Φ_i. The effective one-particle potential

$$V_{\mathrm{eff}}(\vec{r}) = V_0(\vec{r}) + \int \frac{e^2 \eta(\vec{r'})}{|\vec{r'} - \vec{r}} d\vec{r'} + V_{\mathrm{xc}}(\eta(\vec{r})) \tag{2.52}$$

consists of the extern potential V_0 describing the attraction between nuclei and electrons, the repulsion among the electrons, described by the second term, and an exchange-correlation potential V_{xc} that includes all non-classical interactions among the electrons. Because the exchange-correlation potential V_{xc} depends on the density η, which depends on the wave function Φ, that in turn depends on the potential V_{xc}, the solution to the Kohn-Sham equation is self-consitent and can be found in an iterative process. The density functional theory is popular in the field of quantum chemistry since it leads to more precise results while requiring less computational power than post-Hartree-Fock approximations. The disadvantage of DFT is, that it can be very difficult to find an expression for V_{xc} which is suitable to the problem.

Quantum numbers and nomenclature

In molecules the spherical symmetry of the potential is broken, so that the usual atomic quantum numbers n, m_l, m_s and m_j neither appropriately determine the states of single electrons nor the total electronic state of the molecule. However, in the simple case of diatomic, homonuclear molecules the molecular axis, that connects both nuclei, defines a new symmetry of the system. Thus, the projections of physical quantities, such as angular momentum $\vec{L}$, spin $\vec{S}$ and $\vec{J}$ onto the new axis are conserved, hence represent good quantum numbers. For describing electronic states of diatomic molecules a structure similar to the atomic nomenclature is used. The state of single electrons are characterized with the following term symbols, which are exemplified in detail in Table 2.2:

$$n\lambda_{u/g} \quad \text{for example} \quad 2\sigma_g \; .$$

The total electronic state of a molecule takes all electrons into consideration, so that the total orbital momentum is given by $\vec{L} = \sum_i \vec{l}_i$ and the total spin by $\vec{S} = \sum_i \vec{s}_i$. In analogy to the nomenclature of atomic states, for molecular states the following term symbols are used:

$$N^{2S+1}\Lambda^{(+/-)}_{\Omega,(g/u)} \quad \text{for example} \quad X^2\Pi^+_{1/2} \; .$$

Table 2.3 gives a detailed explanation for each component of the term symbol.

Table 2.2: Quantum numbers for characterizing the state of a single electron (i.e. molecular orbital) in a linear diatomic molecule.

n	labels the energy level $1,2,3,...$ of the electron.
λ	declares the projection of the angular momentum $\vec{l}$ on molecular axis with values $\lambda = 0,1,2,... \equiv \sigma,\pi,\delta,....$[10]
g/u	indicates the symmetry behavior of the wave function under inversion of the coordinates at the center of charge $\hat{I}\|\Psi(\vec{r})\rangle = \Psi(\vec{-r})\rangle$. The molecular orbital is even if $\hat{I}\|\Psi(\vec{r})\rangle = \|\Psi(\vec{r})\rangle$ and odd if $\hat{I}\|\Psi(\vec{r})\rangle = -\|\Psi(\vec{r})\rangle$. Inversion at the center of charge is a symmetry operation only for homonuclear diatomic molecules.

2.1.4 Types of molecular bonds

Condensed matter consists of atoms formed to clusters and crystals. Although the only origin of bonding is the Coulomb interaction between electrons and protons, different types of bonds are distinguished. In the context of the presented experiment three of the bond types are briefly described in the following section.

Covalent bond

In the case of a covalent bond the bonding partners build one or more mutual electron pairs that interact with the nuclei. Hereby, the valence orbitals are rearranged in order to increase the electron density between both partners. The covalent bond is the strongest bond between atoms. Examples for crystals, that form covalent bonds, are carbon or silicon.

Hydrogen bond

Hydrogen bonds are formed when atoms with high electronegativity bonds with a H atom which is covalently bond to another atom. If the second atom approaches the hydrogen, the spacial density of its electron can expand to both atoms so that the H^+ acts like a bridge. The hydrogen bond plays an important role e.g. in biological systems.

Van der Waals bond

If the outermost shell of an atom is filled so that the valence electrons are bound strongly, the spatial electron density cannot easily be deformed under the influence of another atom. Hence, the atoms do not build up a bonding molecular orbital by rearranging as it is done in covalent bonds. Instead, due to the Coulomb repulsion of the negative electron orbitals the total electron density of both atoms is slightly shifted relatively to the positive charge of the nuclei,

---

[10] In a linear diatomic molecule, that does not rotate, the energy only depends on $|\lambda|$. Hence, the projection quantum number λ has only positive values.

[11] In this context the symbol Σ denotes the absolute value of the total spin $|\vec{S}| = |\sum_i \vec{s}_i|$.

Table 2.3: Quantum numbers for characterizing the total electronic state of a molecule.

N	labels the energy level. Usually $N = X$ is used for the ground state and $N = A, B, ...$ for the following excited states.
S	is the spin quantum number which is used to calculate the spin multiplicity $2S+1$. Depending on the spin multiplicity $1, 2, 3, ...$ the state is called singlet, doublet, triplet, etc. The projection of the total spin $\vec{S}$ on the molecular axis is labeled with $\Sigma = M_S = -S, -S+1, ..., S-1, S$.[11]
Λ	is the projection quantum number $\lvert M_L \rvert$ which declares the projection of the total orbital momentum $\vec{L}$ on the molecular axis. Its range is $\Lambda = 0, 1, 2, ... \equiv \Sigma, \Pi, \Delta, ...$.
Ω	is the projection of the total angular momentum $\vec{J} = \vec{L} + \vec{S}$ on the molecular axis with the range $\Omega = \lvert M_J \rvert = 0, \frac{1}{2}, ..., J-1, J$. If the spin-orbit coupling is weak, $\vec{L}$ and $\vec{S}$ are decoupled and Ω is given by the sum of each projections $\Omega = \lvert \Lambda + \Sigma \rvert$ instead.
(g/u)	describes the behavior of the molecule under inversion of the coordinates at the center of charge. This operation is applicable for homonuclear diatomic molecules only.
$(+/-)$	denotes the parity of the electronic wave function. The parity of a wave function Ψ describes its behavior under reflection on a plane perpendicular to the molecular axis. Hence, a molecular state can have positive parity if $\hat{\sigma} \lvert \Psi^+ \rangle = \lvert \Psi^+ \rangle$ or negative parity if $\hat{\sigma} \lvert \Psi^- \rangle = - \lvert \Psi^- \rangle \ ,$ with the parity operator $\hat{\sigma}$. This symmetry operation is only applicable on diatomic molecules.

thereby inducing dipole moments which start to attract each other. If the atoms get closer so that the orbitals overlap, the Coulomb repulsion of the nuclei dominates and the force becomes repulsive. For two atoms or molecules, that are Van der Waals bonded, the potential is described by the empirical Lennard-Jones potential

$$V(r_{ij}) \propto \frac{a}{r_{ij}^{12}} - \frac{b}{r_{ij}^{6}} , \tag{2.53}$$

where a and b are constants and $r_{ij} = |\vec{r}_j - \vec{r}_i|$ is the distance between the atoms or molecules.

2.2 Interaction between light and matter

Light can interact with matter in different ways. It can scatter from electrons, it can be absorbed or emitted by atoms and it even can transform into matter by for example creating a pair consisting of an electron and a positron. Before quantum theory was developed, light has been considered as a continuous electromagnetic wave. With this classical understanding many phenomenon such as diffraction, interference or polarization of light could be explained. However the theory of electromagnetism reaches its boundaries when it comes to the interaction between light and matter. A well known example is the photoelectric effect. When light hits a metallic surface, it deposits energy which allows valence electrons to escape from the potential of the atomic lattice. According to the classical theory light transfers its energy in a continuous way. Hence, the maximum kinetic energy of the released electrons is expected to increase with the intensity of the light. Experiments showed that an increased intensity leads to a higher number of photoelectrons, yet their maximum kinetic energy stays the same. Instead it turns out, that the maximum energy, which is transferred to a single electron, solely depends on the frequency ν of the light. Quantum theory considers light as quantized and each quantum, called photon, carries the energy $E = h\nu$. Assuming that only one photon can interact with an electron at a time the phenomenon of the photoelectric effect can be understood. The maximum kinetic energy of a released electron is then described by the equation

$$E_{\text{kin,max}} = h\nu - W , \tag{2.54}$$

where W denotes the energy which is required to remove an electron from the surface of the metal. The intensity of the light is interpreted as the photon density which explains the increased number of photoelectrons at higher intensities. The process of a single atom or molecule emitting an electron due to photon absorption is called photoionization. If the photon energy is lower than the binding energy of the electron, the photon can still be absorbed and used for excitation, if

$$h\nu = E_2 - E_1 . \tag{2.55}$$

This process can also be reversed. In most cases an excited atom has the possibility to de-excite by emitting a photon with the energy given by the difference of the binding energies E_1 and E_2 of the two involved states.

In order to describe these emission and absorption processes quantum mechanically the time dependent Schrödinger equation (see Equation 2.1) of a charged particle in the electromagnetic field is considered. The Hamiltonian is then given as [16]:

$$H(t) = -\frac{1}{2m}(\vec{p} - e\vec{A})^2 - V(\vec{r}) . \tag{2.56}$$

According to the correspondence principle, the position representation of $\vec{p}$ equals the operator $-i\hbar\vec{\nabla}$ and the Hamiltonian reads

$$H(t) = -\frac{\hbar^2}{2m}\vec{\nabla}^2 - i\hbar\frac{e}{2m}(\vec{\nabla}\vec{A}+\vec{A}\vec{\nabla}) + \frac{e}{2m}^2\vec{A}^2 - V(\vec{r}) \ , \tag{2.57}$$

with $V_{\vec{r}}$ expressing the Coulomb potential of the nucleus and the vector potential $\vec{A}$ describing the radiation field. Since the electrodynamics are invariant under gauge transformations, the Coulomb gauge ($\vec{\nabla}\vec{A} = 0$) can be chosen, which leads to

$$H(t) = \underbrace{-\frac{\hbar^2}{2m}\vec{\nabla}^2 - V(\vec{r})}_{H_0}\underbrace{-(i\hbar\frac{e}{2m}\vec{A}\vec{\nabla} - \frac{e^2}{2m}\vec{A}^2)}_{H_{\text{int}}(t)} \ . \tag{2.58}$$

This simpler form of the Hamiltonian consists of a time independent part H_0 and a time dependent part $H_{\text{int}}(t)$ describing the interaction between the electron and the electromagnetic field. Photons with sufficient energy to induce electronic transitions in atoms are classically considered as weak electromagnetic fields so that the term $\vec{A}^2$ is negligible compared to $\vec{A}$. Generally the field of the photon is also much weaker than the Coulomb field of the nucleus, so that the interaction Hamiltonian $H_{\text{int}}(t)$ can be considered as a small perturbation of H_0. Using time dependent perturbation theory the integrated cross section of absorption

$$\sigma_{i\to f} = \frac{4\pi^2\alpha\hbar^2}{m^2\omega_{fi}}|M_{fi}(\omega_{fi})|^2\delta(E_f - E_i - h\nu) \tag{2.59}$$

can be derived. Furthermore, the transition rate $W_{i\to f}$, i.e. the probability per unit time, of a quantum mechanical system going from the initial state $|i\rangle$ to a final state $|f\rangle$

$$W_{i\to f} = \frac{2\pi}{\hbar}|M_{fi}|^2\delta(E_f - E_i) \ , \tag{2.60}$$

which is known as Fermi's golden rule, is obtained. The transition matrix element M_{fi} in the first order of time dependent perturbation theory is

$$M_{fi} = \langle f|\hat{H}_{\text{int}}|i\rangle \quad \text{, with} \quad H_{int} = -i\hbar\frac{e}{2m}\vec{A}\vec{\nabla} \ . \tag{2.61}$$

In order to quantify quantities such as the transition rate or integrated cross sections the matrix element must be calculated.

2.2.1 Photoionization

In the process of photoionization illustrated in Figure 2.3 a photon with energy $h\nu$ is absorbed by an atom or a molecule thereby inducing the emission of an electron. The kinetic energy of the removed electron is given by

$$E_{\text{kin}} = h\nu - E_{\text{bind}} \ , \tag{2.62}$$

with E_{bind} the binding energy of the electron. Since momentum conservation must be fulfilled, a negligibly small part of the energy is also transfered to the recoil ion. To describe photoionization with the tools of quantum mechanics a general pulse of radiation is considered so that the vector potential is given by

$$\vec{A} = \vec{\varepsilon}\int_0^\infty A_0(\omega)cos(\vec{k}\cdot\vec{r} - \omega t + \delta_w)d\omega \ . \tag{2.63}$$

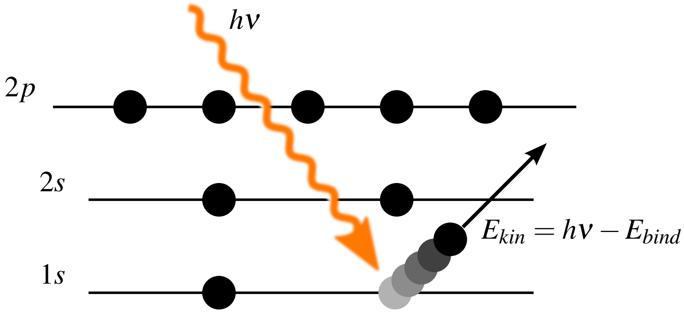

Figure 2.3: In the process of photoionization a photon is absorbed by transferring its energy $h\nu$ to an electron which subsequently is emitted. The kinetic energy of the free electron is given by $E_{\text{kin}} = h\nu - E_{\text{bind}}$.

With first order perturbation theory the matrix element derives to

$$M_{fi} = \langle f|exp(i\vec{k}\cdot\vec{r})\vec{\varepsilon}\cdot\vec{\nabla}|i\rangle \ . \tag{2.64}$$

In order to solve this integral another important approximation of atomic physics, which is called the dipole approximation, is used. The typical photon energy for optical transitions and ionizations is associated with wavelengths of $\lambda \approx 10^{-6}\,\text{m}$ or $k = 2\pi/\lambda \approx 10^{5}\,\text{m}^{-1}$. Atomic orbitals usually extend over distances of the order of $10^{-10}\,\text{m}$ so that the product is $\vec{k}\cdot\vec{r} \ll 1$. This justifies the expansion of the exponential term into a Taylor series

$$exp(i\vec{k}\cdot\vec{r}) = 1 + (i\vec{k}\cdot\vec{r}) + \frac{1}{2!}(i\vec{k}\cdot\vec{r})^2 + ... \tag{2.65}$$

and to stop after the 0^{th}-order. Physically the dipole approximation neglects the linear momentum which represents the direction of the photon. Thus, in the laboratory system all cross sections depend only on angles with respect to the polarization vector but not with respect to the direction of the photon. Switching back to momentum representation $\vec{\nabla} \to (i\hbar)^{-1}\vec{p}$ and using the Heisenberg equation of motion[12] for the matrix element

$$M_{fi} = \frac{mE_{fi}}{e}\vec{\varepsilon}\cdot\vec{D}_{fi} \tag{2.66}$$

is obtained, where $D_{fi} = -e\vec{r}_{fi}$ is the dipole operator. Considering linearly polarized photons, e.g. into the z-direction, the matrix element simplifies to

$$M_{fi} = -mE_{fi}d_{fi} \ , \tag{2.67}$$

where $d_{fi} = \langle f|z|i\rangle$ is called the dipole matrix element. The simplest case of photoionization is the K-shell ionization exciting a 1s-electron into the continuum. The continuum wave function of an electron with wave vector $\vec{k}$ can be expressed as an expansion into partial waves [17]:

$$\Phi_{km_s}(\vec{r}) = \frac{1}{k}\sum_{l,m} i^l e^{-i\Delta_l} Y^{+}_{lm}(\vec{k}) R_{k,l} Y_{lm}(\theta,\phi) \Upsilon^{m_s}_{1/2} \ . \tag{2.68}$$

---

[12] Using $\dot{\vec{r}} = (i\hbar)^{-1}[\vec{r}, H_0]$ the relation $\langle f|\dot{\vec{r}}|i\rangle = \langle f|\vec{r}H_0 - H_0\vec{r}|i\rangle = -(i\hbar)^{-1}(E_f - E_i)\langle f|\vec{r}|i\rangle$ can be derived.

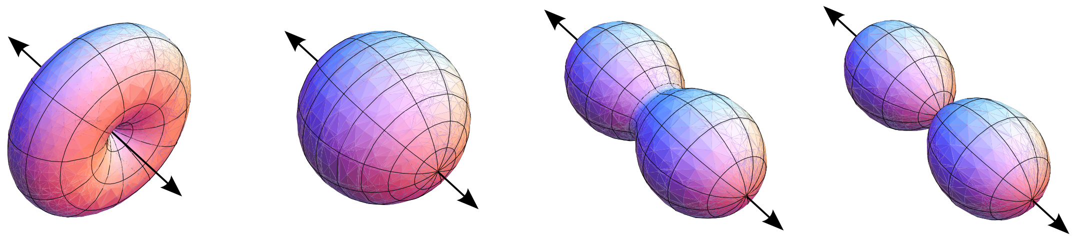

$\beta = -1$ $\beta = 0$ $\beta = 1$ $\beta = 2$

Figure 2.4: Angular distribution of a photoelectron in spherical coordinates for different values of β according to Equation 2.71. The arrows indicate the polarization direction of the photon.

Δ_l is the phase shift due to the Coulomb potential, $R_{k,l}$ is the radial part of the wave function and $\Upsilon^{m_s}_{1/2}$ describes the spin configuration. The dipole matrix element is written as

$$d_{fi} = \langle \Phi_{km_s}|z|\Psi_{1s}\rangle = \frac{1}{\sqrt{k}}\sum_{l,m}(-i)^l e^{i\Delta_l} Y_{lm}(\vec{k})\frac{1}{\sqrt{3}}R_{\varepsilon p,1s}\int Y^*_{lm}(\theta,\phi)Y_{10}(\theta,\phi)d\Omega \,, \tag{2.69}$$

where $R_{\varepsilon,1s}$ describes the weighted overlap of the radial parts $\langle R_{k,l}|r|R_{1s}\rangle$ and ε denotes the kinetic energy of the electron in the continuum. The integral over the two spherical harmonics represents the selection rules that hold for electronic transitions. The orthogonality condition of spherical harmonics requires $l = 1$ and $m = 0$ for the integral not to vanish. In general, if a bound electron is ejected by a photon, the resulting transition is $nl_i \to \varepsilon l_f$ with $l_f = l_i \pm 1$, hence the parity of the wave function switches. The magnetic quantum number m_l remains unchanged.[13] Using the dipole matrix element described by Equation 2.69 and Fermi's golden rule described in Equation 2.60 the partial cross section of photoionization of an 1s-electron

$$\frac{d\sigma}{d\Omega}(\theta) = 4\pi^2\alpha E_{fi}k|d_{fi}|^2 = 2\pi\alpha E_{\text{kin}}R_{\varepsilon p,1s}cos^2\theta \tag{2.70}$$

is obtained within the framework of the dipole approximation. For the purpose of experimental quantification the partial cross section of photoionization

$$\frac{d\sigma}{d\Omega}(\theta) = \frac{\sigma}{4\pi}(1+\beta P_2(cos\theta)) \tag{2.71}$$

is considered. The β-parameter, with values from -1 to 2, was introduced in order to describe the anisotropy of the angular distribution. $P_2(cos\theta)$ is the second Legendre polynomial and σ denotes the integrated cross section. Figure 2.4 shows the partial cross section for different values of β. In case of ionizing an 1s-electron, an angular distribution described by $\beta = 2$ is measured which in turn corresponds to Equation 2.70.

Photoionization not only happens in atoms but also in molecules. In case of ionizing an electron bound to a molecule the nuclear motion has to be taken into account. As shown in Section 2.1.3, the potential energy of a molecule depends on the nuclear constellation $\vec{R}$, and in the simple case of a diatomic molecule, on the internuclear distance R. Based on the Born-Oppenheimer approximation photoionization is considered as instantaneous compared to the time scale of nuclear motion. This means that the positions of the nuclei do not change until the photoionization has occurred. In a diagram showing the potential energy as a function of the internuclear distance the transition is drawn in form of a vertical line as it is illustrated in Figure 2.5. This

---

[13] $\Delta m_l = 0$ does only hold for linearly polarized light. For photoionization with circularly polarized light it is $\Delta m = \pm 1$.

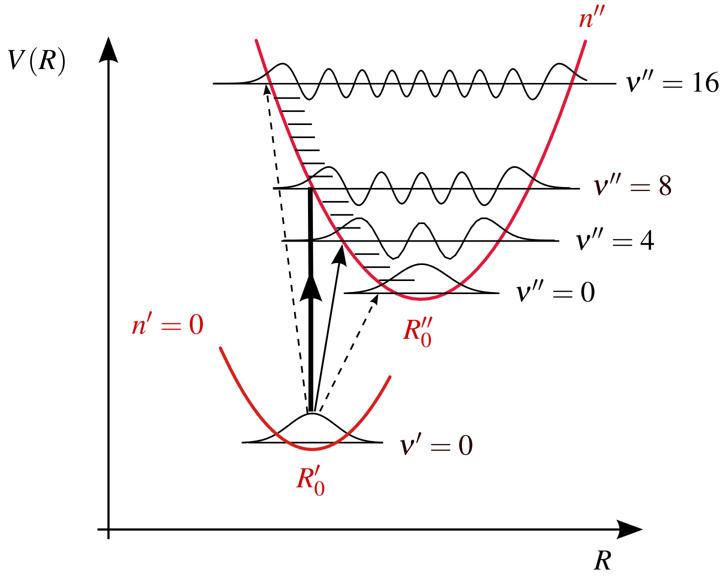

Figure 2.5: The Franck-Condon principle states that photoionization occurs instantaneously compared to the nuclear motion so that the molecule makes a vertical transition. The transition probability increases the more overlap the vibrational wave functions of initial and final states have. In this example the vibrational state $v'' = 8$ has the highest relative occupancy probability (modified from [18]).

simple relation is called Franck-Condon principle and the range of the nuclear distance, where these transitions occur, the Franck-Condon area. Referring to Equation 2.70 and considering the total wave function[14] of a diatomic molecule $\Psi_{n,v}(r,R) = \Phi_n^{\mathrm{el}}(r) \cdot \chi_n^v(R)$ the partial cross section in the dipole approximation reads

$$\frac{d\sigma}{d\Omega} \propto |\langle \Phi_f^{el}(\vec{r}) \cdot \chi_f^{v'}(\vec{R})|z|\Phi_i^{\mathrm{el}}(\vec{r}) \cdot \chi_i^{v}(R)\rangle|^2 = \underbrace{|\langle \chi_f^{v'}(R)|\chi_i^{v}(R)\rangle|^2}_{P_{FC}} \cdot \underbrace{|\langle \Phi_f^{\mathrm{el}}|z|\Phi_i^{\mathrm{el}}\rangle|^2}_{d_{fi}^2} \,, \qquad (2.72)$$

where $\int \chi_f^{v'}(R)\chi_i^{v}(R)dR$ is the overlap between the final and initial vibrational wave function. Its square

$$P_{\mathrm{FC}} = \int \chi_f^{v'}(R)\chi_i^{v}(R)dR \qquad (2.73)$$

is called Franck-Condon factor. If the final molecular state consist of more than one vibrational modes, the Franck-Condon factors denote the relative occupancy probabilities.

Beside inducing additional vibrational transitions, molecular photoionization can also lead to dissociation of the molecule. Hence, there is the possibility that the ions show a shaped angular distribution depending on the polarization of the light as well. Experiments with CF_3I or OCS have shown, that for linearly polarized light the differential cross section can be described by the same Equation 2.71 as for photoelectrons including the anisotropy paramenter β [19, 20]. A strong alignment of the molecule during the ionization process or different symmetries of the initial and the final state are found to be the reasons of the anisotropy. Since the molecular wave function is determined by quantum numbers (see Table 2.3), there are selection rules for electronic transitions analogous to those of atomic transitions. Depending on the polarization, the projection of the angular momentum changes $\Delta\Lambda = \Delta|M_L| = 0, \pm 1$, whereas the total S spin remains unchanged. If the molecule is diatomic, its symmetry does not change with respect to the molecular axis. If it is in addition homonuclear, the parity switches ($g \rightarrow u$ or $u \rightarrow g$).

---

[14] The spin part χ_s does not contribute here and can be neglected.

2.2.2 Double ionization

Double ionization describes the process of light interacting with a quantum mechanical system resulting in the emission two electrons. There are two types of double ionization that need to be distinguished. The process, where the light field interacts with both electrons that are ejected, is called sequential or two-step-two (TS2) double ionization. Since atoms and molecules can interact with only one photon at a time, this model requires at least two photons. Each electron then absorbs one photon or more independently of the other electron until it has sufficient energy $E = n \cdot h\nu > E_{\text{bind}}$ to escape from the bound state. Sequential double ionization occurs preferably in intense light fields, such as intense laser pulses, due to high photon density but low photon energy. However, if the energy of a single photon exceeds a certain energy threshold, it can induce non-sequential double ionization, which means that both electrons are ejected in the same process. Three different mechanisms of non-sequential double ionization are briefly discussed in the following sections.

Shake off

After one electron has been removed from the system by absorbing one photon, the total wave function remains altered. The basis set of orthonormal states of the system has changed. The wave functions of the electrons must be projected on the new eigenstates [21]. Since some of the states are in the continuum, there exist a probability, that an electron jumps to one of these unbound states. Semiclassically the process is understood as a sudden change of the effective potential acting on the valence electrons sitting in the outermost shell after the energy levels have shifted downwards due to the missing electron. Figure 2.6 shows how one valance electron is "shaken off" due to the shift of the energy levels, i.e. the shrinking electron cloud.

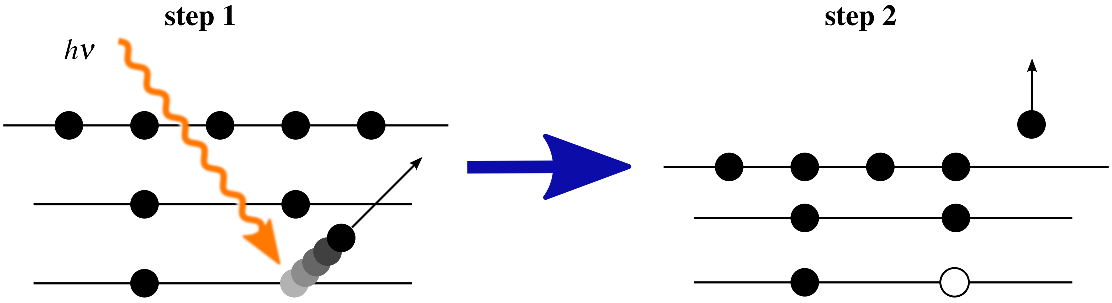

Figure 2.6: In the shake-off process the valence electron remains in a continuum state after the effective potential has suddenly changed due to a precedent photoionization.

Two-step-one

In the two-step-one (TS1) process shown in Figure 2.7 the photon interacts only with one electron transferring its energy so that it can escape from its bound state with the kinetic energy $E'_{\text{kin},1} = h\nu - E_{\text{bind},1}$. There is a probability of the electron interacting with a second electron while leaving the molecule thereby transferring sufficient energy to lift it into the continuum.

The second electron then has the kinetic energy

$$E_{\mathrm{kin},2} = h\nu - E_{\mathrm{bind},1} - E_{\mathrm{bind},2} \; , \tag{2.74}$$

whereas the first electron remains with

$$E_{\mathrm{kin},1} = E'_{\mathrm{kin},1} - E_{\mathrm{kin},2} \; . \tag{2.75}$$

Due to the collision between both electrons the total available energy is continuously distributed among them. However, the sum of the kinetic energies of both electrons

$$E_{\mathrm{kin},1} + E_{\mathrm{kin},2} = h\nu - E_{\mathrm{bind},1} - E_{\mathrm{bind},2} = \mathrm{const} \tag{2.76}$$

is constant. It is important to note that the sum of the binding energy of the fist and second electron $E_{\mathrm{bin},1} + E_{\mathrm{bind},2}$ is given by the double ionization potential of the system. If the second electron is ejected from the partner molecule, the system remains in a dissociative state. In this case the nuclear geometry at the point of the electronic transition has to be taken into account. As it is illustrated in Figure 2.8, the double ionization potential then includes the dissociation energy D_0, the single ionization potentials of the involved molecules and the kinetic energy release (KER), which is the kinetic energy that the fragmenting nuclei gain during the Coulomb repulsion. The constant sum of the kinetic energies of the electrons can be shifted according to the width of the KER of the ions.

The TS1 process has been experimentally confirmed in simple atoms such as helium [22] and in complex molecules like acetylene C_2H_4 [23]. Since the first electron can only knock off a second electron, if it travels in the direction of where the scattering partner is located, the TS1 can be distinctly identified in atoms by examining the angle between the electrons [24]. TS1 in molecules is identified by exploring the angular distribution of the electrons depending on the nuclear distance as it was shown for the helium dimer He_2 [25].

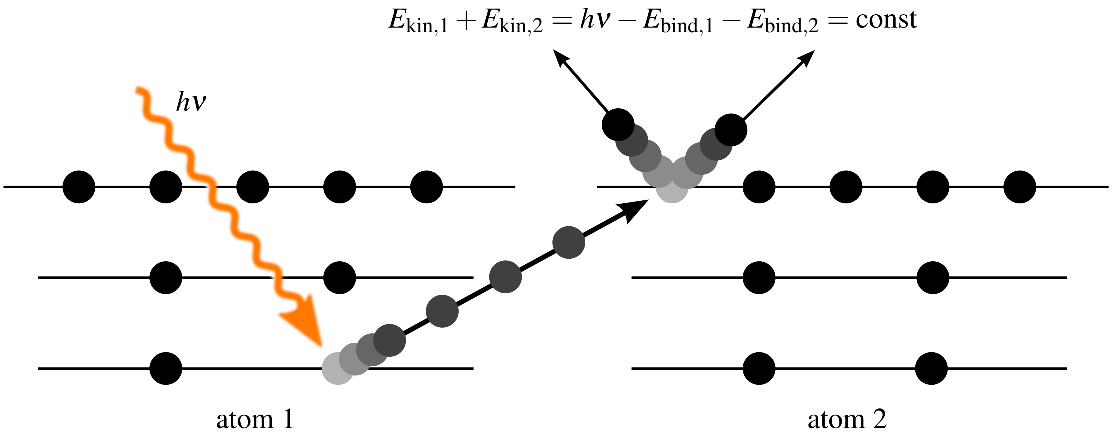

Figure 2.7: In the two-step-one model of double ionization one electron first absorbs the photon. On its way out of the molecule it scatters with a second electron lifting it into the continuum (kick off). The sum of the kinetic energy of both electrons is constant, however it is distributed continuously among the electrons.

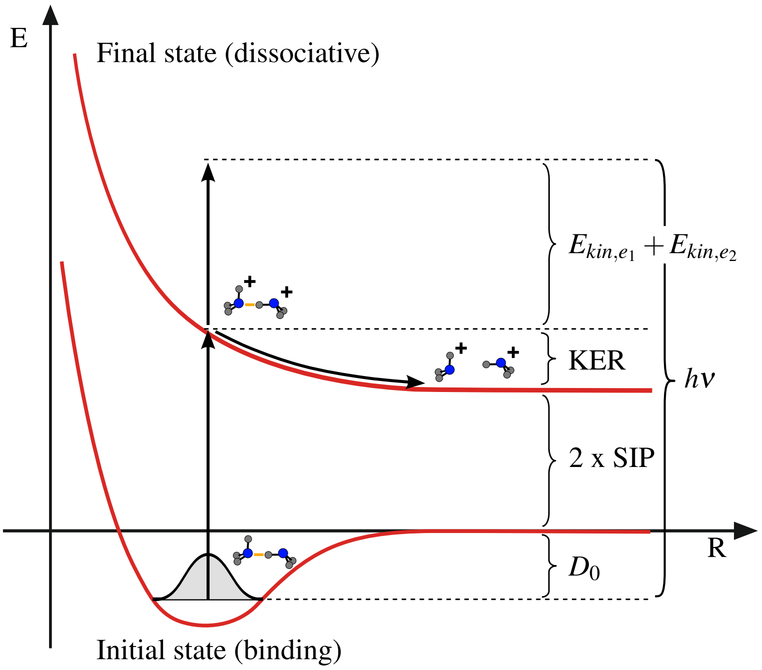

Figure 2.8: Double ionization of the system by knock-off can lead to a direct transition from the bound state to a dissociative state. In this case the exact amount of energy, that is shared by the electrons, depends on the KER, which is determined by the nuclear structure at the point of the electronic transition.

Auger decay in the two-step-one model

Photoionization of a molecule[15] by ejecting a core electron leaves the molecule in an excited state with an inner-shell vacancy. This vacancy can subsequently be filled by an electron from one of the higher energy levels. Thereby surplus energy is released either by emitting a photon or a weakly bound electron from one of the valence orbitals. The latter mechanism, shown in Figure 2.9, is called Auger effect, a double ionization process named after one of its discoverers, Pierre Victor Auger [26].

Emitting a photon (fluorescence) and ejecting a second electron are competing processes, however the probability of fluorescence increases with higher proton number. The kinetic energy of the auger electron is determined by its binding energy E_{bind} and the difference of the potential energies ΔE_{mf} between the final state $|\Psi_f\rangle$ and the intermediate state $|\Psi_m\rangle$:

$$E_{\text{kin,Aug}} = \Delta E_{mf} - E_{\text{bind,Aug}} \ . \tag{2.77}$$

The Auger decay channels are classified by the principal quantum numbers (notation for electron shells) of the vacancy, the electron that fills the vacancy and the auger electron. For example filling a K-shell vacancy with an L-shell electron accompanied by the emission of an Auger electron from the L-shell is then labeled as a KLL-transition. The Auger decay in the two-step-one model is divided into two steps. First the molecule is lifted from its initial state $|\Psi_i\rangle$ into an excited state $|\Psi_m\rangle$ which is considered as the intermediate state by photoionization. In the following step the system decays into its final state $|\Psi_f\rangle$ by electronic transition and ejection of

---

[15] The following considerations also hold for atoms.

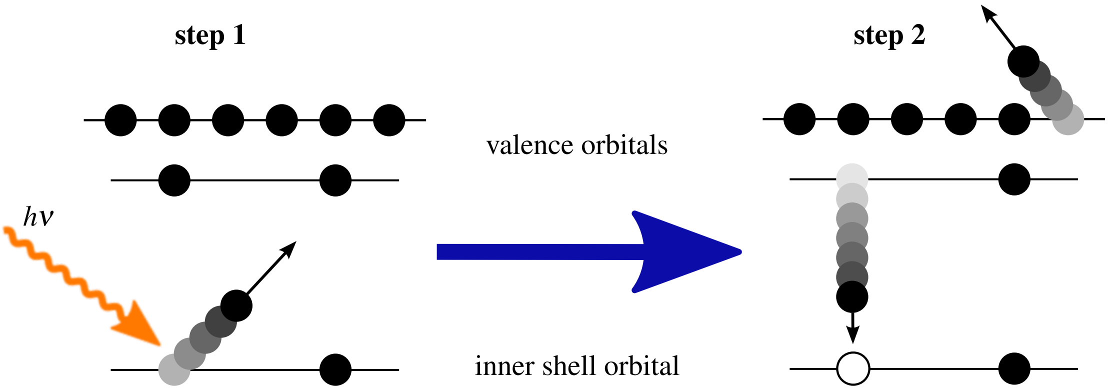

Figure 2.9: The auger decay can be divided in two steps. In step 1 the system is photoionized by a photon ejecting a core electron. In step 2 the vacancy is occupied by an electron from a higher energy level. Thereby, the energy difference of both levels is released and transfered to a weakly bound valence electron which is lifted into the continuum. The kinetic energy of the Auger electron is given by $E_{\text{kin,Aug}} = E_f - E_m - E_{\text{bind,Aug}}$, with E_f denoting the energy of the final state, E_m the energy of the intermediate state and E_{bind} the binding energy of the Auger electron.

the Auger electron. Its intensity can then be determined by the product

$$I_{\mathrm{A}} = P_{\mathrm{A}} \cdot P_{\mathrm{PI}} \,, \tag{2.78}$$

where $P_{\mathrm{A}} = |\langle \Psi_f | \hat{V} | \Psi_m \rangle|^2$ denotes the transition probability of the Auger effect (step 2) and $P_{\mathrm{PI}} = |\langle \Psi_m | \hat{D} | \Psi_i \rangle|^2$ the probability of the photoionization (step 1) [27]. $\hat{V}$ is the operator of the Coulomb interaction that depends on the distance between the involved electrons. $\hat{D}$ is the dipole operator which is derived in Section 2.2.1. Describing the Auger decay in molecules, the nuclear motion has again to be taken into account. Using Fermi's golden rule the following relation for the intensity of the Auger electron is found [28]:

$$I_{\mathrm{A}} \propto \sum_f \sum_m |\langle \Psi_f | \hat{V} | \Psi_m \rangle|^2 |\langle \Psi_m | \hat{D} | \Psi_i \rangle|^2 \delta(\Delta E_{mf} - E_{\text{bind,Aug}}) \,, \tag{2.79}$$

with the delta function assuring energy conservation. After separating the electronic and the nuclear part $|\Psi\rangle = |\chi\rangle \cdot |\Phi^{\mathrm{el}}\rangle$ the sum over all vibrational modes of intermediate and final states has to be taken:

$$I_{\mathrm{A}} \propto \underbrace{|T_{\mathrm{A}}|^2 |T_{\mathrm{PI}}|^2}_{\substack{\text{electronic}\\\text{transition}}} \sum_f \sum_m \underbrace{|\langle \chi_f | \chi_m \rangle|^2 |\langle \chi_m | \chi_i \rangle|^2}_{\text{FC}-\text{factors}} \delta(\Delta E_{mf} - E_{\text{bind,Aug}}) \,. \tag{2.80}$$

If, in case of diatomic molecules, the final state is dissociative so that the molecule breaks apart, the sum of the KER and the kinetic energy of the Auger electron is constant. Hence, if these energies are known, different Auger decay channels can be assigned [29].

2.2.3 Intermolecular Coulombic decay

All ionization processes described so far have been known for many decades. In contrast, the intermolecular Coulombic decay[16] (ICD) is a decay process relatively newly described. Cederbaum, Zobeley, and Tarantelli were the first one to theoretically predict the ICD in 1997 as a novel decay mechanism that is supposed to occur in weakly bound atoms or molecules [2]. A few years later the experimental evidences for ICD were found, first in simple molecules such as the neon dimer $(\mathrm{Ne})_2$ [3] and later on also in complex system such as water clusters $\mathrm{H_2O}\cdots\mathrm{H_2O}$ [30].

Similar to the Auger decay, ICD starts with an inner-valence shell photoionization leaving the molecule or atom in an excited state. If the system de-excites by filling the vacancy with an electron from a higher energy level, the released energy is used to eject a second electron from one of the outer-valence orbitals (single-site Auger decay) or emit a photon (fluorescence). However, in some systems the de-excitation energy is smaller than the binding energy of the weakest bound electron[17] which means that the single-site Auger decay is energetically forbidden. In this case Cederbaum, Zobeley, and Tarantelli suggest, that the de-excitation energy can be transfered to a weakly bound atomic or molecular neighbor which itself subsequently undergoes an ionization [2]. The decay rate of ICD is proportional to $|V_{ov_1,ov_2,iv_1,c} - V_{ov_1,ov_2,c,iv_1}|^2$, where the two Coulomb matrix elements [31]

$$V_{ov_1,ov_2,c,iv_1} = \int\int \Phi^*_{ov_1}(\vec{r}_1)\Phi_c(\vec{r}_1)\frac{e^2}{|\vec{r}_1-\vec{r}_2|}\Phi^*_{ov_2}(\vec{r}_2)\Phi_{iv_1}(\vec{r}_2)d\vec{r}_1 d\vec{r}_2 \tag{2.81}$$

and

$$V_{ov_1,ov_2,iv_1,c} = \int\int \Phi^*_{ov_1}(\vec{r}_1)\Phi_{iv_1}(\vec{r}_1)\frac{e^2}{|\vec{r}_1-\vec{r}_2|}\Phi^*_{ov_2}(\vec{r}_2)\Phi_c(\vec{r}_2)d\vec{r}_1 d\vec{r}_2 \tag{2.82}$$

are called exchange and direct contribution, respectively. The index 1 marks the first molecule or atom, whereas the index 2 marks its neighbor. The indices *ov* and *iv* denote the outer-valence and inner-valence shell, respectively, that are involved in the process. *c* labels the continuum state. Both integrals describe different sub-processes of ICD, yet they are indistinguishable based on the result, as illustrated in Figure 2.10. The exchange integral describes the process of an electron transfer: the vacancy in the inner-valence shell of atom 1 is occupied by an electron from an outer-valence shell of atom 2, thereby releasing de-excitation energy which is used for ejection of a outer-valence electron in atom 1.

The direct integral describes the transfer of energy by exchanging a virtual photon. A valence electron of atom 1 drops into the previously created core hole thereby transferring the released de-excitation energy to its atomic neighbor which subsequently emits one of its outer-valence electrons.

Both sub-processes are followed by a Coulomb explosion of the ions. These two competing processes can be distinguished based on the parity of the excited intermediate state as shown by Jahnke et al. [32]. Furthermore the relative contribution of the different processes can be determined. For example Scheit, Cederbaum, and Meyer showed that, in case of a 2s-ionization of the neon dimer, the direct term mainly contributes to the occurring ICD due to the large distance between both neon atoms [33]. In general the probability of ICD, i.e. its decay rate, is determined by the electronic overlap of the involved orbitals, calculated in the Coulomb matrix

---

[16] If the decay occurs in bound molecules or atoms the term intermolecular or interatomic, respectively, is used. In the following ICD shall be considered in molecules unless differently declared.

[17] This may arise from the fact that after photoionization the effective potential for the remaining electrons increase so that they are bound stronger, i.e. their energy levels are shifted downwards.

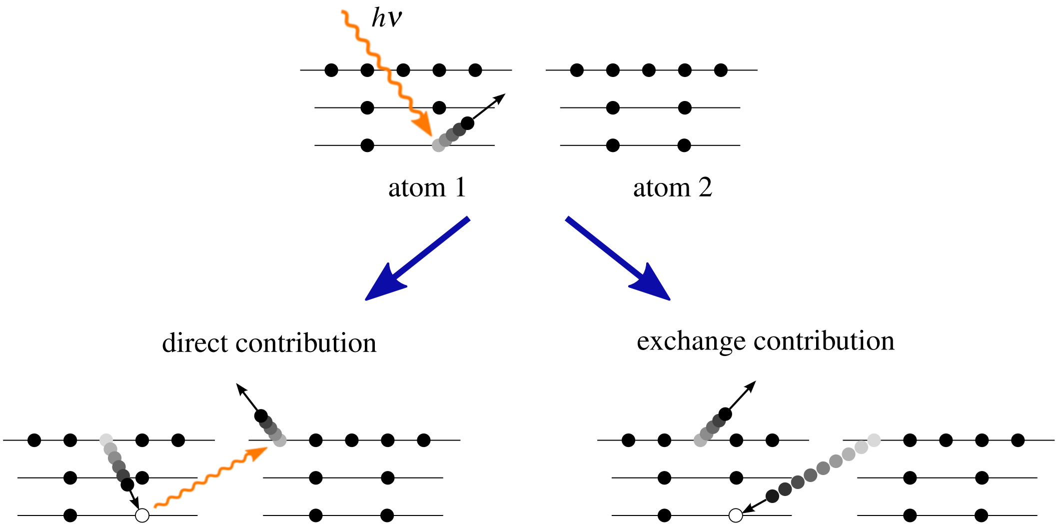

Figure 2.10: Intermolecular or interatomic Coulombic decay can occur in weakly bound molecules or atoms if a single-site Auger decay is energetically forbidden. The de-excitation energy released by filling the previously created inner-valence vacancy by an outer-valence electron is used to emit a second outer-valence electron. **Left:** In the direct contribution the core hole in atom 1 is occupied by one of its outer-valence electrons. The energy is transfered to the partner atom in form of a virtual photon ejecting the second electron. **Right:** In the exchange contribution the core hole of atom 1 is occupied by an outer-valence electron of atom 2, thereby releasing de-excitation energy which is used for the ejection of an outer-valence electron in atom 1.

elements as described in Equations 2.81 and 2.82, as well as the number of different decay channels. Hence using Fermi's golden rule the general decay rate is given by [34]

$$2\pi\sum_{c}\sum_{ov_1}\sum_{ov_2>ov_1}|V_{ov_1,ov_2,iv,c}-V_{ov_1,ov_2,c,iv}|^2\delta(\Delta E)\,, \tag{2.83}$$

with the δ-function requiring energy conservation of the process and thus specifying the available decay channels:

$$\Delta E=\varepsilon_{iv}-\varepsilon_{ov_1}-\varepsilon_{ov_2}+V_{ov_1,ov_2,[ov_1,ov_2]}+\varepsilon_c-V_{c,ov_1,[c,ov_1]}-V_{k,ov_2,[k,ov_2]}\,. \tag{2.84}$$

The equation above includes the following components:

- the ionization potential of the inner-valence electron:

  $$\varepsilon_{vi}$$

- the energy sum of final states of both the molecules or the atoms with a hole in the outer-valence shell containing the ionization potentials and their interaction among each other:

  $$-\varepsilon_{ov_1}-\varepsilon_{ov_2}+V_{ov_1,ov_2,[ov_1,ov_2]}$$

- the kinetic energy of the ICD electron and its residual interaction with the two holes in the outer-valence shells:

  $$\varepsilon_c-V_{c,ov_1,[c,ov_1]}-V_{k,ov_2,[k,ov_2]}$$

The simplified energy balance of the ICD process is illustrated in Figure 2.11. As seen in the figure, the kinetic energy of the photoelectron is given by the difference of photon energy and

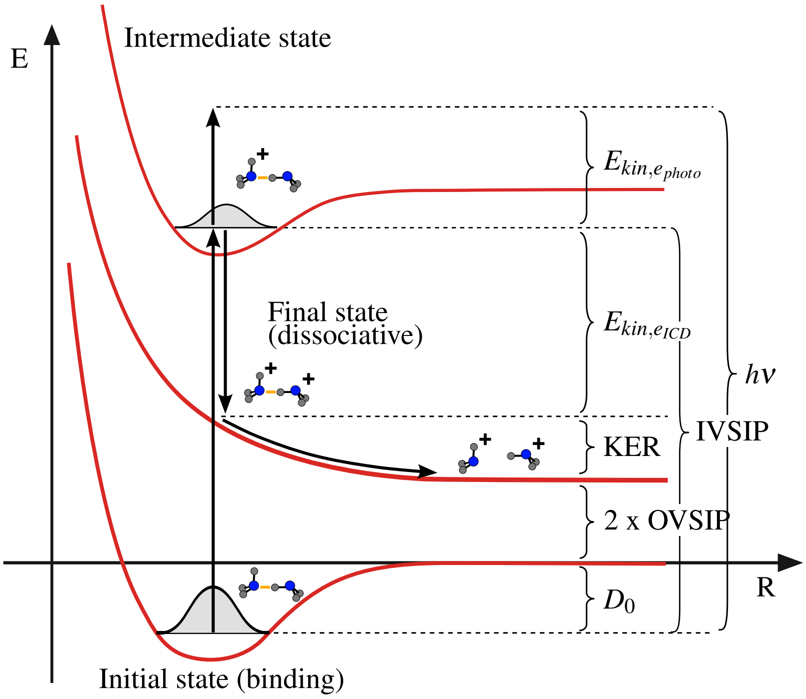

Figure 2.11: In the process of ICD the system first makes a transition from the bound state to an excited state due to photoionization. Thereafter, the system decays by falling onto the dissociative state by emitting the ICD electron.

the inner-valence single ionization potential (IVSIP):

$$E_{\mathrm{kin,photo}} = h\nu - \mathrm{IVSIP}\ . \tag{2.85}$$

After the emission of the photoelectron the deposited energy is partly freed up by de-excitation. As can be seen in Figure 2.11, this constant amount of energy is shared by the ions in form of the KER and by the ICD electron

$$E_{\mathrm{kin,ICD}} + \mathrm{KER} = h\nu - D_0 - 2 \times \mathrm{OVSIP}\ . \tag{2.86}$$

The outer-valence single ionization potentials OVSIP are defined as the energy that is required to singly ionize each of the molecules in the continuum. Furthermore, Figure 2.11 illustrates that a system is able to undergo ICD, only if at least one inner-valence ionization potential lies above the lowest two-site double ionization potential. Moreover the probability of ICD as a potential decay mechanism increases the more DIP lie below a IVSIP, i.e. the more decay channels are available. Hence, ICD can be a very efficient de-excitation process, especially in complex molecules and clusters.

2.3 ICD in hydrogen bonded systems

The hydrogen bonded systems used for the experiment are the ammonia dimer $NH_3 \cdots NH_3$ and the ammonia water molecule $NH_3 \cdots H_2O$. In the following sections the monomers NH_3 and H_2O are introduced with respect to their electronic and geometric characteristics. Furthermore, it is explained how they form hydrogen bonds. Finally, the process of ICD in these systems is presented in detail.

2.3.1 ICD in the ammonia dimer $NH_3 \cdots NH_3$

The ammonia monomer consists of three hydrogen atoms and one nitrogen atom. The electron configuration of nitrogen is

$$(1s)^2(2s)^2(2p_x)(2p_y)(2p_z)\ ,$$

where the three electrons in the p-orbitals form directed bonds to the $1s$-orbitals of the hydrogen atoms. As illustrated in Figure 2.12 all three binding p-orbitals form an angle of 106.7° with respect to each other.[18] This is due to hybridization[19] of the orbitals. The relaxed geometry of the molecule resembles an slightly skewed tetrahedron. Similar to the water molecule, NH_3 forms a permanent electric dipole $\vec{D}$ due to its asymmetric charge distribution. The dipole moment with a magnitude of $|\vec{D}| = 1.78$ D is directed along the symmetry axis (C3-axis) pointing from the nitrogen atom to the middle of the triangle spanned by the three hydrogen atoms [35]. The vibrational modes of the ammonia molecule arise from the possibility of the N atom to swing up and down along the C3-axis. The potential energy of the molecule depends on the height of the N atom above the plane spanned by the H atoms. It reaches its minimum for $h = 0$ and its maximum for $h = \pm h_0$, respectively. The ground state of NH_3 is a superposition of the nitrogen

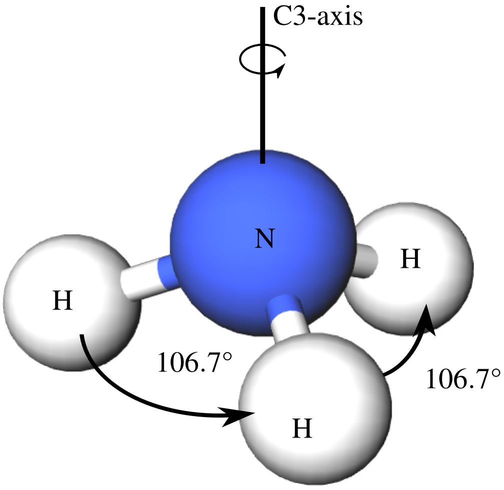

Figure 2.12: The three electrons of hybridized p-orbitals of the nitrogen atom bind to the $1s$-orbitals of each hydrogen atom thereby giving the ammonia molecule the structure of a slightly skewed tetrahedron. The molecule can rotate about the C3-axis.

---

[18] The theoretically optimal geometry varies depending on the used calculation method. For instance, when using second order Møller-Plesset method ,106.8° is obtained [10].

[19] The phenomenon of deformation of atomic orbitals due to electron-electron interaction is called hybridization. By deforming their orbitals the binding atoms reach a lower energy level.

atom being located above and below the plane. Although classically forbidden, the nitrogen atom is able to change position by tunneling through the potential barrier.

If two ammonia molecules get close to each other, they can form a dimer $NH_3 \cdots NH_3$ through a hydrogen bond. Even though similar molecules such as the water dimer $H_2O \cdots H_2O$ are both theoretically and experimentally well understood, there is still discrepancy between experimental and computational results regarding the geometrical structure of the $NH_3 \cdots NH_3$. The first *ab initio* calculations proposed a geometry as shown in Figure 2.13 where the binding hydrogen atom is located on the axis connecting the H-donor and the H-acceptor [36, 37]. In literature this geometry often is referred to as the classical hydrogen bonded structure with the following notation:

$$\underbrace{NH_3}_{\text{H-donor}} \cdots \underbrace{NH_3}_{\text{H-acceptor}} \quad .$$

However spectroscopic measurements of the quadrupole hyperfine structure led to contradicting results suggesting an asymmetric cyclic structure [38, 39]. Compared to out-dated Hartree-Fock calculations, modern *ab initio* methods such as DFT calculations [40] or MP2 perturbation theory [35] obtained more reliable results using larger basis sets and taking all particles into account including electron correlation. Contrary to the experimental results of Nelson Jr, Fraser, and Klemperer [39] the minimal energy of the system was again found under the assumption of the classical hydrogen bond structure as optimal geometry. Far-infrared spectroscopy shows the importance of dynamic effects in the dimer thereby implying that vibrational averaging might be the reason for this discrepancy [41, 42]. The equilibrium distance R_0 between both N atoms is determined within a range of 3.2 Å to 3.4 Å [39, 43, 44]. The exact value again depends on the calculation method.

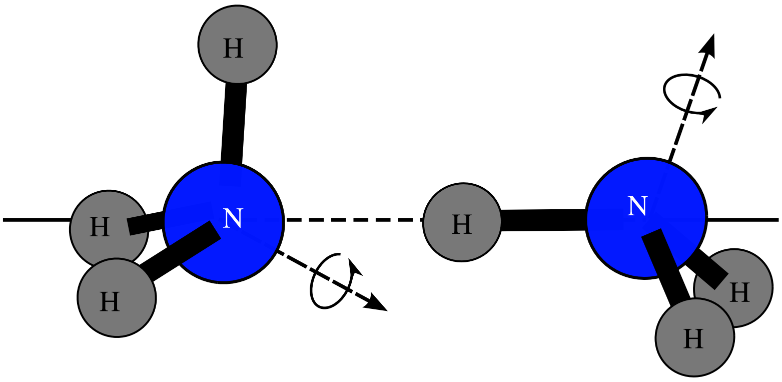

Figure 2.13: Schematic of the ammonia dimer in the classical hydrogen bonded geometry. The $N-H-H$ is arranged nearly linearly so that the bonding H atom almost lies on the C3-axis of the proton-acceptor.

The ammonia dimer is a hydrogen bonded system with a complex electronic structure. Hence, the absorption of a photon can induce various electronic dynamics. Kryzhevoi and Cederbaum suggest, that ICD is a possible decay mechanism, if the energy deposited by the photon is sufficient [9]. After photoionization of an inner-valence orbital an isolated NH_3 molecule cannot de-excite by emitting an Auger electron since it is energetically forbidden. In the dimer, however, the de-excitation energy can be transferred to the partner molecule followed by the emission of an outer-valence electron. Thereupon both, the H-acceptor or H-donor, remain singly ionized and fragment in a Coulomb explosion. The intermolecular decay can take place in two ways:

- **proton-donor decays**

  Step 1 (inner-valence ionization):

$$\mathrm{NH_3\cdots NH_3 \xrightarrow{h\nu} NH_3^{+}}(iv^{-1})\mathrm{\cdots NH_3} + e^-_{\mathrm{photo}}$$

  Step 2 (ICD):

$$\mathrm{NH_3^{+}\cdots NH_3 \longrightarrow NH_3^{+}\cdots NH_3^{+}} + e^-_{\mathrm{ICD}}$$

- **proton-acceptor decays**

  Step 1 (inner-valence ionization):

$$\mathrm{NH_3\cdots NH_3 \xrightarrow{h\nu} NH_3\cdots NH_3^{+}}(iv^{-1}) + e^-_{\mathrm{photo}}$$

  Step 2 (ICD):

$$\mathrm{NH_3\cdots NH_3^{+} \longrightarrow NH_3^{+}\cdots NH_3^{+}} + e^-_{\mathrm{ICD}}\ .$$

Here, iv^{-1} denotes the inner-valence vacancy. Calculations of the inner- and out-valence single ionization potentials as well as the double ionization potentials, which are based on the classical hydrogen bonded structure, reveal that ICD in $NH_3\cdots NH_3$ should be energetically allowed [9]. The results for the ionization potentials with the highest intensities are presented in Figure 2.14.

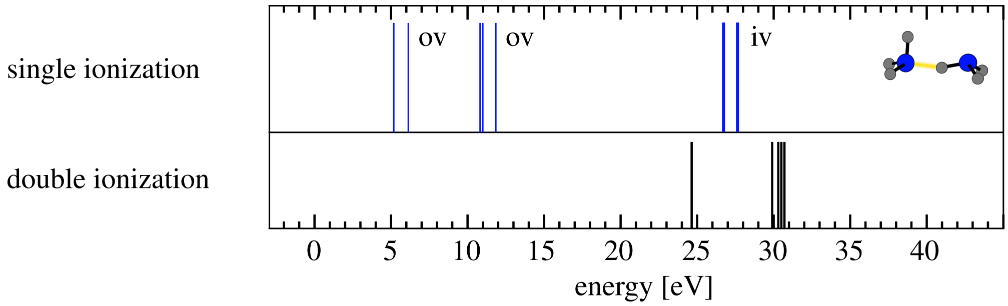

Figure 2.14: Calculated double and single ionization potentials of the ammonia dimer in classical hyrdogen-bonded structure using MP2 perturbation theory [9]. The thin lines in blue in the upper left part correspond to single ionization from an inner-valence orbital whereas the thick lines in blue at higher energies correspond to single ionization from an inner-valence orbital. The lower half of the figure shows the calculated two-site state double ionization potentials.

2.3.2 ICD in the ammonia water molecule $NH_3\cdots H_2O$

The water molecule consists of one oxygen atom and two hydrogen atoms. The electron configuration of oxygen is

$$(1s)^2(2s)^2(2p)^4\ ,$$

where two electrons in the p-orbital form directed bonds to the $1s$-orbitals of the hydrogen atoms. Due to hybridization the p_x- and p_y-orbital form an angle of 105° with each other as illustrated in Figure 2.15. Although the H_2O molecule looks quite simple, its vibrational and rotational spectra are very complex as recent elaborate evaluations showed [45–48]. Its vibrations involve various combinations of symmetric and asymmetric stretching as well as bending. The main rotation axis of the H_2O molecule is the C2-axis lying in the plane spanned

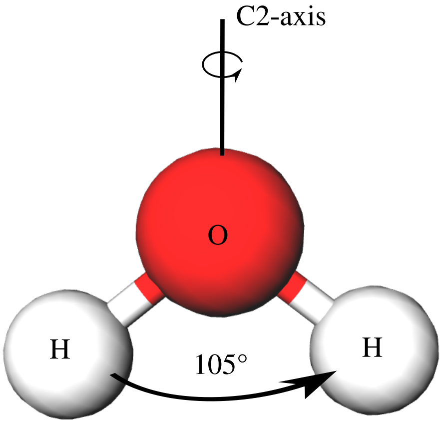

Figure 2.15: Two electrons of the *p*-orbital of the oxygen atom bond to the 1*s*-orbitals of the two hydrogen atoms. Due to hybridization they form an angle of 105°. The water molecule can rotate about the C2-axis.

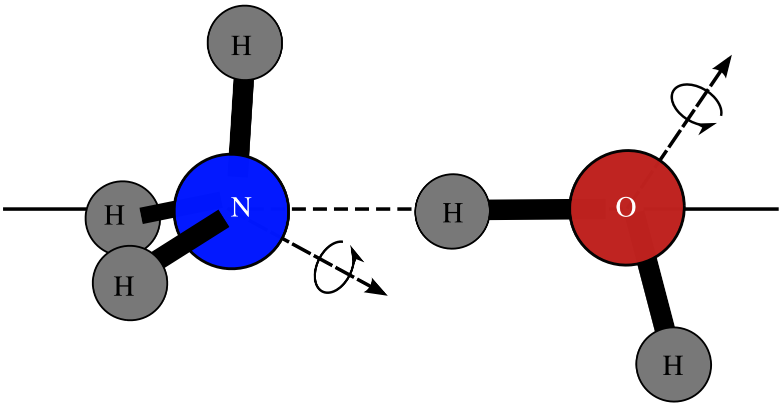

Figure 2.16: Schematic of the ammonia water dimer with water as the proton donor. In the classical hydrogen bonded geometry the $N-H-O$ is arranged linearly, yet the C3-axis forms an angle of 23° with the $O-N$-complex.

by all three H atoms and dividing the angle between the H atoms in half. Due to charge shifting an electric dipole moment $\vec{D}$ is created which points along the C2-axis. With a magnitude of $|\vec{D}| = 2.35\mathrm{D}$ the polarization of water is strong compared to other molecules [18].

A water monomer together with ammonia can form the hydrogen bonded dimer $NH_3\cdots H_2O$. Despite the use of elaborate *ab initio* methods to obtain information about the geometric and energetic structure of weakly bound complexes, the minimum potential geometry of $NH_3\cdots H_2O$ still remains unclear. Although some calculations using perturbation theory lead to contradictory results [49], the majority of studies come to the conclusion, that the classical hydrogen bonded structure, depicted in Figure 2.16, is the optimal geometry [50–53]. By using the method of far-infrared spectroscopy on gaseous $NH_3\cdots H_2O$ this structure was confirmed as the preferred one. The heavy atoms O and N are arranged collinearly with the hydrogen atom between them. The C3-axis of the ammonia molecule forms an angle of 23° with the $N\cdots O$ complex [52]. The distance between the N and the O atom is calculated to 3.27 Å, if N is the proton donor. In the case of O being the proton donor, the distance is calculated to 2.95 Å [10]. Further spectroscopic investigations showed that the dimer allows many types of motions with low energy barriers to occur such as nearly free rotation about the C3-axis or exchange of the water proton [52]. Since

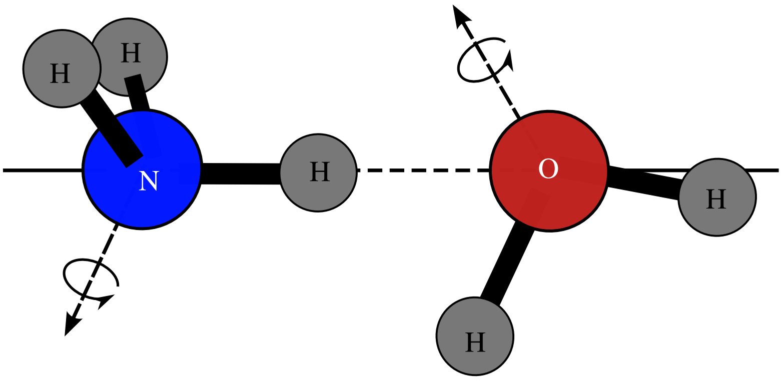

Figure 2.17: Schematic of the ammonia water dimer with water as the proton acceptor. In the classical hydrogen bonded geometry the N – H – O is arranged linearly.

rotational excitation energies ranging in the order of meV congest the energy bands of vibrational excitation ($< 1\,\mathrm{eV}$), electronic transition energies are expected to be smeared out due to rovibrational motion [54].

Similar to the single ionization potentials in ammonia, Stoychev, Kuleff, and Cederbaum found that the potentials in water are also arranged so that an Auger decay after inner-valence ionization is energetically forbidden [10]. However with an adjacent NH_3 the core ionized water molecule can de-excite via ICD. Stoychev, Kuleff, and Cederbaum distinguish two different bonded systems depending on which molecule is donating or accepting the hydrogen proton. In Figure 2.16 water is the proton-donor whereas in Figure 2.17 it acts as the proton-acceptor. Since the inner-valence ionization in step 1 of the ICD process can occur in both molecules of the dimer, there are four reactions that has to be considered:

- $H_2O \cdots NH_3$
  - **proton-donor decays**

    Step 1 (inner-valence ionization):

    $$H_2O \cdots NH_3 \xrightarrow{h\nu} H_2O^+(iv^{-1}) \cdots NH_3 + e^-_{\text{photo}}$$

    Step 2 (ICD):

    $$H_2O^+ \cdots NH_3 \longrightarrow H_2O^+ \cdots NH_3^+ + e^-_{\text{ICD}}$$
  - **proton-acceptor decays**

    Step 1 (inner-valence ionization):

    $$H_2O \cdots NH_3 \xrightarrow{h\nu} H_2O \cdots NH_3^+(iv^{-1}) + e^-_{\text{photo}}$$

    Step 2 (ICD):

    $$H_2O \cdots NH_3^+ \longrightarrow H_2O^+ \cdots NH_3^+ + e^-_{\text{ICD}}$$
- $NH_3 \cdots H_2O$
  - **proton-donor decays**

    Step 1 (inner-valence ionization):

    $$NH_3 \cdots H_2O \xrightarrow{h\nu} NH_3^+(iv^{-1}) \cdots H_2O + e^-_{\text{photo}}$$

Step 2 (ICD):

$$NH_3^+ \cdots H_2O \longrightarrow NH_3^+ \cdots H_2O^+ + e^-_{\text{ICD}}$$

- **proton-acceptor decays**

  Step 1 (inner-valence ionization):

$$NH_3 \cdots H_2O \xrightarrow{h\nu} NH_3 \cdots H_2O^+(iv^{-1}) + e^-_{\text{photo}}$$

  Step 2 (ICD):

$$NH_3 \cdots H_2O^+ \longrightarrow NH_3^+ \cdots H_2O^+ + e^-_{\text{ICD}}$$

Assuming the classical geometry Stoychev, Kuleff, and Cederbaum calculated the inner-valence and outer-valence single ionization potentials as well as the two-site state double ionization potentials with the highest intensity. The results for $H_2O \cdots NH_3$ and $NH_3 \cdots H_2O$ are shown in Figure 2.18 and 2.19, respectively.

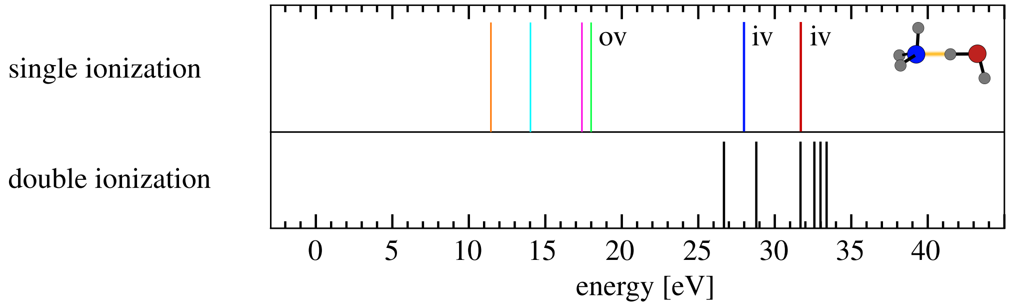

Figure 2.18: Calculated double and single ionization potentials of the ammonia water dimer with water as the proton-donor [10]. The thin lines in the upper left part correspond to the single ionization from an inner-valence orbital. The thick blue line at higher energies corresponds to the single ionization from an inner-valence orbital of the N atom, the thick red line corresponds to the outer-valence singe ionization of the O atom. The lower half of the figure shows the calculated two-site state double ionization potentials.

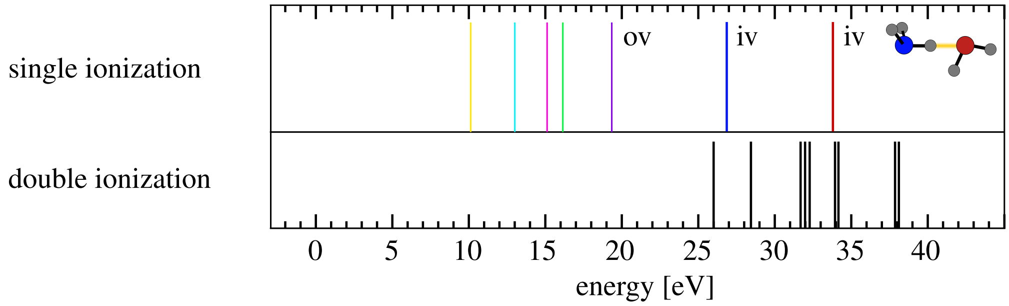

Figure 2.19: Double and single ionization potentials of the ammonia water dimer water as the proton-acceptor [10]. The thin lines in the upper left part correspond to single iv-ionization. The thick blue line at higher energies corresponds to single ov-ionization of the N atom, the thick red line corresponds to ov-ionization of the O atom. The lower half of the figure shows the calculated two-site state double ionization potentials.

Chapter 3

Experimental Setup

For the investigation of the ICD or other ionization processes in molecular systems, in general crossed beam experiments are performed. In these experiments, two beams intersect allowing the projectile and the target to collide thereby creating the reaction. In order to study the decay of $NH_3 \cdots NH_3$ and $NH_3 \cdots H_2O$, a gas jet of water and ammonia was used as a target and synchrotron light for inducing the reactions. In Section 3.1, the syncrotron light source is explained in more detail. The photon energy was chosen at $h\nu = 36\,\mathrm{eV}$ which is sufficient for core-hole ionization of both oxygen and nitrogen. The fragments created subsequent to the reaction were measured using the Cold Target Recoil Ion Momentum Spectroscopy[1](COLTRIMS) method. With this imaging technique the initial momentum vectors of all particles can be reconstruct, thereby getting detailed insight into the precedent reaction on an atomic scale. Figure 3.1 shows the working principle of the performed experiment. The different components of the COLTRIMS setup are discussed in Section 3.2.

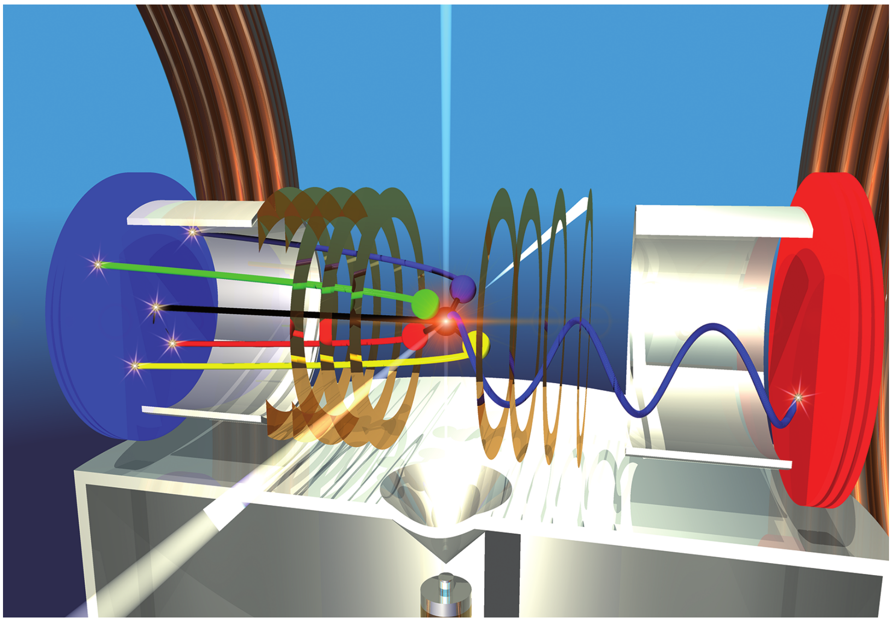

Figure 3.1: Schematic of a reaction microscope. The photon beam intersects with the gas jet inducing a reaction. All fragments can be detected in coincidence. The obtained information about the time-of-flight (ToF) of the particles in the spectrometer and the position of the hits on the detectors allows to reconstruct the initial momentum vector of each fragment (modified from [55]).

---

[1] In standard literature the experimental setup for COLTRIMS measurements is often described as reaction microscope.

3.1 Light source - synchrotron radiation

For investigating the dynamics in quantum mechanical system such as photoionization, different light sources, which are suitable for such experiments, exist. In general, monochromatic light with sufficient intensity is needed. Furthermore most spectroscopic techniques require the reaction volume to be as small as possible. Therefore it is important, that the light beam has a low divergence. In order to compare the quality of light sources, a measure, that includes all required criteria, is defined:

$$\text{brilliance} = \frac{\Phi}{\Delta\Omega^{\Delta\omega}/_{\omega}} , \tag{3.1}$$

with Φ denoting the photon flux, i.e. number of photons per unit area per unit time, $\Delta\Omega$ the solid angle and $^{\Delta\omega}/_{\omega}$ the spectral band width. Since synchrotron light is fulfilling all the requirements mentioned above, it is used for a variety of experiments spanning from lithography to atomic and molecular optical science, and also for the experiment presented in this thesis.

Generally speaking a synchrotron is a cyclic particle accelerator capable of accelerating charged particles to high kinetic energies while bending them onto a closed circular path. In contrast to a cyclotron, the guiding magnetic field of the synchrotron is increased synchronously with the accelerated particles until the particles have reached a velocity near to the speed of light. Although the particles are then kept at constant speed, they are still continuously accelerated by the Lorentz force perpendicular to their direction of travel. According to the principles of electrodynamics, an accelerated charge radiates electromagnetic waves perpendicular to the acceleration vector. Classically the resulting radiation characteristic is dipole-shaped with an angular dependence $I \propto sin^4(\theta)$ as illustrated on the left-hand side of Figure 3.2. However, since the particles in the synchrotron move with nearly the speed of light, the radiation characteristic must be considered relativistically. In the moving framework of the particle the radiation characteristic shows a significantly different angular dependence due to the Lorentz contraction of the coordinates perpendicular to the direction of travel. As seen on the the right-hand side of Figure 3.2, the resulting emission pattern is sharply collimated forward. Hence, the photons are emitted tangentially to the trajectory of the electrons.

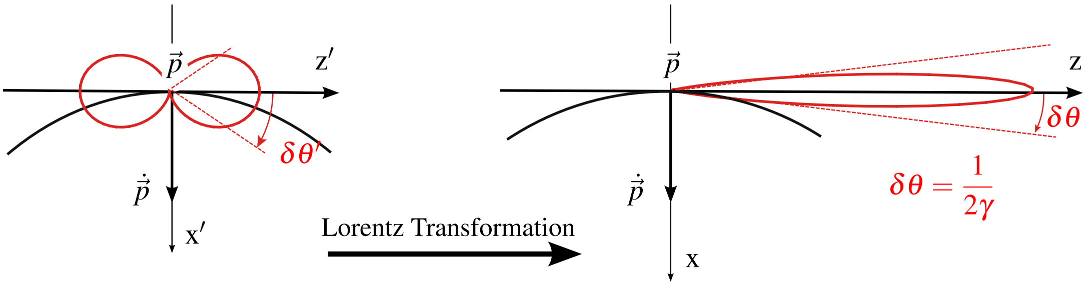

Figure 3.2: Radiation characteristic of electrons that are accelerated perpendicular to the direction of travel. At high velocities the classical dipole characteristic changes to an emission pattern sharply collimated forward due to the Lorentz contraction (modified from [14]).

The width of the beam depends on the velocity of the particles. For small angles the approximation $sin(\theta) \approx \theta$ can be made, so that the divergence angle $\delta\theta$ is defined as the deviation from the tangent. Using this approximation the divergence can be derived to to [14]

$$\delta\theta = \frac{1}{2\gamma} , \tag{3.2}$$

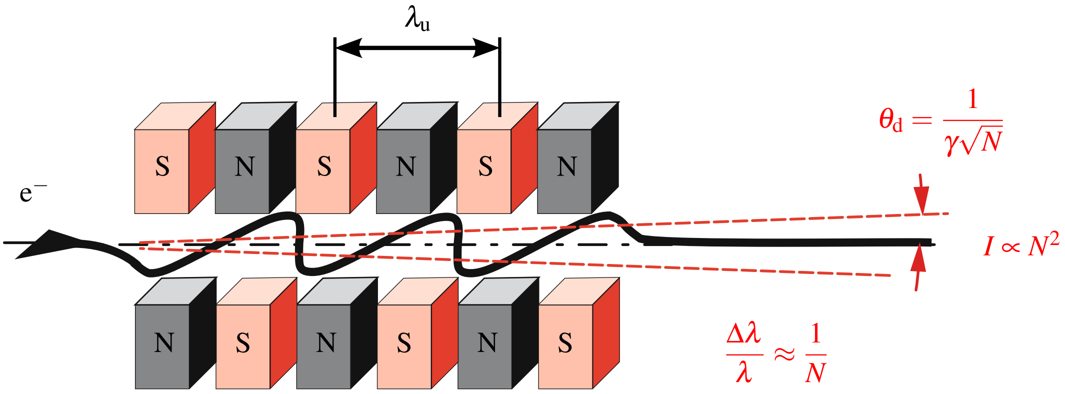

Figure 3.3: In an undulator N bending magnets are arranged in a pattern of alternating north and south poles so that a charged particle is forced on a sinusoidal path radiating N times. The emitted waves constructively interfere leading to an increased intensity of the produced light (modified from [14]).

with $\gamma = \frac{1}{\sqrt{1-\frac{v^2}{c^2}}}$ denoting the Lorentz factor.

Beside the divergence, the radiated power P is also an important measure. Its expression reads (in SI units):

$$P = \frac{q^2 c \gamma^4}{6\pi\varepsilon_0\rho^2}\,, \tag{3.3}$$

where ρ is the radius of the orbital, ε_0 the electric constant, q the charge of the accelerated particle and c the speed of light. Expressing the Lorentz factor γ as the fraction of the relativistic total energy E_{tot} and the rest energy of the particle $E_0 = m_0 c^4$ the relation

$$P \propto \frac{1}{m_0^4} \tag{3.4}$$

is obtained. Hence, in order to maximize the radiated power, the particles should have as low mass as possible.

In third-generations synchrotrons, the radiation intensity is further increased by using insertion devices. Between the bending magnets, that keep the particles on their circular-like path, straight sections are equipped with many magnets arranged in a pattern of alternating north and south poles. These undulators force the electrons on a sinusoidal path as illustrated in Figure 3.3. At each bending point the electrons radiate electromagnetic waves which constructively interfere with each other. Due to this effect the total intensity is proportional to the square of the number of bending magnets N. Beside high intensities, also a better spectral brilliance is attained. The wavelength of the radiation can be changed by varying the strength of the magnetic fields which depends on the vertical distance between the north and south poles. Using various optical elements such as monochrochromators and focusing mirrors the beam quality can be further optimized.

The experiment discussed in this thesis was performed at beamline 10.0.1 at the Advanced Light Source (ALS) in Berkeley, California, USA shown in Figure 3.4. The electron beam of the ALS, which is stored in a ring with 196.8 m circumference, has an energy of 1.9 GeV. The synchrotron is usually run in multi-bunch mode, which means that the electron beam consists of many electron bunches with a time distance of 2 ns. Since it is essential for the experiment, that the photons can be indistinguishably assigned to the reaction they induced, the bunch spacing

Figure 3.4: The Advanced Light Source at Lawrence Berneley National Laboratory with the San Francsico Bay Area in the background [57].

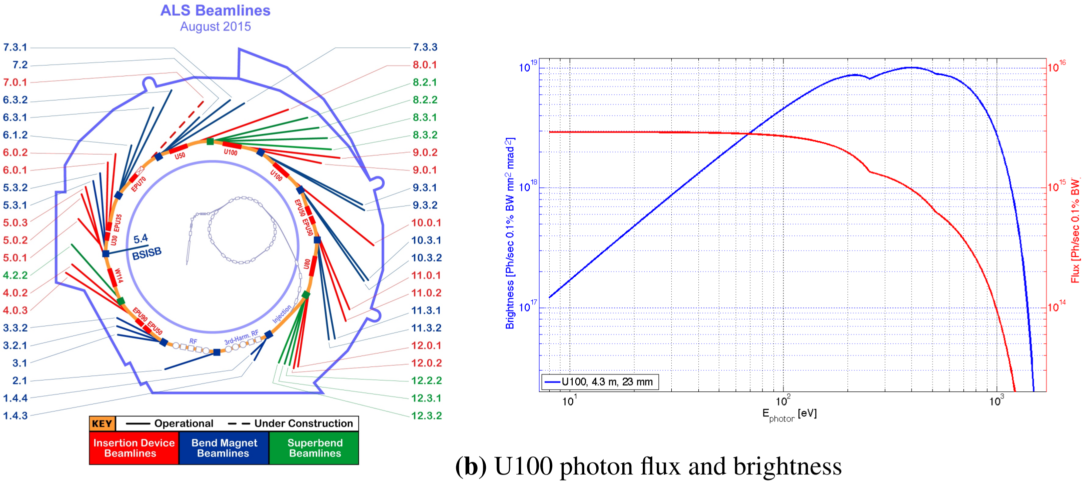

(a) ALS beamclock

(b) U100 photon flux and brightness

Figure 3.5: (a) The ALS beamclock comprises of 44 beamlines which extract the photon beam tangentially to the storage ring. The beamlines are used for experiments of various kinds depending on their energy range [58]. **(b)** Both the brightness and the photon flux of U100 are plotted against the photon energy. At an energy of 36 eV the photon flux is estimated to be $10^{12}\,\mathrm{s}^{-1}$ to $10^{13}\,\mathrm{s}^{-1}$ [56].

has to be larger than the shortest measured ToF, which is in the range of 100 ns. Hence, the experiment was performed during two-bunch mode with a bunch spacing of 328.3 ns. A bunch marker signal is sent from the beamline in sync with the circulating bunches. It is used as the time reference in the data analysis later on. Because the electron bunches continuously scatter with background particles in the storage ring, the beam intensity decreases exponentially. In order to provide a constant beam current of ~35 mA the synchrotron is operated in the top-off mode which means that new electrons are periodically injected. The photon pulses extracted at beamline 10.0.1 are created by the undulator U100 shown in Figure 3.5a which covers an energy range from 12 eV to 1500 eV [56]. Its photon flux in two-bunch mode is reduced to about $10^{12}\,\mathrm{s}^{-1}$ to $10^{13}\,\mathrm{s}^{-1}$ by setting the monochromator to an energy of 36 eV. The beam position can be adjusted in vertical and horizontal direction with alignment mirrors. To reduce the intensity, apertures injected in the beam path can be used. During the experiment the focus of the beam in the reaction zone was approximately 1 mm wide and 0.2 mm high.

3.2 COLTRIMS

The photons coming from the undulator react with the target molecules from the gas jet. In order to image the dynamics of the subsequent fragmentation, a powerful measurement technique is used. COLTRIMS is an imaging technique covering the full solid angle, which means that particles emitted in all spatial direction are coincidently detected.

In order to perform ionization experiments, the complete reaction has to take place in an ultra high vacuum preventing the fragments to interact with background particles. If a fragment scatters with a background particle before it is detected, the information obtained from the measurement cannot be indistinguishably assigned to the initial state of the particle. The vacuum system with all its components is briefly explained in Section 3.2.1. Since the goal of the experiment is to measure the momentum of the particles at the instant of the fragmentation with sufficient precision, the motion of the target molecules prior to the reaction needs to be reduced as much as possible. Therefore, the molecules are prepared in form of a supersonic gas jet (Section 3.2.2) where almost all thermal energy is converted into translation energy. This jet intersects with the pulsed photon beam creating the desired reactions. The created ions and electrons are then accelerated in the electric field of the spectrometer (Section 3.2.3) towards the corresponding detectors.

The light electrons have much higher initial velocities than the ions. Hence, a regular acceleration field of a few $\mathrm{V\,cm^{-1}}$ is not sufficient for collecting them with the full solid angle 4π. In order to prevent electrons from leaving the spectrometer a parallel magnetic field created by large Helmholtz coils attached to the chamber is added. Then, in addition to the acceleration along the spectrometer axis, the general electromagnetic force

$$\vec{F}_{\mathrm{em}} = e(\vec{E} + (\vec{v} \times \vec{B})) \tag{3.5}$$

accelerates the electrons perpendicular to the spectrometer axis thereby forcing them onto a spiral trajectory. The strength of the magnetic field is chosen so that the gyration radius of the spiral motion fits into the spectrometer, i.e. is smaller than the radius of the detectors. Due to their low velocity, the ions are barely affected by the magnetic field and their minimal gyration can be neglected in the momentum calculation.

The detectors are located at both ends of the spectrometer. Equipped with micro channel plates and delay line anodes, they are time and position sensitive (Section 3.2.4). Together with the ToF, which is calculated using the bunchmarker signal as a reference signal, the initial momenta of all particles can be reconstructed.

3.2.1 Vacuum system

As seen in Figure 3.6, the vacuum system of the experimental setup consists of four different regions: the source stage, the second stage, the main chamber and the jet dump. The source stage contains the nozzle which injects the gas jet. Due to its high gas ballast the source stage is pumped by a turbo pump with a pumping speed of ~$1600\,\mathrm{l/s}$. A bypass connects the source stage to the second stage. It is used for pumping and venting both stages at the same time in order to protect the skimmer (0.3 mm diameter) which is the only connection between the two regions beside the bypass. When the bypass is closed the gas expands through the nozzle into the second stage due to the pressure gradient. The second stage is pumped by a turbo pump (~$220\,\mathrm{l/s}$) and connected to the main chamber through a small pinhole (0.5 mm diameter). Due

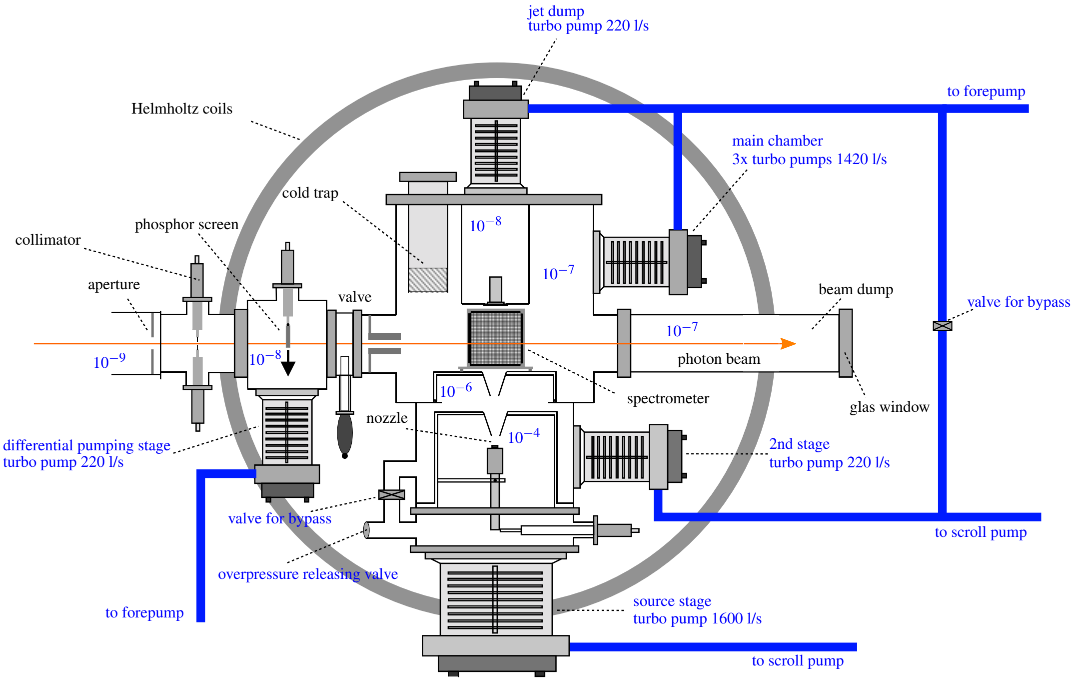

Figure 3.6: The vacuum system of a COLTRIMS setup is divided into four regions: the source stage, second stage, main chamber and jet dump (labeled in blue). A differential pumping stage is mounted to bridge the ultra high vacuum of the beamline to the vacuum in the main chamber. In order to support the turbo pumps different scroll and diaphragm pumps are used which provide the necessary backing pressure (modified from [59]).

to practical reasons of pumping and venting, an additional bypass connects the second stage to the main chamber as well as to the backing pumps which deliver the fore pressure.

The biggest part of the system consists of the main chamber. In order to reach low pressures in the order of 10^{-8} mbar during the experiment, the large volume of the chamber is pumped by three turbo pumps with a total pumping speed of ~1420 l/s. Since most of the molecules in the jet do not interact with the photons or background particles, they pass through the main chamber and have to be collected and removed from the vacuum system. Therefore, a long metal cylinder equipped with a turbo pump (~220 l/s) is attached to the main chamber. If the gas jet is aligned, the molecules are allowed to enter the jet dump through a small pinhole (0.5 mm diameter) which inhibits a back flow into the main chamber. The complete system has to be connected to the beamline which, however, contains a ultra high vacuum of the order of 10^{-10} mbar. Hence, between the main chamber and the beamline a differential pumping stage is mounted bridging the two different pressures. The stage is connected to the beamline by a small aperture and to the main chamber by a narrow cylinder of ~10 cm length. Its vacuum is pumped by a turbo pump (~220 l/s) supported by scroll and diaphragm pumps.

Before starting the measurement a jet test is performed to ensure that the jet passes through all pinholes. The goal of the jet test is to find the maximum pressure in the jet dump depending of the driving pressure, i.e. the gas pressure before the nozzle. The jet test prior to the measurement was performed with nitrogen N_2 at room temperature. Figure 3.7a shows the pressures in all different regions depending on the driving pressure of the nitrogen. One can see that the pressure in the beam dump immediately increases with the driving pressure, whereas the pressure in the main chamber remains constant indicating that the jet passes all pinholes properly. In Figure 3.7b the pressures are shown without the background, i.e. without the gas jet. Based on

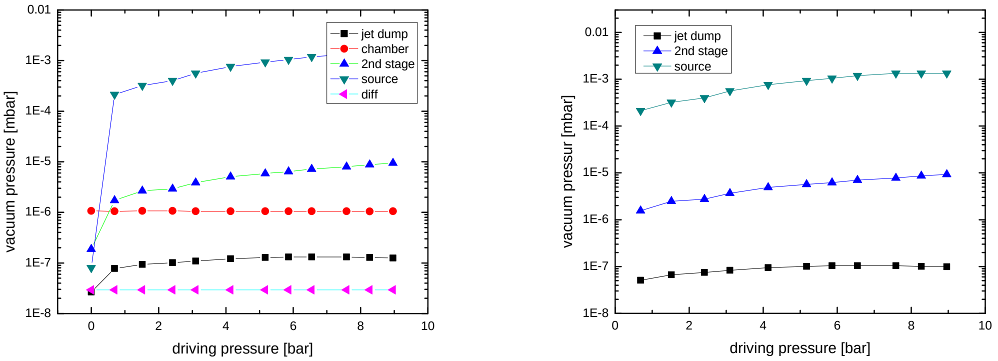

(a) Experimental pressures during the jet test. **(b)** Pressures with background subtracted.

Figure 3.7: **(a)** Prior to the experiment, a jet test with nitrogen N_2 is performed at room temperature. The increasing pressure in the jet dump indicates the jet passing through all pinholes. **(b)** With the background subtracted the pressure in the jet dump slightly shows a maximum at 8 bar, however the driving pressure has to be optimized while using the real target due to other factors affecting the gas jet.

Table 3.1: Experimental pressures in the different parts of the vacuum system with and without a gas jet.

Driving pressure	0 bar	8 bar
Source stage	1×10^{-7} mbar	7×10^{-4} mbar
2nd stage	1×10^{-8} mbar	2×10^{-6} mbar
Main chamber	2×10^{-8} mbar	2×10^{-8} mbar
Jet dump	$< 1 \times 10^{-8}$ mbar	5×10^{-8} mbar

these results, the experiment might preferably be performed with a driving pressure of ~8 bar. However, since the jet quality is affect by other factors as well, in particular the formation of molecular clusters in the jet, the optimal driving pressure continuously had to be adjusted during the experiment.

In order to improve the vacuum, a container made out of copper reaching into the main chamber, a so-called cold trap, is filled with liquid nitrogen from outside. The residual gas in the main chamber condensates on the cold surface on the inside of the chamber. Typical pressures of the different regions during the experiment with a filled cold trap are shown in Table 3.1.

3.2.2 Gas jet

In order to successfully investigate the dynamics of electrons and ions during photoinduced decay mechanisms using momentum spectroscopy, it is crucial for the target molecules to have as little motion as possible. The velocity of particles in an ensemble of atoms or molecules with mass m and temperature T is given by the Boltzmann distribution. However, if only one spatial direction is considered, the absolute value of the velocity is described by a Gaussian distribution [60, chapter 7.3.5]. Considering all degrees of freedom including vibration and rotation, the internal energy is given by

$$U = (f_{\mathrm{vid}} + f_{\mathrm{rot}} + f_{\mathrm{tra}}) \cdot \frac{1}{2} k_{\mathrm{B}} T \;, \tag{3.6}$$

where k_{B} denotes the Boltzmann constant. Each degree of freedom contributes with a factor of $1/2 k_{\mathrm{B}} T$ to the internal energy. The mean momentum of a molecule in one spatial direction due to thermal motion is

$$p_i = \sqrt{m k_{\mathrm{B}} T} \;. \tag{3.7}$$

For instance, an ammonia dimer with mass $m = 34\,\mathrm{u}$ at room temperature $T = 293\,\mathrm{K}$ would have a momentum distributed around $p_i = 4.8$ au. Hence, in order to precisely measure the momenta of all particles, the thermal energy of the target molecules needs to be further reduced. This is achieved by taking advantage of the supersonic expansion of a gas into the vacuum.

In the experiment presented here, the gas flows through a nozzle at temperature T_0 from a vessel with the pressure p_0 (driving pressure) into the source stage with the pressure p_1. If the condition $p_0 > 2.1 p_1$ is fulfilled, the gas expands adiabatically behind the nozzle and almost the whole enthalpy H is converted into translation energy [61]. If the gas is assumed to be ideal, so that $pV = 1/2 k_{\mathrm{B}} T$, it follows that

$$H = U + pV = \left(\frac{f}{2} + 1\right) k_{\mathrm{B}} T_0 = \frac{1}{2} m v^2 \;, \tag{3.8}$$

where U denotes the internal energy with f degrees of freedom. The product pV is the pressure-volume work of the nozzle on the gas. In the expansion area behind the nozzle the interaction between the molecules due to scattering is reduced to a minimum causing all internal degrees of freedom to freeze out. The boundaries of the area arise from the fact, that the molecules start to scatter with background particles. In this so called zone of silence the molecules have a very narrow velocity distribution and the internal temperature of this motion can be estimated by [61]

$$T_{\mathrm{jet}} \approx \left(\frac{f}{2} + 1\right) \frac{T_0}{S^2} \;, \tag{3.9}$$

with $S = (2\sqrt{ln2}) \cdot v/\Delta v$ denoting the speed ratio. According to the conservation of energy, the velocity of the molecules in the zone of silence can be calculated by the difference of the enthalpy before and after the expansion:

$$v_{\mathrm{jet}} = \sqrt{\left(\frac{f}{2} + 1\right) \frac{k_{\mathrm{B}}}{m} \cdot (T_0 - T_{\mathrm{jet}})} \;. \tag{3.10}$$

In order to calculate the internal temperature T_{jet}, the speed ratio has to be empirically determined. The speed ratio depends on the driving pressure and the nozzle geometry and is usually in the order of 10 to 100 [62, 63]. Hence, the temperature in the zone of silence T_{jet} is estimated to be in the order of a few mK and can be neglected in comparison to the nozzle temperature T_0. For molecules the velocity then reads

$$v_{\mathrm{jet}} = \sqrt{\frac{f+2}{2} \frac{k_{\mathrm{B}}}{m} \cdot T_0} \;. \tag{3.11}$$

The nozzle used in the experiment has a diameter of 50 µm. The gas jet is created by cutting out a part of the gas from the zone of silence by a narrow cylinder (see 3.8). The so called skimmer with a length of 10 mm is placed 6 mm behind the nozzle. An additional pinhole with ~0.5 mm

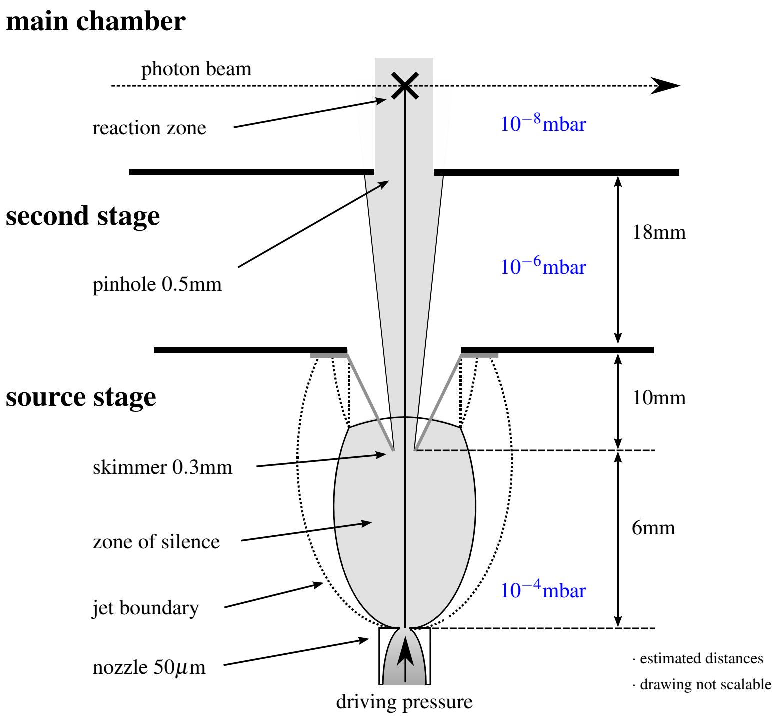

Figure 3.8: Under certain conditions the gas expands adiabatically into the source stage. By cutting out a part of the gas in the zone of silence a supersonic gas jet is created. Within the jet the molecules have a very narrow velocity distribution in direction of travel. A pinhole connecting the source stage to the main chamber limits the transversal momentum distribution (modified from [59]).

connecting the second stage with the main chamber further limits the transversal momentum distribution of the molecules in the jet, thereby defining the size of the reaction volume in the main chamber. Given this geometry the momentum spreads in the jet can then be calculated:

$$\Delta p_{\perp} = \sqrt{fmk_{\mathrm{B}}T_0} \cdot \frac{d_{\mathrm{N}} + d_{\mathrm{P}}}{l} \quad \text{transversal jet momentum} \tag{3.12}$$

$$\Delta p_{\parallel} = \sqrt{fmk_{\mathrm{B}}T_0} \cdot \frac{2\sqrt{ln2}}{S} \quad \text{parallel jet momentum} \tag{3.13}$$

Here d_{N} denotes the diameter of the nozzle and d_{P} the diameter of the pinhole, respectively.

During the experiment the preparation of a gas jet containing the desired target molecules $NH_3 \cdots NH_3$ and $H_2O \cdots H_2O$ was challenging. For that purpose the gaseous ammonia was bubbled through the liquid water in the reservoir. Depending on the driving pressure of the ammonia and the temperature of the reservoir, the tubes and the nozzle the gas jet had different molecular compositions. The concentration of water relative to that of ammonia was hardly controllable. Consequently the experimental conditions for the target molecules were constantly changing. These circumstances during the measurement are discussed in detail in Section 5.4.

3.2.3 Spectrometer

The spectrometer is the central part of the COLTRIMS setup. Inside of the spectrometer the photon beam intersects with the gas jet inducing the reactions under investigation. It is build in a cylindric geometry and is equipped with detectors on both ends, one for detecting the electrons and one for the ions. A linearly increasing potential along the copper plates in the acceleration

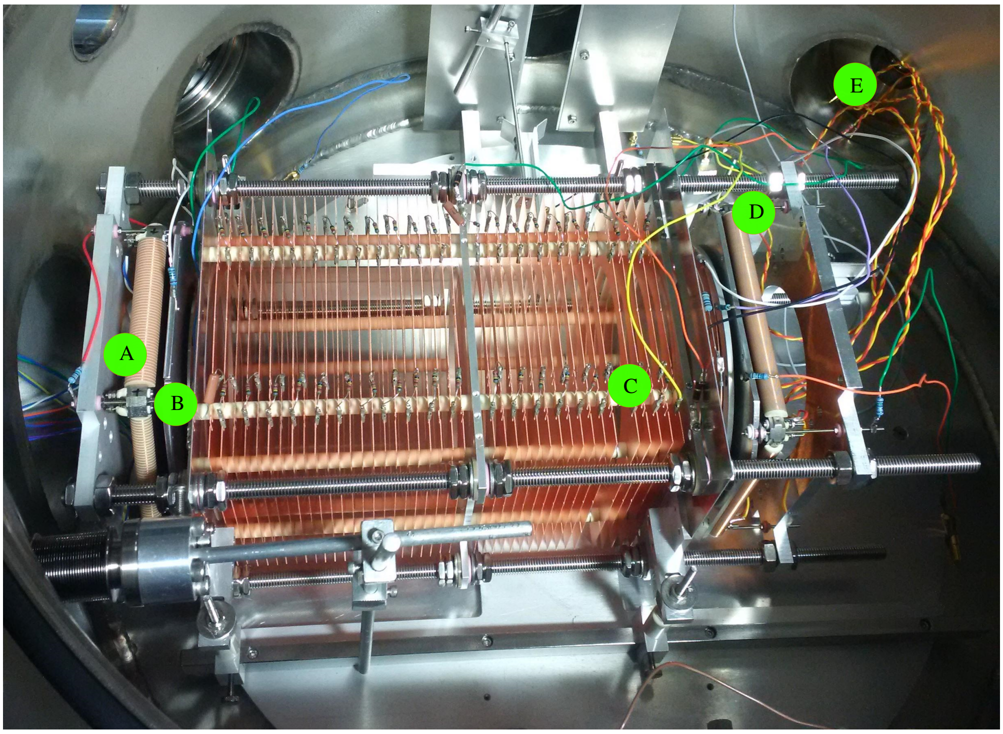

Figure 3.9: During the measurement the spectrometer sits horizontally in the main vacuum chamber. On the left side **(A)** the hexagonal anode and **(B)** the MCP for detecting the electrons. At **(C)** is the reaction zone located. On the right side **(D)** the quad anode with the MCP right in front of it. **(E)** shows where the wires of the ion side are fed through and connected to the electronics and the power supplies outside of the chamber.

region creates a homogeneous electric field separating electrons and ions after the fragmentation of the molecule. The electron arm of the spectrometer is build in the Wiley-McLaren geometry featuring a long field-free drift region for an optimal time focus [64]. The ion side consists of the acceleration region followed by an extended boost region. All regions with different electric fields are separated by fine metallic meshes shielding from potential reach-through. During the experiment the spectrometer sits horizontally in the main chamber as it is shown in Figure 3.9.

Geometry and settings

Figure 3.10 shows a detailed drawing of the spectrometer. It is built of 39 equidistant copper plates that are 0.4 mm thick and mounted on ceramic rods with a gap of 5 mm between each other. In the experiment the mesh on the ion side was set to a potential of $-157\,\mathrm{V}$, whereas the mesh at the other end of the acceleration region was set to $-100\,\mathrm{V}$. All copper plates are connected by $600\,\mathrm{k\Omega}$ resistors ensuring that the potential changes linearly alongside the region. With a length of 107 mm of the total acceleration region, the electric field theoretically calculates ~$5.327\,\mathrm{V\,cm^{-1}}$. After being accelerated the electrons pass through a 138 mm long field-free drift region until they enter the boost region. The electron micro channel plate (MCP) sits 5 mm behind the mesh at the end of the drift region. Its front is set to a potential of 200 V, so that the the boost field is $600\,\mathrm{V\,cm^{-1}}$. This short strong acceleration field ensures that the electrons trigger the detector regardless of their kinetic energy (details on the detectors in Section 3.2.4).

The ions are guided towards the other side of the spectrometer. After being accelerated over 36.5 mm, they reach the ion mesh mounted on an aluminium holder with 4 mm thickness. In

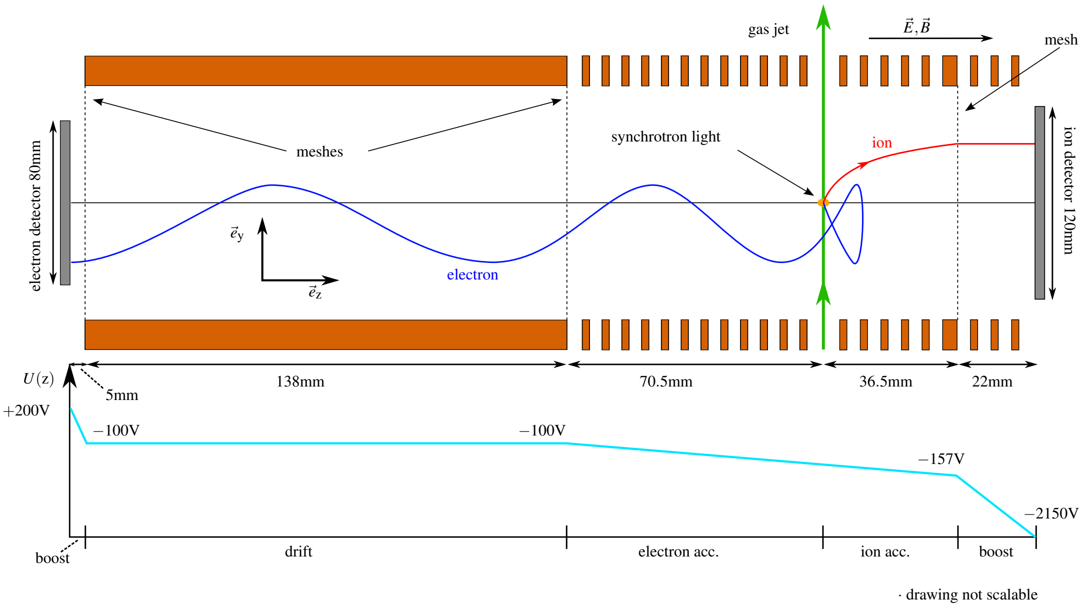

Figure 3.10: Schematic of the spectrometer. The electron arm is built in the Wiley-McLaren geometry (drift and acceleration length in 2:1) for optimal time focus. The ion side has an expanded boost region and the mesh facing towards the MCP in order to reduce the reach-through of the strong potential of the MCP. The electric field strength is chosen so that all electrons and ions given their expected kinetic energy are captured.

previous experiments with this spectrometer the mesh was mounted on the left side of the holder facing towards the electron detector. However, in order to force back the reach-through of the strong potential of the ion MCP (also called fringe field) the mesh was placed on the right side of the holder extending the acceleration from 32.5 mm to 36.5 mm. For the same reason the boost region accelerating the ions onto the MCP was extended. Setting the MCP front to $-2150\,\mathrm{V}$ makes the potential decrease by 1993 V over 22 mm resulting in a boost field of $906\,\mathrm{V\,cm^{-1}}$ for the ions. Another modification reducing the fringe field was done by replacing the $600\,\mathrm{k\Omega}$ resistor between the last copper plate of the acceleration region and the ion mesh holder with an adjustable resistance (potentiometer). By tweaking the potentiometer, the electric field can be increased at the end of the acceleration, thus compensating the potential fringe field. The effect of these modifications are discussed in detail in Section 4.4.

The lengths of the drift and acceleration region on the electron side have a ratio of 2:1. This so called Wiley-McLaren geometry assures an optimal time focus. As illustrated in Figure 3.11, this means that electrons, which have the same initial velocity v_z, also have the same ToF regardless their starting point in the reaction zone [64]. Due to the finite volume of the reaction zone (~1 mm in z-direction and ~1 mm in y-direction determined by the focus of the photon beam and ~1 mm in x-direction determined by the gas jet) electrons can be produced at different distances to the electron MCP. However, if an electron starts with greater distance to the detector, it gains more kinetic energy due to a longer acceleration and enters the drift region with higher velocity. In the field-free drift region it then catches up with electrons that started with the same initial velocity but a shorter distance to the MCP. If the drift length is exactly two times the acceleration length, all electrons will reach the end of the drift region at the same time.

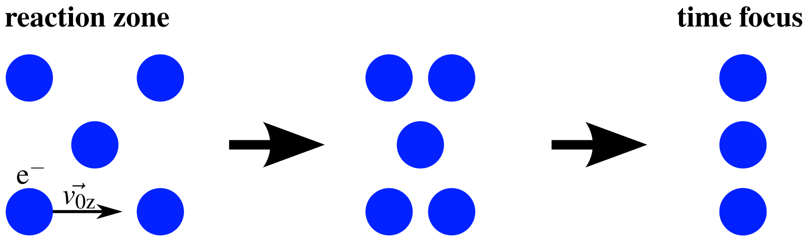

Figure 3.11: Left: In the finite reaction volume electrons with the same initial velocity v_{0z} can start at different distances to the detector, i.e. different positions on the z-axis. **Right:** After a certain distance of acceleration and drifting all electrons are on the same hight. This time focus is achieved, if the drift length and the acceleration length have a ratio of 2:1.

3.2.4 Detectors and data acquisition electronics

The detectors consist of two parts, the micro channel plates (MCP), that are used for measuring the ToF of the particles, and the delay line anode, which is used for obtaining the position information of a detected particle. The detector system typically has a spatial resolution of $< 100\,\mu m$ and a time resolution of $< 0.2\,ns$ [65].

Micro-channel plates

A micro-channel plate, depicted in Figure 3.12a, is a thin layer of millions of stacked narrow tubes. Each tube has a diameter of ~25 µm and is around 1.5 mm long. The distance to the next neighbor tube is of the same order than its diameter, so that the whole layer has an open area of 50% or more. Macroscopically the MCP usually has the shape of a disk. In this experiment the diameter of the ion MCP was 120 mm and of the electron MCP 80 mm. The front and back surface of the MCP, both covered with a metallic layer, are set to different potentials, thereby creating a very strong electric field of ~$1000\,\mathrm{V\,mm^{-1}}$ along the tubes.

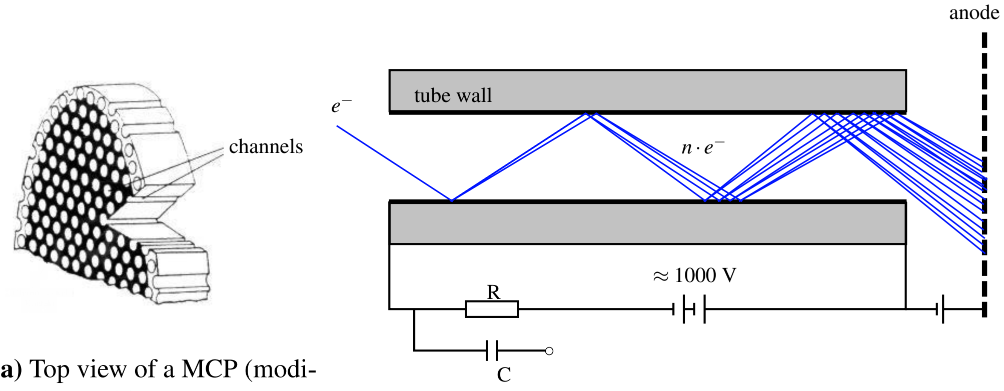

(a) Top view of a MCP (modified from [66]).

(b) Individual electron multiplier tube.

Figure 3.12: (a) A micro channel plate is a 1.5 mm thin layer with millions of stacked individual electron multiplier tubes. The usual ratio of length to diameter of a tube is in the range of 60 to 120. **(b)** If an energetic particle hits the semiconducting tube wall, it ejects secondary electrons that are accelerated in the strong electric field along the tube and in turn liberate electrons. The voltage fluctuation created by the avalanche of secondary electrons can be capacitively decoupled.

The walls on the inside of the tubes are coated with a semiconductor material featuring a low work function. Usually the tubes are tilted by a few degrees to prevent incoming particles from passing through without interacting. If an particle such as an ion, electron or photon with sufficient kinetic energy hits the tube walls, one or more secondary electrons are ejected. In the electric field they are immediately accelerated along the tube. Once they have gained enough kinetic energy, they in turn liberate further electrons as illustrated in Figure 3.12b. By this multiplying effect an avalanche along the tube is formed containing up to more than 10^6 electrons. The signal required for the time measurement can then be obtained by capacitively decoupling (RC highpass filter) the resulting voltage fluctuation between the MCP front and back. Assuming that each electron cloud needs the same time to travel through the tube, time signals can be attained with a resolution of 0.2 ns.

The MCPs used in the presented experiment are made out of two layers which are rotated by 180° with respect to each other so that the channels have a kink at half way. With this so called chevronThe word " chevron" describes a v-shape. In a chevron MCP the channels have a v-like form. MCP stack sufficient amplification is obtained and potential liberated secondary ions can be prevented from traveling back into the spectrometer and mistakenly being detected. Due to the fact, that the tubes are very narrow and densely packed, the created electron clouds are precisely located at the back of the MCP, where they can than be detected by the delay line anodes.

Delay line anodes

Right behind the MCPs the delay line anodes are attached which measure the positions of the detected particles. As seen in Figure 3.13, a delay line anode consists of two or three layers of coiled copper wires mounted on an isolating holder. The copper wires sit on lower potential than the MCP, hence attracting incoming avalanches of electrons. If an electron cloud hits the wires, a signal is created traveling from the position of impact to both ends of the wire, where it is recorded. The traveling time to each end is calculated relatively to the trigger signal. Assuming that the traveling speed of a signal is constant along the wire the sum of both time signals in one dimension is constant:

$$t_{\mathrm{sum,i}} = (t_{i,1} + t_{i,2}) - 2 \cdot t_{\mathrm{MCP}} \,, \tag{3.14}$$

with $i = u, v, w$ denoting the layer. The run times t used for the position reconstruction have negative values as they are calculated by the TDC as time differences (see Section 4.1). With this information the initial position of the impact can be calculated.

With a quad anode four signals are acquired, while each layer gives information about the position in one dimension. A hex anode produces six signals, thus providing more information than necessary. However, if two particles hit the MCP at the same time or within a time interval smaller than multiple hit dead time, the hex anode covers a larger area where these multi hits still can be resolved in position. Beside its improved multi hit ability, the hex anode also allows the user to reconstruct events in case of information loss using the additional information. In both anodes the signal quality in high frequency range is improved by using two wires per layer with a potential difference of ~50 V (Lecher line). The signal is carried by the signal line, whereas the electric noise is carried by both wires. In order to obtain a clear signal without background noise both signals are subtracted from each other.

(a) Stack of MCP and quad anode

(b) Hex anode

Figure 3.13: **(a)** For the ion detector a quadratic delay line anode with two layers and a width of 120 mm was used (taken from [59]). **(b)** For the electron detector a hexagonal delay line anode with a width of 80 mm was used. It has three layers with a relative angle of 60° (taken from [67])

.

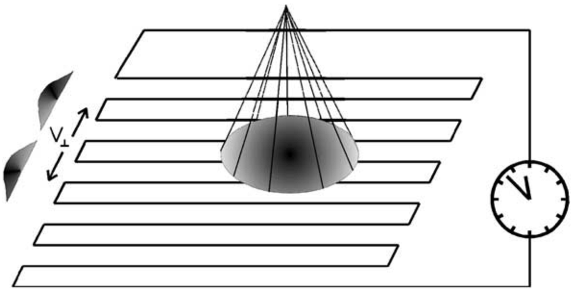

Figure 3.14: The time sum of the signals traveling towards both ends is constant. The position of the impact can be calculated from the time difference (modified from [68]).

Signal acquisition and processing

As mentioned in Section 3.2.4, the very fast voltage fluctuations on the MCPs and the delay line anodes are extracted by a highpass filters sitting in so called decoupling boxes outside the main chamber. They are equipped with LEMO[2] connectors and potentiometers for tuning the RC-elements. Since the signals are in the order of 10^2 mV, they must be amplified. This is done by fast amplifier modules. In order to precisely measure the time between two signals, well-defined reference points, which do not depend on the shape of the analog signals, are required. Therefore, the signals are modified by so-called constant-fraction discriminators (CFT). The pulses are duplicated, inverted and superposed with a relative time delay. The resulting zero-crossing is then independent of the height and width of the pulse and can be used as reference point.

Further processed by electronic modules such as delays logical gates, the signals are then handed over to the time-to-digital converter (TDC). The TDC is an electronic module that measures time differences between the signals on its channels with a accuracy smaller than 25 ps. Controlled by the software CoboldPC [69] the data is then saved from the TDC memory to the computer as list mode files (*lmf*). During the experiment millions of events were saved with a total data volume of 1.3 Terabytes. The events were stored only, if they contained two ion hits and at least one electron hit. Figure 3.15 schematically shows how the detected hits are electronically selected. First the electron opens a gate, that is longer than the bunch spacing of 328.3 ns, for recording a few bunch marker signals of the beamline (GATE_1 and AND_1 in Figure 3.15). These bunch markers are used as a time reference in the ToF calculation. The signal, which triggers data storing, is created by requiring a triple-coincidence. The first electron opens another gate (GATE_2 in Fig. 3.15), typically 1 µs long and delayed by ~3 µs, to record the ions. The first ion opens a gate longer than the maximal ToF of the recoils. Combining this gate with the second ion by a logical AND a recoil-recoil-coincidence signal is created. This recoil-recoil-coincidence signal is in turn combined with the open electron gate by another logical AND thereby creating the triple-coincidence signal which then triggers the data storage.

---

[2] Nuclear Instrumentation Standard

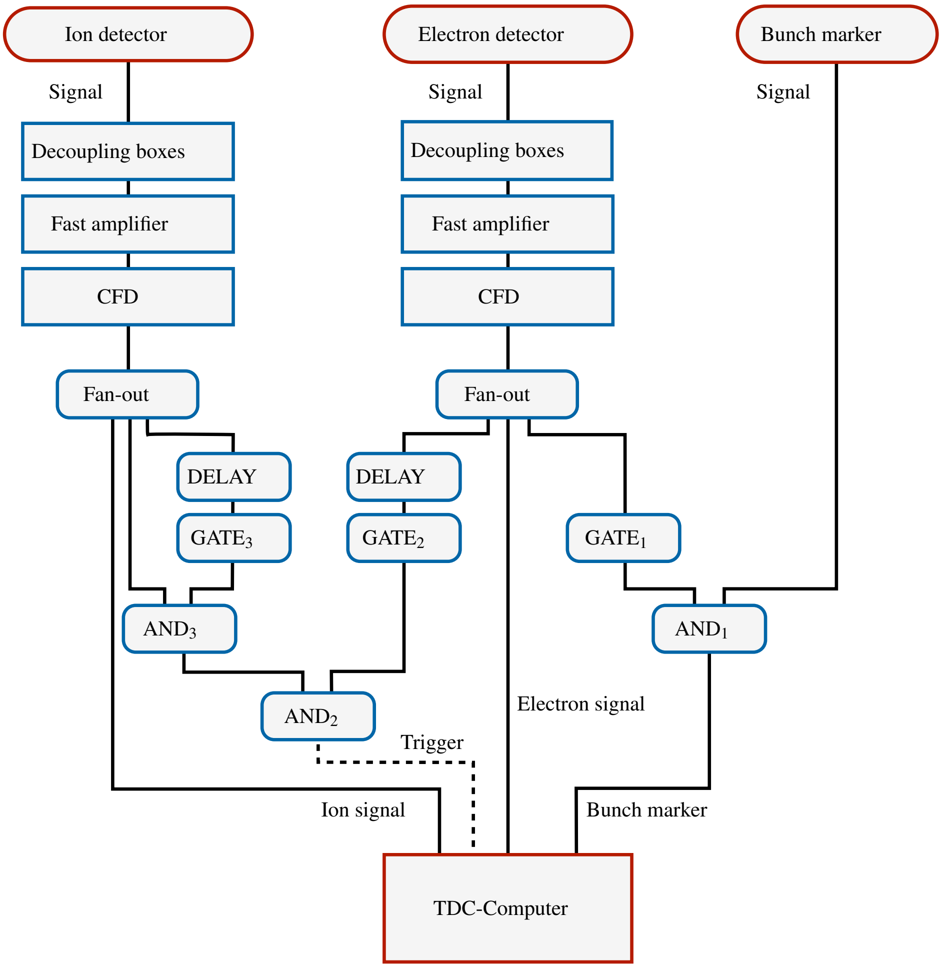

Figure 3.15: The signals from the MCPs and the delay line anodes are decoupled by highpass filters and further modified by fast amplifiers and constant fraction discriminators. The processed MCP time signals of electron and ion detector then have to fulfill certain conditions ensuring a three-particle coincidence, which allows the TDC to store the data (modified from [70]).

Chapter 4

Data Analysis

The raw data collected during a COLTRIMS experiment is encoded as times. The time signals received from the synchrotron, MCPs and delay line anodes have to be converted into ToF and position information for each particle of an event (see Section 4.1). Here, an event describes the reaction that created the particles measured in coincidence. In the case of ICD an event consists of four detected particles, two ions and two electrons. After preprocessing the data, the obtained ToF and position information is used for the reconstruction of the initial momentum vectors of all particles by solving the corresponding equations of motion (see Section 4.2).

Since theoretical considerations regarding the experimental setup seldom perfectly matches with the results, thorough calibrations need to be undertaken (see Section 4.2). As a first step the detectors are calibrated so that the signal preprocessing leads to the correct ToF and position information. Then, the spectrometer is calibrated. Therefor photoionization of helium and double ionization of nitrogen have been measured. The spectrometer geometry and the applied $\vec{E}$- and $\vec{B}$-field are adjusted so that the calculated momenta and energies correspond to the literature values. In Section 4.4 the correction of the field inhomogeneities is described which was crucial for the success of the calibration. The actual analysis was not carried out using all recorded data. Instead, only a small proportion containing the relevant events was taken into consideration. In order to select these events, all data stored in *lmf*-files was presorted by setting specific conditions on the ion ToF while requiring a three particle coincidence. Hereby, different potential breakup channels of the target systems $NH_3 \cdots NH_3$ and $NH_3 \cdots H_2O$ were cut out and saved in different files (see Section 4.5). Both, the presorting and the subsequent data analysis was performed using the self-made C++ program *lmf2root* which is based on the ROOT data analysis framework[1] developed at CERN.

4.1 Data preprocessing

For each event the TDC acquires multiple time signals as listed in Table 4.1. All time signals are clock times with a random absolute value θ. However the TDC stores the time differences between the trigger and each of the other time signals. Hence, the measured times have negative values. For example the MCP time is calculated $t_{\text{MCP}} = \theta_{\text{MCP}} - \theta_{\text{trigger}}$. Using these relative times $t = \Delta\theta$, the important ToF and position information can be extracted.

---

[1] More information about the software ROOT can be found on `https://root.cern.ch/`. For the data analysis, version 5.27.04 was used.

Table 4.1: Raw time signals θ sent to the TDC for each event. The TDC calculates relative times starting from the trigger signal and then saves the TDC times t to the computer.

θ_{BM}	denotes the bunchmarker signal which is sent in sync with the circulating electron bunches in the synchrotron. It serves as a time reference indicating when the photons enter the target chamber.
$\theta_{\mathrm{X,MCP}}$	is the MCP signal. It is created when a particle strikes on the MCP. The index $\mathrm{X} = \mathrm{e},\mathrm{r}$ denotes the type of particle.
$\theta_{l,i}$	are the time signals recorded at each end of one delay line. The index $i = 1,2$ indicates at which end the signal was acquired while $l = u,v,w$ denotes the layer. For an ion hit only four signals are acquired due to the missing third layer of the quad anode.
$\theta_{\mathrm{trigger}}$	denotes the signal triggering the TDC to save the collected signals.

4.1.1 Time-of-flight (ToF)

The time-of-flight of a particle is the difference between the instant of its creation during the reaction and the instant of its detection by the MCP. Except an arbitrary offset, which can be determined from the data (see Section 4.3.2), the bunchmarker time t_{BM} denotes the start time of the particle flying towards the detector. The MCP time $t_{\mathrm{X,MCP}}$ denotes the end time. The time-of-flight of an electron is then calculated by

$$\mathrm{ToF_e} = f_{\mathrm{mod}}(t_{\mathrm{e,MCP}} + t_{\mathrm{offset}} - t_{\mathrm{BM}} + 1000 \cdot \mathrm{BM_{period}}, \mathrm{BM_{period}}) , \qquad (4.1)$$

with $f_{\mathrm{mod}}(a,n)$ denoting the modulo function which ensures to calculate the correct difference between bunchmarker and MCP time. Since the sum of MCP time and ToF of each particle must give the difference between $\theta_{\mathrm{trigger}}$ and the instant of the reaction, the time-of-flight for an ion is calculated by:

$$\mathrm{ToF_r} = t_{\mathrm{r,MCP}} - t_{\mathrm{e,MCP}} + \mathrm{ToF_e}. \qquad (4.2)$$

Note that $t_{\mathrm{X,MCP}}$ are negative values.

4.1.2 Reconstruction of real-space coordinates

As mentioned in Section 3.2.4, the particle impact on the detector can be located by using the TDC runtimes of the signals $t_{l,i}$ on each delay line. Within the coordinate system of the delay lines the position on one layer axis, for instance the u-layer, is calculated by

$$u = \frac{1}{2f_u}(t_{2,u} - t_{1,u}) , \qquad (4.3)$$

where $f_u = {}^1\!/_{v_u}$ depends on the propagation velocity of the signal along the wire. The position on the layers can then be expressed in real-space coordinates after a coordinate transformation. For this purpose, quad- and hex-anode have to be treated separately.

Quad-anode

On the quad-anode, which is used for detecting the ions, the layer axes u, v are the same as the Cartesian coordinate axes x, y. Hence, the coordinates correspond to each other [71]:

$$\begin{aligned} x_\mathrm{r} &= u_\mathrm{r} && (4.4) \\ y_\mathrm{r} &= v_\mathrm{r} \,. && (4.5) \end{aligned}$$

The conversion factors for both layers listed in Table 4.2 are manually determined by correcting distortions of the shape of the detector until the cut-off of the ion detector image is a circle with 120 mm diameter. Due to the perpendicularity of the coordinate axes the coordinates are transformed independently from each other.

Table 4.2: Layer conversion factors of the quad-anode in [mm/ns].

Layer	**Conversion factor** [mm/ns]
u	0.4311
v	0.4064

Hex-anode

In a hex-anode, such as the one used for the electron side, the layers are rotated by 60° to each other and the Cartesian coordinates are obtained by the transformations [71]

$$\begin{aligned} x_{uv} &= u && (4.6) \\ y_{uv} &= \frac{1}{\sqrt{3}}(u-2v) && (4.7) \\ x_{uw} &= u && (4.8) \\ y_{uw} &= -\frac{1}{\sqrt{3}}(u+2w) && (4.9) \\ x_{vw} &= (v-w) && (4.10) \\ y_{uw} &= -\frac{1}{\sqrt{3}}(v+w) \,, && (4.11) \end{aligned}$$

where all set of coordinates are equal. Hence, if the information of one layer is missing the position can still be reconstructed using the other layers. Unlike the scaling factors of the quad anode, the factors of the hex-anode have to be consistent with respect to each other. Therefore, the factors are determined by iteratively adjusting two of them with respect to the third one until the electron detector image is circular with diameter of 80 mm.

Table 4.3: Layer conversion factors of the hex-anode in [mm/ns].

Layer	**Conversion factor** [mm/ns]
u	0.5480
v	0.5302
w	0.5260

4.2 Momentum calculation

Using the information about the ToF and impact position of each particle, the initial momentum vector of the particle can be reconstructed. Thereby the ToF component z and spatial components x and y are considered separately. The acceleration along the spectrometer axis by the different electric fields is one-dimensional, whereas the accelerations along the spatial components are entangled due to the Lorentz force.

4.2.1 ToF component

Both, the electrons and ions, are accelerated by different electric fields along the spectrometer axis z. The electron side consists of three regions: acceleration, drift and boost. On the ion side there are only two regions: acceleration and boost. However, by using a general solution the momentum of both particles in the z-direction can be calculated with the same function.

The reconstruction is performed by assuming three general acceleration regions: a_1, a_2 and a_3 with the lengths x_1, x_2 and x_3. For each region the same simple equation of motion holds

$$
\begin{aligned}
x_1 &= v_0 t_1 + \frac{1}{2} a_1 t_1^2 && (4.12)\\
x_2 &= v_1 t_2 + \frac{1}{2} a_2 t_2^2 && (4.13)\\
x_3 &= v_2 t_3 + \frac{1}{2} a_3 t_3^2 \, , && (4.14)
\end{aligned}
$$

with s_i the traveled distance in the according region. v_0 is the initial velocity, $v_1 = v_0 + a_1 t_1$ and $v_2 = v_0 + a_1 t_1 + a_2 t_2$ the entering velocity in the second and third region, respectively. The theoretical total time-of-flight t_{theory} of a particle is given by the sum of the times

$$
\begin{aligned}
t_1 &= \frac{-v_0 + \sqrt{v_0^2 + 2a_1 x_1}}{a_1} && (4.15)\\
t_2 &= \frac{-v_1(v_0,t_1) + \sqrt{v_1^2(v_0,t_1) + 2a_2 x_2}}{a_2} && (4.16)\\
t_3 &= \frac{-v_2(v_0,t_1,t_2) + \sqrt{v_2^2(v_0,t_1,t_2) + 2a_3 x_3}}{a_3} && (4.17)
\end{aligned}
$$

that it need to pass all three regions:

$$t_{\text{theory}} = t_1 + t_2 + t_3 \, . \qquad (4.18)$$

This theoretical time-of-flight solely depends on the unknown initial velocity v_0. The idea is to find the right value of v_0 so that $t_{\text{theory}} = \text{ToF}$. In the data analysis this is achieved by determining the root of the function

$$\Delta t(v_0) = t_{\text{theory}}(v_0) - \text{ToF} \qquad (4.19)$$

in an iterative process called Newton's method. Taking only a few iterations this method is very efficient in case the electric fields are uniform, so that the accelerations a_i are constant within the corresponding regions. However, in case of an inhomogeneous field, the reconstruction becomes more elaborate and other methods such as using look-up tables become more suitable as explained in Section 4.4. With the correct initial velocity the ToF component of the momentum

Table 4.4: Parameters of the electron side of the spectrometer used in the momentum calculation.

$x_1,\ a_1$	Acceleration region with a low electric field.
$x_2,\ a_2 = 0$	Relatively long drift region without an electric field.
$x_3,\ a_3$	Short boost region with high electric field.

Table 4.5: Parameters of the ion side of the spectrometer used in the momentum calculation.

$x_1,\ a_1$	Acceleration region with a low electric field.
$x_2,\ a_2$	Short boost region with high electric field.
$x_3 = 0,\ a_3 = 0$	No third region implemented.

is then simply given by

$$p_{\mathrm{z}} = m \cdot v_0(\mathrm{ToF}) \ , \tag{4.20}$$

with m denoting the mass of the particle.

The input for the reconstruction of the ToF component according to the spectrometer geometry is shown in Table 4.4 for the electrons and in Table 4.5 for the ions. Their exact values are determined in the spectrometer calibration presented in Section 4.3.5.

4.2.2 Spatial components

The spatial components of the momentum vector p_{x} and p_{y} are not affected by the electric field and can be reconstructed by using the position information of the impact of the particle on the detectors.

Electrons

To capture the fast electrons an additional magnetic field is applied, which forces the electrons onto a spiral-shaped trajectory. The equations of motion can be derived to

$$x(t) = \frac{1}{m_{\mathrm{e}}w}\left[p_{\mathrm{x}}sin(wt) - p_{\mathrm{y}}(cos(wt)-1)\right] , \tag{4.21}$$

$$x(t) = \frac{1}{m_{\mathrm{e}}w}\left[p_{\mathrm{x}}(cos(wt)-1) + p_{\mathrm{y}}sin(wt)\right] \ , \tag{4.22}$$

where $w = \frac{e \cdot |\vec{B}|}{m_{\mathrm{e}}}$ is the gyration frequency. The solutions for the spacial momentum components are

$$p_{\mathrm{x,e}} = \frac{m(b \cdot x - a \cdot y)}{a^2 + b^2} \tag{4.23}$$

$$p_{\mathrm{y,e}} = \frac{m(a \cdot x + b \cdot y)}{a^2 + b^2} \ , \tag{4.24}$$

with

$$a = \frac{1 - cos(w \cdot \mathrm{ToF_e})}{w} \quad , \quad b = \frac{sin(w \cdot \mathrm{ToF_e})}{w} \ . \tag{4.25}$$

Here x and y denote the coordinates of the impact on the electron detector after the measured flight time $\mathrm{ToF_e}$. It is important to note that for $w \cdot \mathrm{ToF_e} = n \cdot 2\pi$ the formula diverges. This is, because after n full gyrations all electrons fall into the same spot in the xy-plane. Hence, these so called nodes do not contain any information about the initial transversal motion of the electron so that the z-component is the only spatial component that is reconstructible.

Ions

The transversal motion of the ions is barely influenced by the magnetic field due to their relatively heavy mass. Therefore, the effect of the magnetic field can be neglected in the calculations. The transversal components of the initial momentum of the ions is given by

$$\begin{aligned} p_{\mathrm{x,r}} &= m_{\mathrm{r}} \frac{x}{\mathrm{ToF_r}} && (4.26) \\ p_{\mathrm{y,r}} &= m_{\mathrm{r}} \frac{y}{\mathrm{ToF_r}} \, , && (4.27) \end{aligned}$$

with x and y denoting the position of the impact on the ion detector.

4.3 Calibrations

In order to achieve correct results in the data preprocessing and momentum calculation the detectors and the spectrometer must be thoroughly calibrated.

4.3.1 Delay line time sums

As mentioned in Section 3.2.4, the sum of the signal run times $t_{i,1}$,$t_{i,2}$ must be constant. This is an important condition for an accurate reconstruction of the real-space positions on the detector. However, real data shows a different picture as it can be seen in Figure 4.1a. In reality the propagation velocity of the signals varies with the location of the impact of a particle on the delay line. This is corrected by a routine shifting the time sums to the same value for all calculated positions on the layer. In Figure 4.1b this is exemplarily shown for the v-layer of the electron and recoil detector. Furthermore, the time sum is shifted to zero so that the reconstruction algorithm can work properly. The time windows Δt_{sum} were set to ± 3 for the recoil detector and ± 1 for the electron detector. Hence, the reconstruction algorithm discriminated reflections and other background by only considering time sums within the set windows.

4.3.2 Time-of-flight offset and magnetic field

When calculating the time-of-flight of electrons, Equation 4.1 is used. In theory the time-of-flight is the time difference between the instant when the electron is born and the instant of impact on the detector. Even though the bunchmarker signal is in sync with the photons reacting with the target, the sinal is shifted by an unknown period. In addition, the MCP signal is randomly delayed by the electronics. The overall time shift was ~198 ns and was roughly adjusted already in an on-the-fly data analysis during the measurements. For the fine adjustments, data was taken with a very low electric field so that the electrons were able to make a couple of gyrations before hitting the detector (“wiggle run”). By plotting the time-of-flight of the electrons against one of their position coordinates, the residual time offset t_{offset} can be identified.

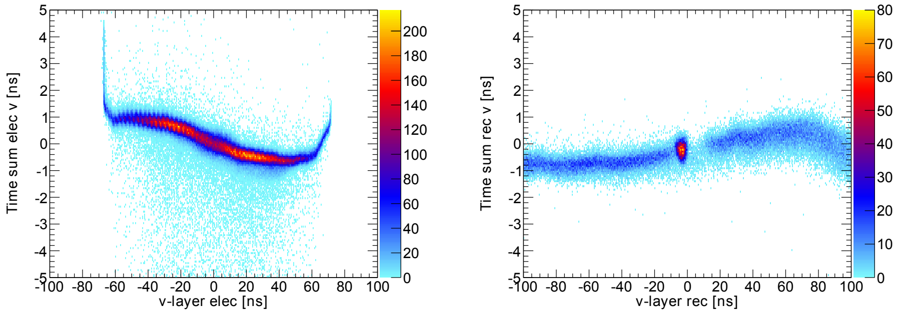

(a) Uncorrected time sum.

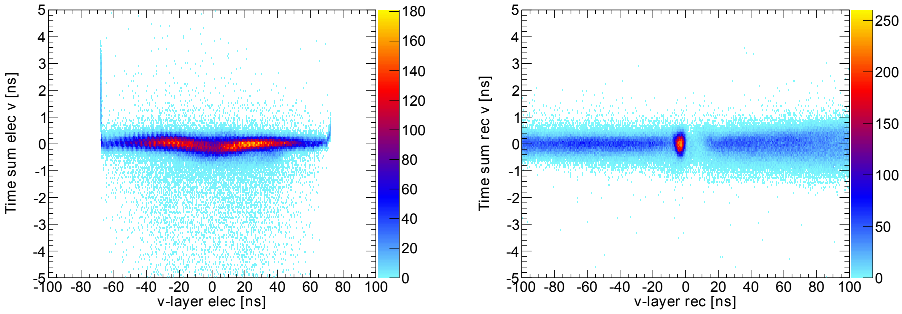

(b) Corrected time sum.

Figure 4.1: **(a)** Before running the correction routine, the sum of both signal run times varies depending on the position of the impact. **(b)** After performing the correction, the time sum is flattened and shifted to zero.

Table 4.6: From the linear fit with equation $y = a \cdot x + b$ in Figure 4.2b the time offset, the gyration period and the magnetic field are determined.

Variable	**Value**
t_{offset}	$0.5 \pm 0.5\,\text{ns}$
T_{gyr}	$52.1 \pm 0.2\,\text{ns}$
$\lvert\vec{B}\rvert$	6.86 ± 0.03 Gauss

The plot with the ToF versus one position coordinate shown in Figure 4.2a is often referred to as " fish spectrum". The nodes in this spectrum are equidistant. Hence, the time offset is given by the intercept of a linear fit through the nodes as illustrated in Figure 4.2b. From this plot further information can be extracted. The slope of the linear fit represents the average gyration period. Using equation

$$T_{\text{gyr}} = \frac{2\pi \cdot m_{\text{e}}}{e \cdot |\vec{B}|} \tag{4.28}$$

the strength of the magnetic field $\vec{B}$ is determined. $\vec{B}$ is used for the momentum calculation. Table 4.6 shows the results for the time offset and the gyration period.

4.3.3 $\vec{E} \times \vec{B}$ drift

The motion of the electrons in the spatial directions x and y is decoupled from the ToF-direction only if the electric and magnetic field are exactly parallel. If this is not the case, the electrons drift perpendicularly to the ToF-direction ($\vec{E} \times \vec{B}$-drift). In order to check for the $\vec{E} \times \vec{B}$-drift, the spatial positions of the nodes are measured using the data from the "wiggle run". The results shown in Figure 4.3.3 indicate a small drift of $-3.5\,\mu\text{m/ns}$ in the x-coordinate and $1.2\,\mu\text{m/ns}$ in the y-coordinate. However this drift occurred over long time periods of ~200 ns. Since the ToF of the electrons during the actual measurement was significantly shorter due to a higher electric field, the $\vec{E} \times \vec{B}$-drift was vanishingly small. Therefore, a correction is not required at this point.

4.3.4 Detector orientation

The detectors mounted on the spectrometer face each other. During the measurement they are placed in the reaction chamber while being connected to the electronics outside of the chamber. Under these circumstance it can happen that the information of which signal is assigned to which layer of the delay line anodes gets lost. However, for the momentum reconstruction it is important that the motions of the electrons and the ions are considered in the same absolute coordinate system. Hence, the orientation of the detectors must be checked as part of the calibration.

For calibration purposes, the single ionization of neon described by the reaction equation

$$\text{Ne} + \gamma \longrightarrow \text{Ne}^{+} + \text{e}^{-}_{\text{photo}} \tag{4.29}$$

was measured using a photon energy of ~21.6 eV which is slightly below the single ionization threshold of helium. Instead of being directly ionized, the helium atoms are excited into a high electronic state (Rydberg state). After reacting with a photon in the reaction zone, the excited helium atoms in the gas jet travel further towards the jet dump. Because the electrons in the Rydberg state are weakly bound, there is a probability of the electrons getting shifted into the

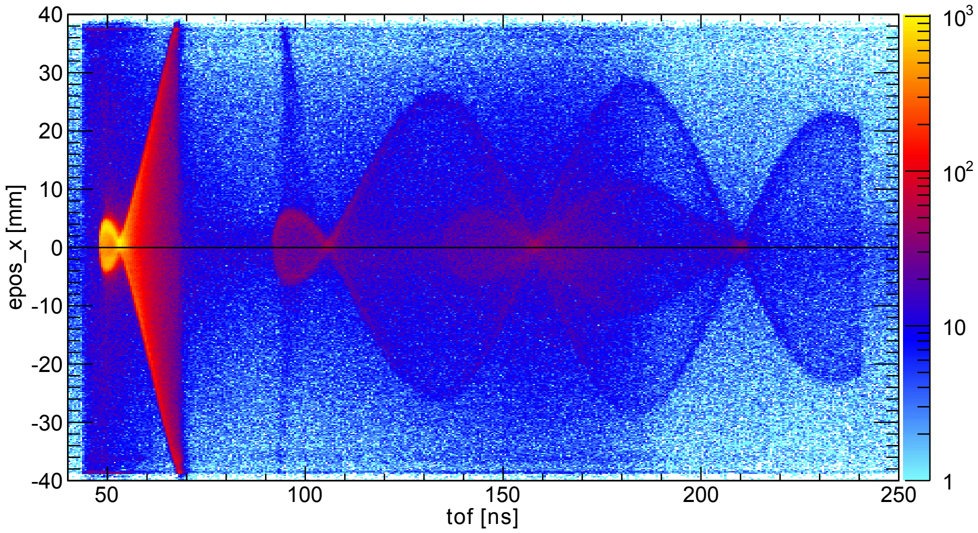

(a) x-coordinate of the position of the electrons plotted against the ToF.

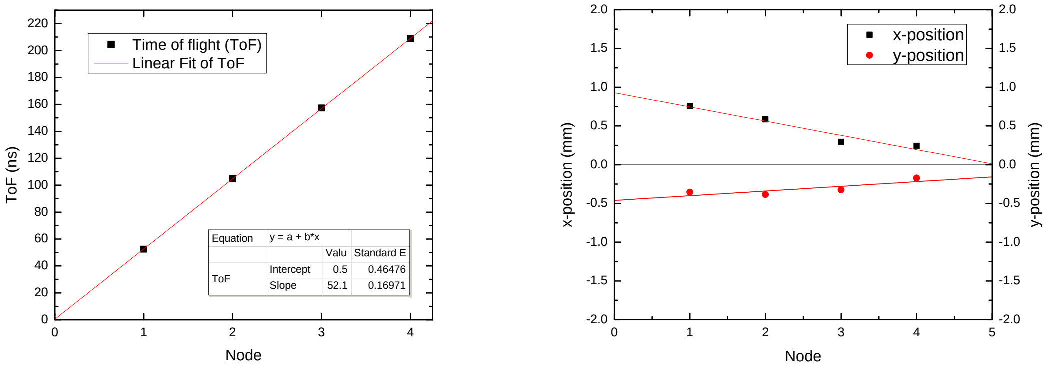

(b) Equidistant nodes in time.

(c) x- and y-position of nodes.

Figure 4.2: **(a)** During a so called “wiggle run” photoelectrons of helium in a low electric field are detected. Plotting the x-coordinate of the electrons against their time-of-flight, shows the projection of their circular motion. **(b)** The the position of the nodes in ToF-direction is plotted. The gyration period and the time offset is obtained with a linear fit. **(c)** The spatial position of the nodes is shown. Ideally all nodes are positioned at $x = y = 0$. If their position coordinates show a trend, the electric and magnetic field are not parallel ($\vec{E} \times \vec{B}$-drift) and the position of the electrons as a function of the ToF needs to be corrected.

Table 4.7: Coordinate system of the particles with respect to the setup.

$\vec{x}$	Direction of the photon beam.
$\vec{y}$	Direction of the gas jet.
$\vec{z}$	Spectrometer axis or ToF-direction.

continuum solely by the influence of the spectrometer field. Once a helium atom is ionized while still in the spectrometer, the withdrawn photoelectron and the ion are coincidently detected. In this way, an image of the gas jet appears on the electron and ion detector.

Beside field ionization, there is another side effect of the measurement that can be used to determine the relative orientation of the detectors. Despite the high vacuum in the main chamber, there are still enough background particles such as oxygen, nitrogen or water which the photons can interact with. Hence, not only in the reaction zone but also along the photon beam throughout the whole chamber particles get photoionized. These ionized particles leave a broad trace on both detectors which is called hot gas stripe.

The hot gas stripe together with the jet trace almost distinctly indicate the orientation of each detector. As seen in Figure 4.3, the electron detector has to be rotated by 120° and the recoil detector by $-90°$ in order to be correctly aligned. The mutual coordinate system, which represents the laboratory system for all calculations, is described in Table 4.7.

Although the orientation of the detectors seems to be correct, the direction of the beam can still be mirrored. In order to ascertain the correct direction of the $\vec{x}$-axis, the momentum calculation is validated. According to momentum conservation the electron must transfer its momentum from the photoionization to the recoil ion. Therefore, when plotting all spatial components of the electron momentum against the recoil momentum, all events are expected to be distributed along a straight line with a slope of -1. Figure 4.4 shows all three spatial momentum components of electrons and recoil ion after photoionization of helium with an energy of 9 eV and 13 eV above ionization threshold which equals a momentum of 8.1 au and 9.8 au, respectively. The events are distributed along the diagonal. Consequently, the detectors are rotated correctly.

4.3.5 Electric field and spectrometer geometry

For the momentum calculation different parameters, which describe the electric fields and the spectrometer geometry, are used as input. Table 4.4 shows the parameters of the electron side of the spectrometer and Table 4.5 the parameters of the ion side. Although in principle the values of these parameters are known, they still need to be verified by calibration measurements. It is important to note that the acceleration field, which corresponds to the parameter a_1 in the momentum calculation, is the same for ions and electrons. However, since the calculation of the electron and ion momenta is performed separately, as a result of the calibration the parameter a_1 might vary slightly for the electron side and the ion side of the spectrometer.

Ion side

Before the actual measurement with $NH_3 \cdots NH_3$ and $NH_3 \cdots H_2O$, calibration measurements with the noble gas nitrogen N_2 as a target were carried out. The reaction described by

$$N_2 + \gamma\,(54\,\mathrm{eV}) \longrightarrow N^+ + N^+ + 2e^- \tag{4.30}$$

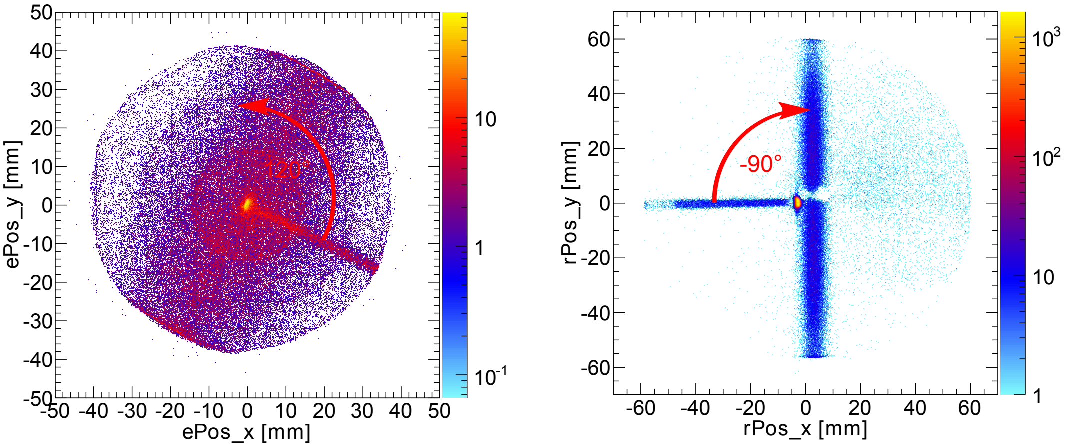

(a) Detector orientation before correction.

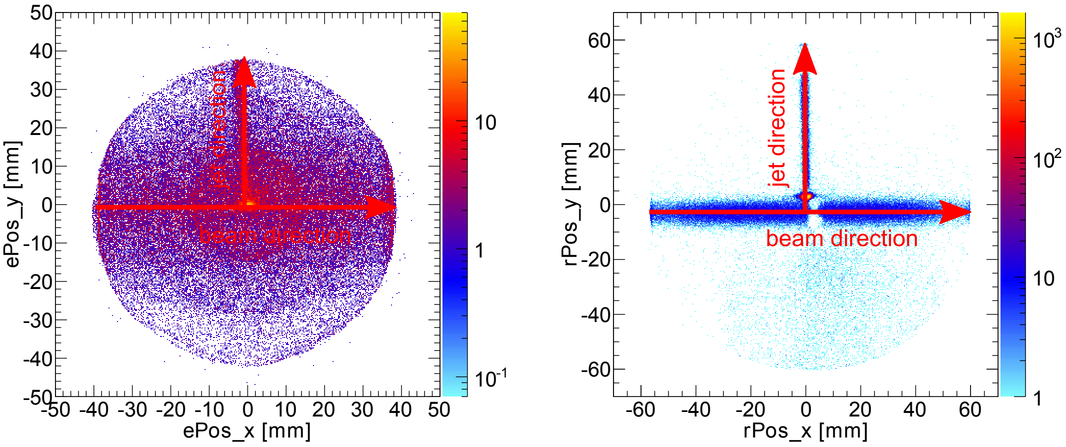

(b) Detector orientation after correction.

Figure 4.3: **(a)** During the experiment the layers are randomly connected to the electronics leading to a rotated position reconstruction. The hot gas stripe and the jet trace indicate their actual orientation in the coordinate system. The interruption of the hot gas stripe on the ion detector is caused by the blind spot where the detector efficiency reaches a minimum. **(b)** Both detectors are rotated so that the beam is aligned with the x-axis and the jet with the y-axis.

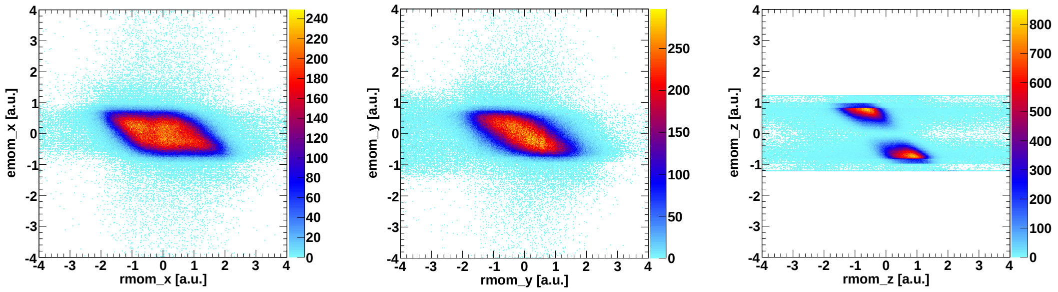

Figure 4.4: Due to momentum conservation electron momentum and ion momentum after photoionization must be equal but with opposite direction. Hence, plotting each of their spatial components against each other shows a distribution along a straight line with slope -1, if the detectors are correctly orientated.

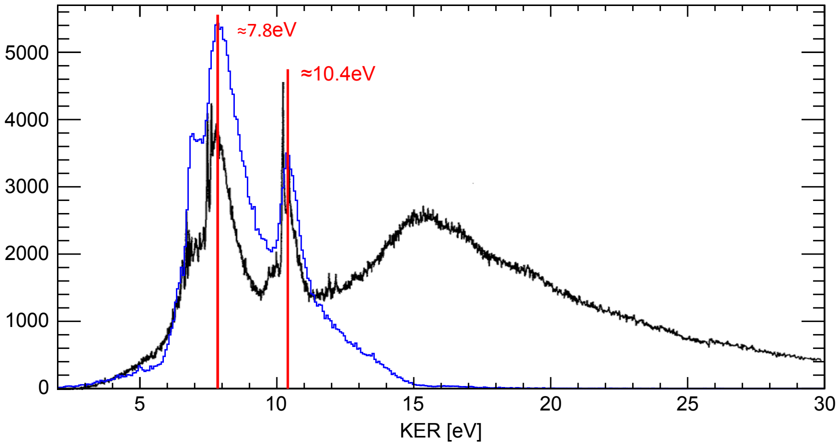

Figure 4.5: Calibration of the ion side of the spectrometer based on the the comparison of the measured KER spectrum of N_2 (blue) with the results from Lundqvist et al. [72] (black).

was measured. After being doubly ionized by a photon with 54 eV the N_2 molecules in the jet subsequently dissociate. Both recoil ions and one the electron from the reaction are detected in coincidence. The kinetic energy release

$$\text{KER} = \frac{|\vec{p}_{\text{rel}}|^2}{2 \cdot \mu} \tag{4.31}$$

is calculated from the relative momentum of the ions

$$\vec{p}_{\text{rel}} = \frac{\vec{p}_2 - \vec{p}_1}{2} \tag{4.32}$$

and the relative mass μ which is given by

$$\mu = \frac{m_{r_1} \cdot m_{r_2}}{m_{r_1} + m_{r_2}} \, . \tag{4.33}$$

Figure 4.5 shows the KER spectrum of N_2 compared with the results of Lundqvist et al. [72]. The length of acceleration and boost region as well as the corresponding electric field used in the momentum calculations are adjusted so that both major peaks in the spectra lie on top of

Table 4.8: Comparison of the two major peaks in the measured KER spectrum of N_2 with the results from Lundqvist et al. [72].

State	**Literature**	**Calibration**
$D^3\Pi_g \rightarrow N^+(^3P) + N^+(^3P)$	7.58 eV to 7.72 eV	7.8 eV
$D^3\Sigma_u^+ \rightarrow N^+(^3P) + N^+(^1D)$	10.08 eV to 10.77 eV	10.4 eV

each other. Beside a better resolution, the reference spectrum also features a different shape. This is due to the fact that Lundqvist et al. used electrons with an energy of 200 eV as projectile to induce the reaction. The KERs, that served as a reference for the calibration, are listed in Table 4.8.

Electron side

After calibrating the ion side of the spectrometer, the same procedure is done for the electron side. Therefor the kinetic energy of photoelectrons stemming from single ionized helium atoms is measured. If a helium atom is single ionized according to equation

$$\mathrm{He} + \gamma \longrightarrow \mathrm{He}^+ + \mathrm{e}^-_{\mathrm{photo}} , \tag{4.34}$$

momentum conservation must be fulfilled so that $|\vec{p}_e| = |\vec{p}_r|$. From the momentum conservation the relation between the kinetic energy of the recoil ion and of the electron

$$\frac{E_r}{E_e} = \frac{m_e}{m_r} \tag{4.35}$$

can be derived. Since the mass of the recoil ion is much larger compared to that of the electron ($m_r \approx 7350 \cdot m_e$), its energy is accordingly small and can be neglected in the energy balance of the reaction. Calculated with Equation 2.62, the kinetic energy of the photoelectron is then a good measure for the calibration if the photon energy and the ionization potential is known with high precision. The single ionization potential of helium is 24.6 eV and the photon energies 33.6 eV and 37.6 eV were chosen at the undulator. The geometry and field parameters used in the momentum calculation are adjusted in the data analysis so that the electron energies match the expected energies calculated using the literature values from [73]. Table 4.9 shows the comparison between the measured values and values taken from literature.

Table 4.9: Comparison of the measured energies of the photoelectrons with the energy values taken from literature [73].

Photon energy	**Literature**	**Calibration**
33.6 eV	9.013 eV	9.082 eV
37.6 eV	13.013 eV	12.90 eV

In addition to the energy values, also the momentum distribution has to be considered. The angular distribution of photoelectrons, that are emitted from the 1*s* orbital by linearly polarized light, is described by the beta parameter in Equation 2.71. In the case of helium, $\beta = 2$. For a given energy of the photoelectron, the absolute value of the momentum vector $|\vec{p}_e|$ has to be independent of its direction. Hence, the momenta of the electrons must be distributed on a

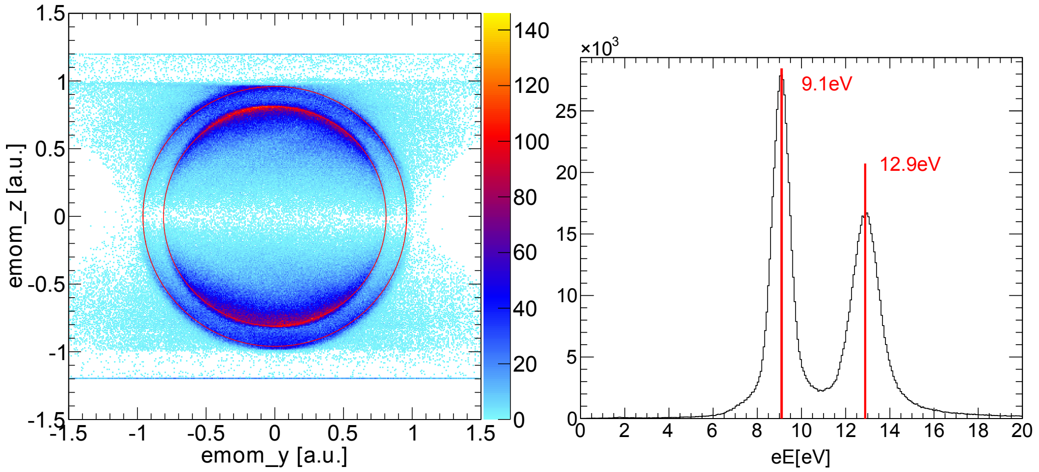

(a) Projection of the momentum sphere into the y-z plane **(b)** Energy spectrum of photoelectron

Figure 4.6: Electron momenta and energies after calibration of the electron side of the spectrometer. **(a)** In momentum space all electron momenta lie on a sphere. Its two-dimensional projections, e.g. in the yz-plane, are concentric circles with a preferred direction along the polarization axis z ($\beta = 2$). **(b)** The energy spectrum of the photoelectrons show two peaks at the expected energies 9 eV and 13 eV.

sphere. Its projection, e.g. into the yz-plane as seen on the left-hand side in Figure 4.6a, is a concentric circle. As seen in Figure 4.6b the round shape of the circle or sphere, respectively, corresponds to the accuracy of the calibration.

4.4 Correction of field inhomogeneities

The results of the calibration presented in Section 4.3.5 were obtained with the optimal set of parameters. However, the optimal calibration included an additional correction of the electric field. As mentioned above the momenta of the photoelectrons ideally lie on a sphere, which means that the absolute value of the momentum vector does not depend on its direction. Hence, plotting their kinetic energy against the azimuthal angle ϕ or the polar angle θ must show a flat distribution. However, in ToF-direction, this distribution could not be obtained by adjusting all input parameters. As seen in Figure 4.12a the kinetic energy of electrons, which started towards the ion detector ($cos\theta > 1$), is increased. This deformation arises from the fact that the measured ToF is longer than the theoretically expected one. Assuming a uniform acceleration field of 5.327 $\mathrm{V\,cm^{-1}}$ throughout the whole region, the longer ToF is calculated into momenta and energies with too high values.

The extended time-of-flight of the electrons starting towards the ion detector is due to a decrease of the electric field in the region of the ion mesh. Simulations[2] of the electric field along the spectrometer axis, i.e. $x, y = 0$, with different geometries and settings revealed two possible reasons for the field inhomogeneity:

1. Mounting the ion mesh on the right-hand side of the holder increases the distance to the last copper plate by 4 mm. Given the potential gradient caused by the resistance of $R = 600\,\mathrm{k\Omega}$, the increased distance leads to a lower electric field.

---

[2] The simulations were made with the program SIMION. Further information to SIMION can be found on `http://simion.com/`

2. Wrong adjustments of the potentiometer resistance between the last copper plate and the mesh holder cause a decrease of the potential and the electric field, respectively.

Figure 4.7 shows the simulated electric field in the acceleration region with the ion mesh on the left- and the right-hand side of the holder. The resistance between the copper plate and the holder is 600 kΩ. With the mesh on the right-hand side, the region is 103 mm long and the resulting field ~5.534 $\mathrm{V\,cm^{-1}}$. Except for the slight decrease towards the ion mesh, which is due to the geometry in the xy-plane (finite dimension and edges of the copper plates), the electric field is uniform. If the mesh is mounted on the right-hand side, the length is 107 mm and the acceleration field ~5.327 $\mathrm{V\,cm^{-1}}$. However, in this case the potentials of the copper plates are not distributed linearly anymore. At the electron mesh the field is too high and decreases towards the ion mesh below the expected average. This effect is very sensitive to the resistance between ion mesh holder and last copper plate as seen in Figure 4.8. According to the simulations a resistance of ~1200 kΩ is needed to compensate the effect of the extended distance between mesh and copper plate. Furthermore the simulations show that the decrease of the field is enhanced the lower the value of resistance of the potentiometer.

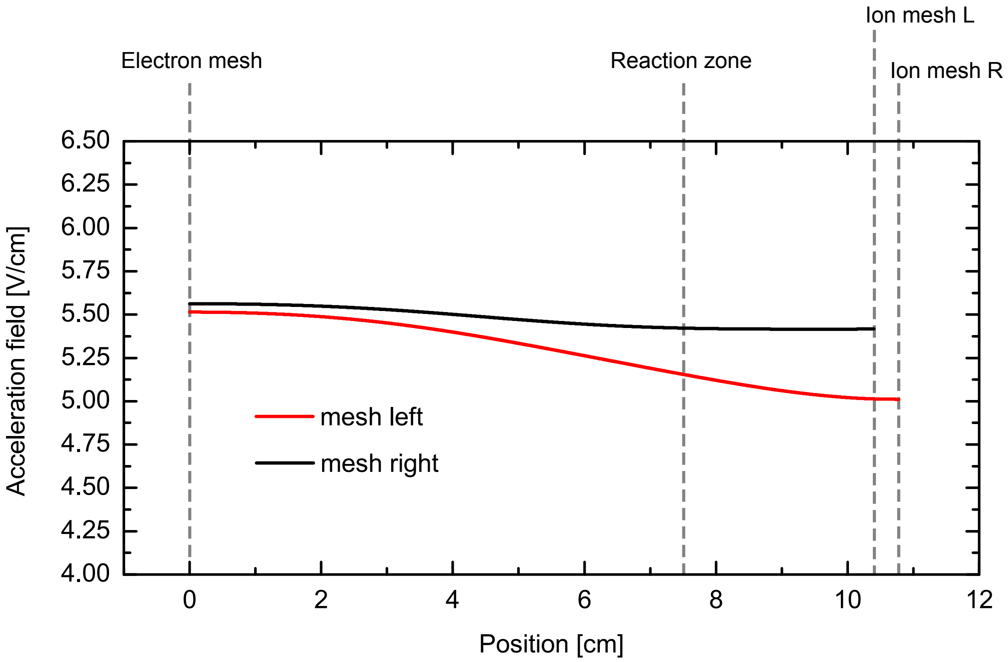

Figure 4.7: The electric field E in the acceleration region along the central line for different positions of the ion mesh. The last copper plate and the mesh is connected by a 600 kΩ resistance. If the ion mesh is mounted on the left-hand side of the holder, the field is almost uniform. However, if the mesh sits on the right-hand side, the field significantly decreases on this side.

In order to account for the inhomogeneity of the field, the calculations of the momentum z-component has to be adjusted. In an electric field, that is inhomogeneous along the z-axis, the acceleration a depends on the position z. Therefore, in order to calculate the ToF of an electron using equation 4.18 the acceleration function has to be integrated over z. However, this integration means significantly higher computational costs so that the momentum calculation using Newton's method (see Section 4.2.1) was not practicable. Instead, a simple look-up table was used. For a given momentum range, for instance $p_z = [-1.2\text{ au}, +1.2\text{ au}]$, the according ToFs were calculated and stored in an array. The measured ToFs were then assigned to the matching momenta via the look-up table. As an approximation of the real electric field, a discontinuous linear function, shown in Figure 4.9, was used. Figure 4.10 shows how the measured ToFs is

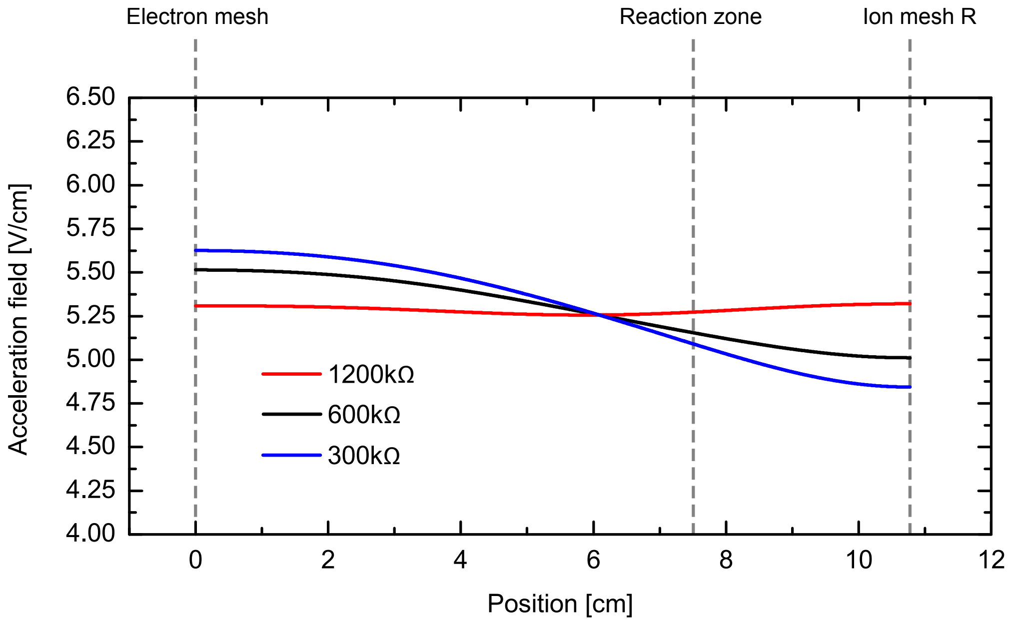

Figure 4.8: The electric field E in the acceleration region for different resistances of the potentiometer connecting the last copper plate and the ion mesh. The simulation shows that the lower the resistance of the potentiometer, the more the field is distorted. In order to compensate the effect of the extended distance between the copper plate and mesh the potentiometer should have a resistance of~1200 kΩ.

calculated to the z-component of the momentum assuming a homogeneous acceleration field. The resulting momentum distribution in the upper part of Figure 4.10 is not symmetric around zero as it should be. The approximation function used for the look-up table gives the correct momentum distribution as seen in Figure 4.11. As a result of the field correction, the calculated energy of the electrons does not depend on the initial flight direction of the electrons. Figure 4.12 shows the energy of the photoelectrons plotted against the cosine of the polar angle before and after considering the field inhomogeneity in the calculations.

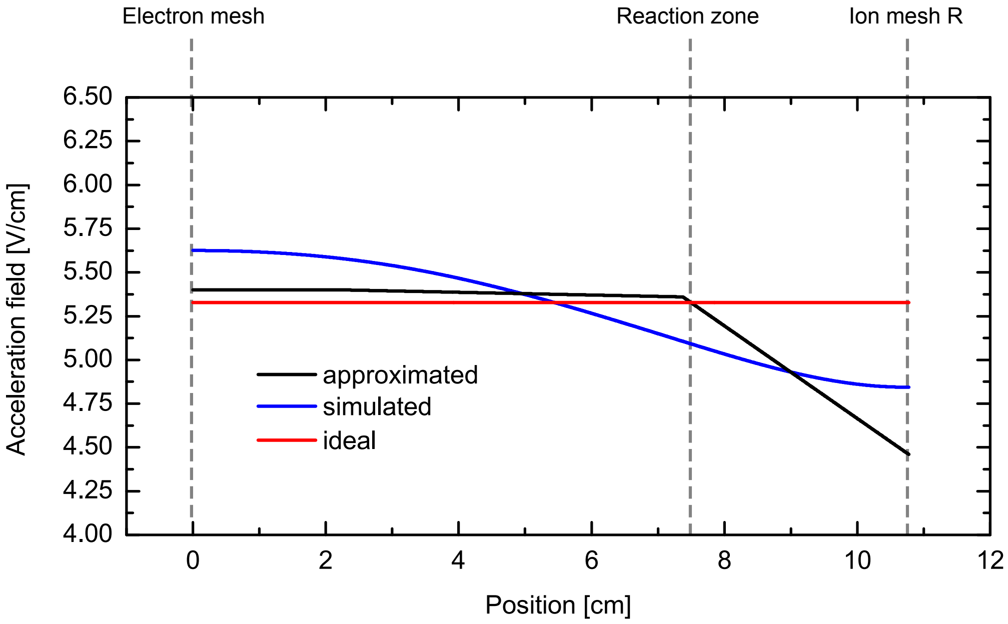

Figure 4.9: For the momentum calculations a discontinuous linear function was used as an approximation of the inhomogeneous field. In order to save computational costs the function was chosen to be as simple as possible.

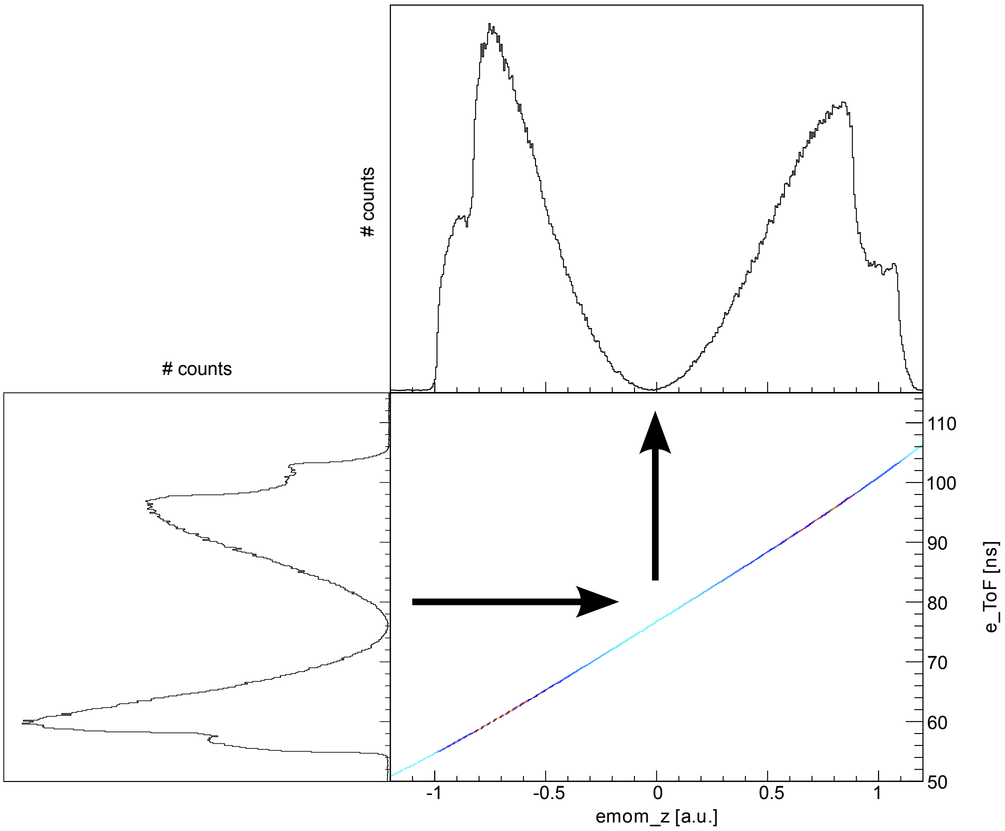

Figure 4.10: The measured ToF distribution is distorted by the field inhomogeneity (left part). Electrons initially moving towards the ion detector need more time until they hit the electron MCP than expected for a homogeneous acceleration field. Under the assumption of a uniform electric field the calculated momentum distribution appears asymmetric (upper part).

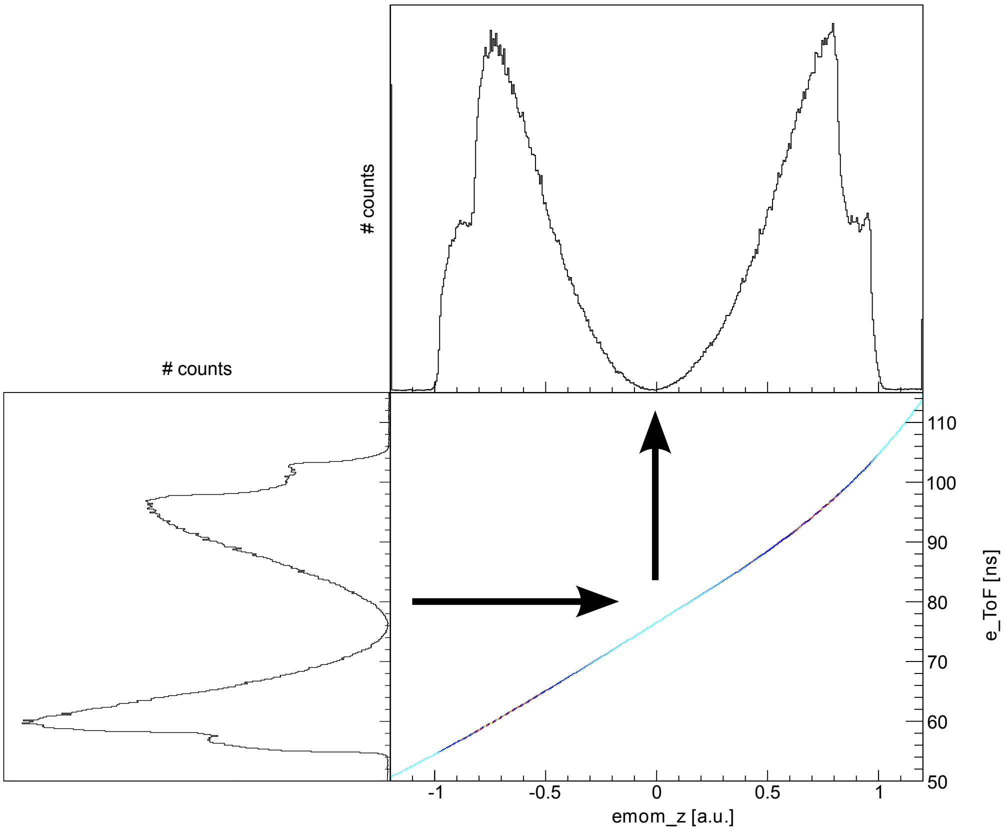

Figure 4.11: After accounting for the field inhomogeneity the measured ToF distribution (left part) is calculated to a momentum distribution which is symmetric around zero (upper part).

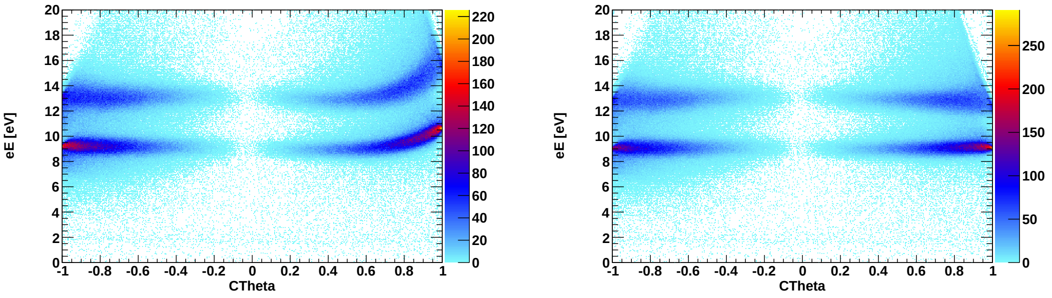

(a) Before correction

(b) After correction

Figure 4.12: **(a)** Before the field correction all electrons initially starting towards the ion detector ($cos\theta > 0$) are assigned to too high energies. **(b)** Taking the field inhomogeneity into consideration all electrons have the same energy independent of their starting direction.

4.5 Presorting and channel identification

Beside the molecules $NH_3 \cdots NH_3$ and $NH_3 \cdots H_2O$, the jet mainly contains the single molecules NH_3 and H_2O. In addition, there are background particles due to the non ideal vacuum that are able to react with the photons. Therefore, it is likely that the coincidence condition from Section 3.2.4 is fulfilled although the detected particles assigned to an event have not been created in the same reaction. During the measurement a huge amount of data was recorded containing approximately 5×10^9 events. In order to efficiently analyze the reactions of interest, the data is reduced as a first step. By setting specific conditions on the time-of-flight of the coincidently detected ions most of the false events can be rejected (see Section 4.5.1). Since the target molecules might undergo different breakups creating various fragments, the potential breakup channels have to be identified in the remaining data. By requiring momentum and energy conservation the channels can be separated from each other (see Section 4.15). The identified channels are then further processed by analyzing the kinematics of the particles created in the corresponding breakups.

4.5.1 Presorting

When presorting the data only the ToFs of the particles are considered. The main condition is set on the ion ToFs as it can be seen in the photoion-photoion-coincidence (PIPICO) spectrum illustrated in Fig 4.13. Given the time-of-flight of the first detected recoil ion $\mathrm{ToF}_{\mathrm{r1}}$, the time-of-flight of the second ion $\mathrm{ToF}_{\mathrm{r2,clalc.}}(\mathrm{ToF}_{\mathrm{r1}}, m_1, m_2)$ is calculated under the assumption of a back-to-back Coulomb explosion using the measured time-of-flight of the first ion and the masses of the particles. Setting the condition

$$[\mathrm{ToF}_{\mathrm{r1,measured}} - \mathrm{ToF}_{\mathrm{r2,clalc.}}] < \Delta\mathrm{ToF} \quad \vee \quad [\mathrm{ToF}_{\mathrm{r2,measured}} - \mathrm{ToF}_{\mathrm{r1,calc.}}] < \Delta\mathrm{ToF} \tag{4.36}$$

with a defined time width $\Delta\mathrm{ToF}$ most of the false events can be rejected while still keeping the relevant events. For the presorting the masses $m_1 = m_2 = 17$ and a time width of $\Delta\mathrm{ToF} = 600\,\mathrm{ns}$ were used. In addition, a condition was set on the electrons. By only allowing events with electrons which have a ToF in range of $\Delta\mathrm{ToF}_{\mathrm{e}} = 80 \pm 50\,\mathrm{ns}$ the data is reduced in total by a factor of ~30.

4.5.2 Mass sorting

As seen in Figure 4.14, the potential breakup channels (i.e. fragments with different masses) lie very close to each other in the PIPICO spectrum. In order to separate channels, that lie next to each other, all events are checked for momentum conservation with different mass combinations. For example when separating channel 17/17 and 17/18, an event belongs to channel 17/17, if

$$|\vec{p}_{\mathrm{r1}}(m_1 = 17) + \vec{p}_{\mathrm{r2}}(m_2 = 17)| \; < \; |\vec{p}\,'_{\mathrm{r1}}(m_1 = 17) + \vec{p}\,'_{\mathrm{r2}}(m_2 = 18)| \tag{4.37}$$

and to channel 17/18, if

$$|\vec{p}_{\mathrm{r1}}(m_1 = 17) + \vec{p}_{\mathrm{r2}}(m_2 = 17)| \; > \; |\vec{p}\,'_{\mathrm{r1}}(m_1 = 17) + \vec{p}\,'_{\mathrm{r2}}(m_2 = 18)|. \tag{4.38}$$

Figure 4.15 shows how the events in the PIPICO are separated by this procedure for the channels 17/17 and 17/18, respectively.

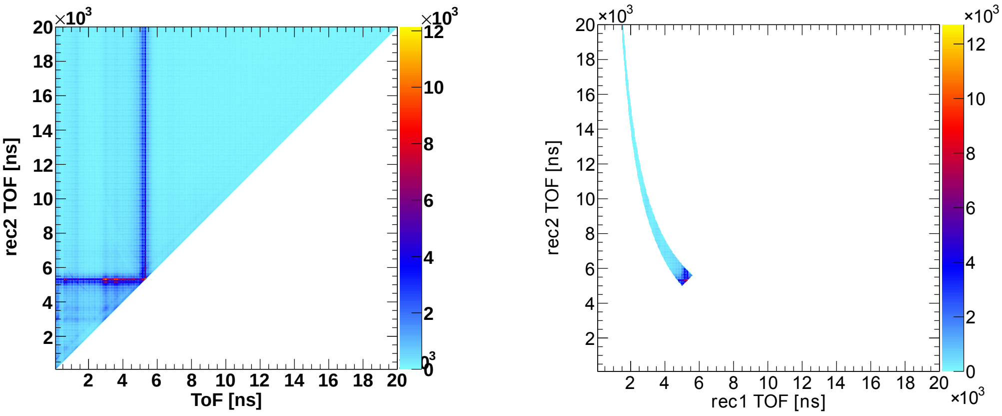

(a) PIPICO raw

(b) PIPICO presorted

Figure 4.13: **(a)** The raw PIPICO spectrum contains all events with two ions that were detected in coincidence. In principle the ions cannot be distinguished. Hence, they are labeled *ion 1* and *ion 2* depending on the order they stroke the detector. The diagonal represents all events where both ions had the same ToF. **(b)** After the data has been presorted only events, that fulfill the conditions set on the ToFs of the ions, remain.

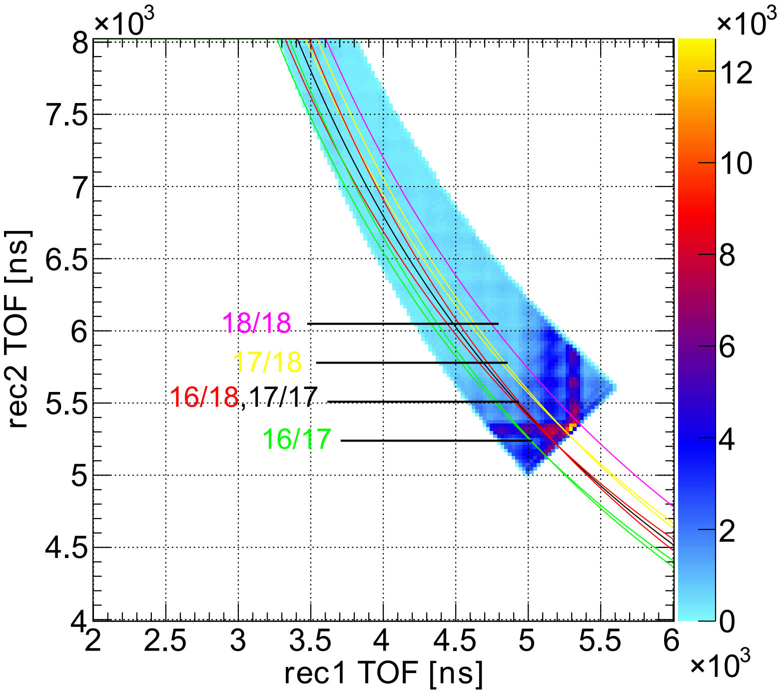

Figure 4.14: The potential breakup channels lie very close to each other in the PIPICO. Thus, they need to be separated for further analysis.

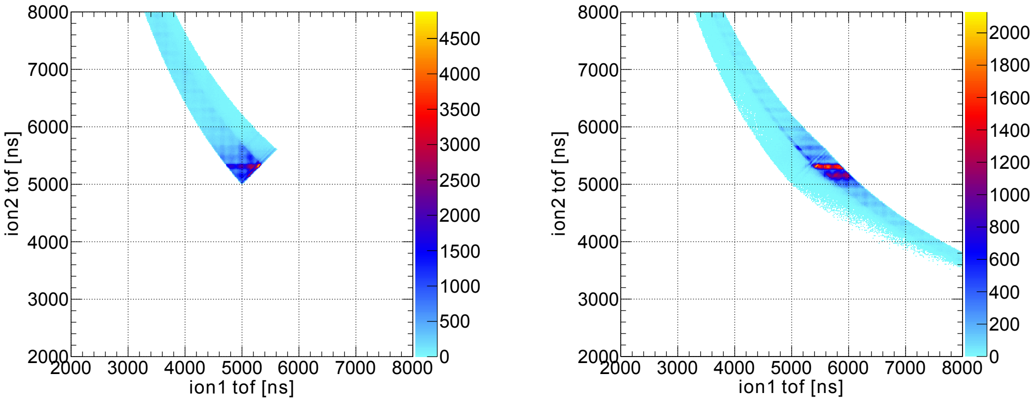

(a) Events assigned to channel 17/17.

(b) Events assigned to channel 17/18.

Figure 4.15: Breakup channels in the PIPICO are separated by comparing the fulfillment of momentum conservation using the corresponding mass combinations. To further reduce the data events with $|\vec{p}_{\mathrm{r}1} + \vec{p}_{\mathrm{r}2}| > 10\sqrt{3}$ au are generally rejected. **(a)** Events, where momentum is better conserved with the masses $m_1 = 17$ au and $m_2 = 17$ au, are assigned to the channel 17/17. **(b)** If momentum conservation is better fulfilled with $m_1 = 17$ au and $m_2 = 18$ au, the event belongs to breakup channel 17/18.

4.5.3 Momentum conservation

For every reaction the total momentum must be conserved. Thus the momenta of all fragments should component-wise add up to zero. Since the electron momenta are considerably smaller than the ion momenta, momentum conservation of the ions is considered without the electrons.

Two ions, that were produced in a back-to-back Coulomb explosion, have opposite momenta with the same absolute value. Therefore, the events of a breakup channel are filtered out by setting the condition

$$\frac{(p_{\mathrm{r}1,\mathrm{x}} + p_{\mathrm{r}2,\mathrm{x}})^2}{a^2} + \frac{(p_{\mathrm{r}1,\mathrm{y}} + p_{\mathrm{r}2,\mathrm{y}})^2}{b^2} + \frac{(p_{\mathrm{r}1,\mathrm{z}} + p_{\mathrm{r}2,\mathrm{z}})^2}{c^2} < 1, \tag{4.39}$$

which requires that the sum of each momentum component should be smaller than a given value a,b and c. Figure 4.16 shows the momentum components of one ion plotted against the components of the other ion, which are, as expected, distributed along a line with slope -1.

Figure 4.16 also shows that the momentum components have different resolutions. The resolution in x-direction is limited by the diameter of the gas jet and therefore the lowest of all components. The y-direction is limited by the focus of the light beam. Because the spatial components x and y solely depend on the position measurement, which technically has a lower resolution than the time measurement, they generally have a lower resolution than the z-component. The latter is measured with the highest precision.

With the spectrometer configuration, that was used in the experiment, only electrons with a momentum smaller than ~1 au can be detected while covering the full solid angle. In order to further discriminate against background events the momentum components of each electron was limited by $p_i < 0.95$ au.

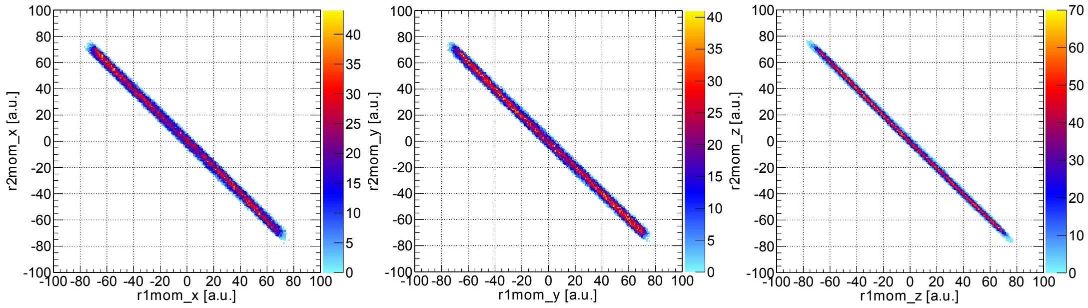

Figure 4.16: The spatial components of the momentum of recoil 1 vs. that of recoil 2. Due to momentum conservation all events lie on a diagonal with slope -1.

4.5.4 Re-calibration

The spectrometer was calibrated using data obtained from measurements in which helium was photoionized and nitrogen molecules doubly ionized with a subsequent dissociation. Therefore, the input parameters of the spectrometer geometry, as well as of electric and magnetic fields were adjusted so that the measured electron energies and KERs match with the values taken from literature (see Sections 4.3.5).

However, the experimental conditions might not have been stable throughout the 14 days of measurements. For example, due to temperature changes the focus of the photon beam could have slightly shifted misaligning the position of the reaction zone relatively to the detectors. As a result the physical center would not have corresponded to the center of reconstructed spatial coordinates and the momentum calculation would then become inaccurate.

Using one of the identified breakup channels, the ion side of the experimental setup can be re-calibrated. The detector position is shifted so that the calculated ion momenta have again a spherical distribution. Then each projection of the ion momenta is circular and centered around zero. The same holds for the relative momenta $p_{\mathrm{rel}} = |\vec{p}_{\mathrm{r2}} - \vec{p}_{\mathrm{r1}}|$ as it is shown in Figure 4.17. Another method of checking for the correctness of the momentum calculation is to observe the plot of the kinetic energy release as a function of the azimuth angle ϕ and the polar angle θ. A spherical momentum distribution of both ions is equivalent to a KER that is independent of the direction. Hence, the KER appears flat as it can be seen in Figure 4.18.

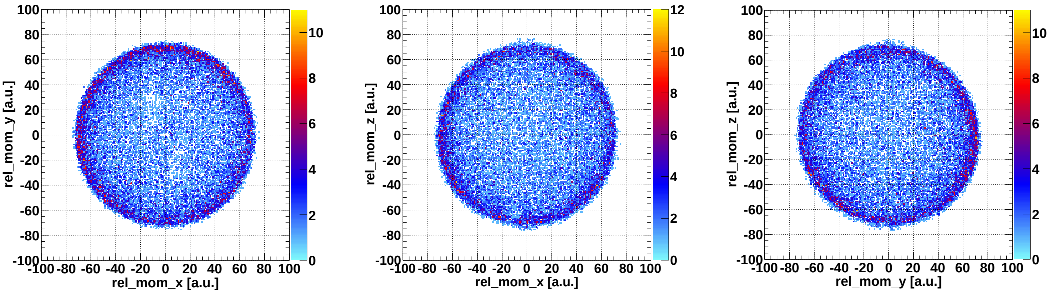

Figure 4.17: Relative momenta of the 17/18 breakup. The momentum calculation is correct, if all relative ion momenta $p_{\mathrm{rel}} = |\vec{p}_{\mathrm{r2}} - \vec{p}_{\mathrm{r1}}|$ lie on a three-dimensional sphere. Its projection into the planes spanned by the Cartesian axes must appear circular. The radius of the sphere is determined by the KER.

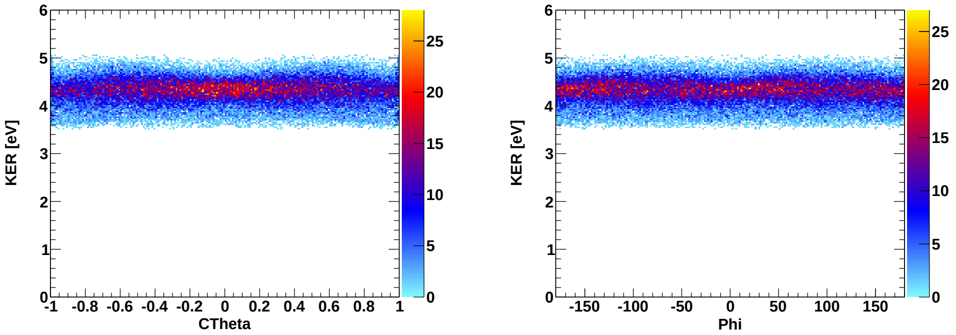

Figure 4.18: The kinetic energy release of the 17/18 breakup. With the KER as a function of the azimuth and polar angle, the spherical distribution of the relative ion momenta can be checked.

4.5.5 Restriction to full coincidences

As explained in Section 3.2.4, the minimum condition for an event to be recorded is the coincidence of one electron and two ions. Although the removal of at least two electrons is precedent to every Coulomb explosion, the probability detecting all four fragments in coincidence is very low. This is due to the limited detector efficiency as well as the dead time (see Section 4.6). Hence, most of the events found in the breakup channel contain only one electron hit as seen in Figure 4.19. For a reasonable investigation of the ICD and the double ionization, the energy and momentum of all fragments must be considered. Therefore only events with more than one electron hit are considered. Thus, the number of useful events is reduced by approximately 66%.

Some of the events remaining in the data set contain three or even four electron hits. The additional electrons either come from false reconstructions or belong to a different reaction. In order to correctly choose the two electrons belonging to the reaction of interest each combination of electron pair is tested together with both ions for momentum conservation.

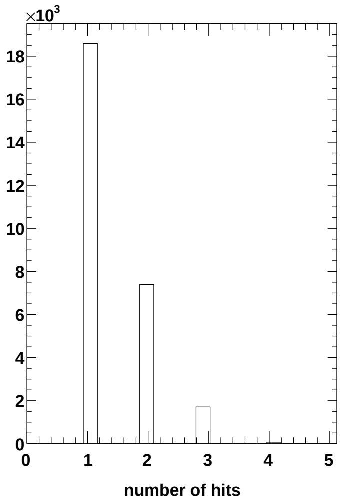

Figure 4.19: Electron hits in channel 17/18. The coincident detection of more than one electron together with two ion is much less likely.

4.6 Errors and limitations

In order to accurately interpret the results of the COLTRIMS measurement, a good understanding of the uncertainty of the experimental setup and the expected errors is crucial. Generally, there are two ways to estimate the uncertainty of a single measurement. Either the propagation of the uncertainty is derived based on the error and resolution of each component of the experimental setup, or the resulting broadening of the measured variable is evaluated around its true value in the obtained spectra. Considering the complexity of the experiment as a whole, the latter option turns out to be more reliable. Assuming that all detected events are independent from each other and occur under unchanged conditions, i.e. the probability distributions of the variables do not change, the distribution of a variable, for example the electron momentum, converges for large numbers to the Gaussian distribution according to the central limit theorem. The full width half maximum (FWHM) can then be interpreted as the statistical error which accounts for all uncertainties stemming from the experimental setup. Its relation to the standard deviation of a Gauss distribution σ is given by

$$\mathrm{FWHM} = 2\sqrt{2\log 2}\sigma \; . \tag{4.40}$$

I addition, the broadening of a distribution needs to be considered. The broadening is partly due to the finite lifetime of the decaying state in which the detected particle is created. If the resolution of the measurement is not sufficient, the substructure of the states due to vibration and rotation also has to be considered as uncertainty.

The primarily measured variable of a COLTRIMS experiments is the momentum p of the electrons and ions. To estimate the momentum error for the electrons the calibration measurement with helium is used. As seen in Figure4.20, the momentum distributions of the electrons tend to become broader for higher values. This is due to non-linear effects related to how the finite reaction volume is projected on the detector.

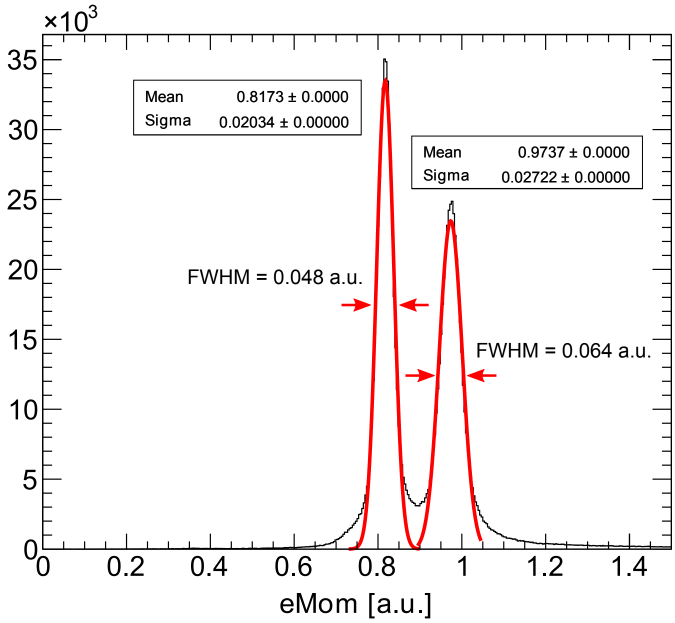

Figure 4.20: For a large number of counts the momenta are Gaussian distributed and the FWHM is used as an estimation of the measurement errors. To estimate the error of the electron momentum the results from the calibration measurement with helium is used.

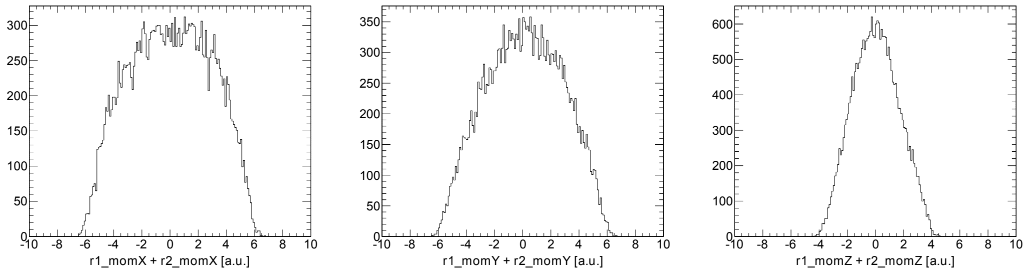

Figure 4.21: The sum of the ion momenta for each component are centered around zero due to momentum conservation. The ion pairs stem from a 17/17 breakup.

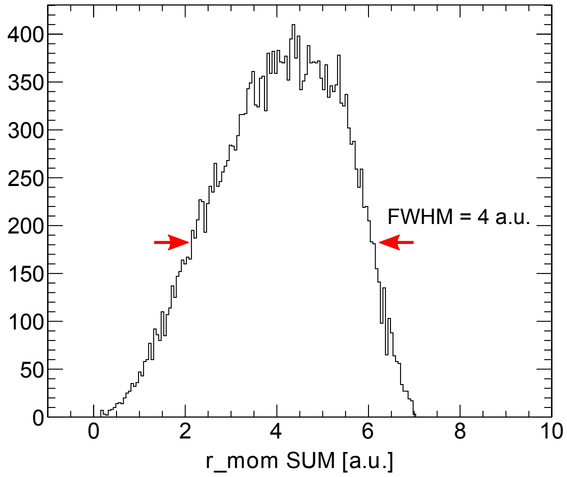

Figure 4.22: The sum of the total momentum of ion pairs stemming from a 17/17 break up is distributed around a value greater than zero since the total momentum sum cannot be negative. Despite a non-Gaussian distribution, the FWHM is used as an error estimation.

Table 4.10: Estimated momentum and energy errors for electron and ions based on the FWHM.

	Momentum	**Energy**
Electron	~0.03 au	~0.8 eV
Ion	~2.0 au	~0.2 eV

The energy values are derived from the momenta using the formula

$$E = \frac{p^2}{2m} \; . \tag{4.41}$$

Their errors can then either be calculated as propagation of the momentum errors according to

$$\Delta E = \sqrt{\left(\frac{\partial\left(p^2/2m\right)}{\partial p}\Delta p\right)^2 + \left(\frac{\partial\left(p^2/2m\right)}{\partial m}\Delta m\right)^2} \approx |\frac{p}{m}\Delta p| \tag{4.42}$$

or estimated from the spectra. Equation 4.42 shows that the relation between the error of the momentum and of the energy is linear. Hence, the absolute error of the energy increases with its value. Derived from the momentum spectra, the resolution for electrons at high energies is ~0.8 eV, yet for lower energies the error is smaller.

The error of the measured ion momentum cannot be estimated as precise as the electron momentum. The detected ions gain their momentum or kinetic energy, respectively, from the Coulomb explosion which varies with the nuclear distance at the instance of the explosion. However, the sum of the momenta of an ion pair is supposed to be zero due to momentum conservation. Hence, the width its distribution gives a rough indication of how large the error of the ion momenta is. Figure 4.21 shows the sum of each momentum component of the ion pair from the 17/17 breakup, which is discussed in Section 5.3. The sum of the total momentum is distributed around a value greater than zero as seen in Figure 4.22. Although the distribution is not Gaussian shaped, a FWHM of ~2 au can be assumed which calculates to an energy error of ~0.2 eV. All estimated errors are listed in Table 4.10.

As stated above, there are multiple sources of errors in the experiment that lead to the uncertainties of the variables. These potential sources are briefly discussed.

Inaccurate calibration As mentioned in Section 4.3, the experimental setup is calibrated by adjusting the set of relevant parameters so that the measured results match with the literature values. Although this was done with highest rigor, its precision is still limited due to limitations in the determination of certain parameters such as the shift of the ToF or the gyration period. In addition disturbing effects, e.g. the $\vec{E} \times \vec{B}$−drift or field inhomogeneities, can only partly be corrected.

Time resolution The detectors have a time resolution of less than 0.2 ns [65]. In addition to the technical limitation of the time measurement the starting point of the particles is slightly delocalized due to the finite reaction volume. On the electron side this issue is addressed by the time-focusing geometry and on the ion side by calculating with relative coordinates.

Position resolution The spatial resolution of the MCPs is given by the diameter of its tubes which is ~25 µm. Together with the delay line anodes, which are necessary for the localization of where the particle hit the MCP, the system has a resolution of less than 0.1 mm in each direction [65]. Beside the technical limitation, the resolution also varies with the size of the area that is used on the detector. The electric fields of the spectrometer are adjusted so that the particles with the expected energies fill most of the area available for detection. This ensures that the momenta are optimally resolved.

Dead time Both, the MCPs and the delay line anodes have a dead time. After an electron cloud has left the MCP, the potential between the front and back of the MCP has to be built up again. In the meantime no particle can be detected. The electron leaving the MCP creates an electronic signal in the wires of the anode. This signal moves with finite speed towards the end of the wires where it is acquired by the electronics. If two electron clouds leave the MCP in very quick succession, the created signals in one wire have an overlap and therefore might be indistinguishable. Hence, the second particle cannot be detected. Figure 4.23 shows that the dead time of the detector for example leads to a time window of $< 5\,\mathrm{ns}$ and relative distance of $< 3\,\mathrm{mm}$ within that two electrons cannot be detected.

Detector efficiency minimum The ion detector features a blind spot which is visible as an interruption of the hot gas stripe in Figure 4.3. Since the detected ionic fragments of the target molecules gain their momentum from a Coulomb explosion they are generally distributed over the whole active area of the detector. Hence, only a small part of the momentum sphere of the ions cannot be covered due to the blind spot.

Gas jet The target particles are prepared in a supersonic gas jet where they are supposed to have very little momentum, yet high enough to bias the momentum created in the reaction. In addition, the reaction volume defined by the overlap of the gas jet and the photon beam has a finite geometry. Hence, the starting point of the particles is delocalized resulting in a uncertainty in the momentum measurement. Figure 4.17 and 4.21 show that the precision of the momentum measurement varies depending on the spatial direction.

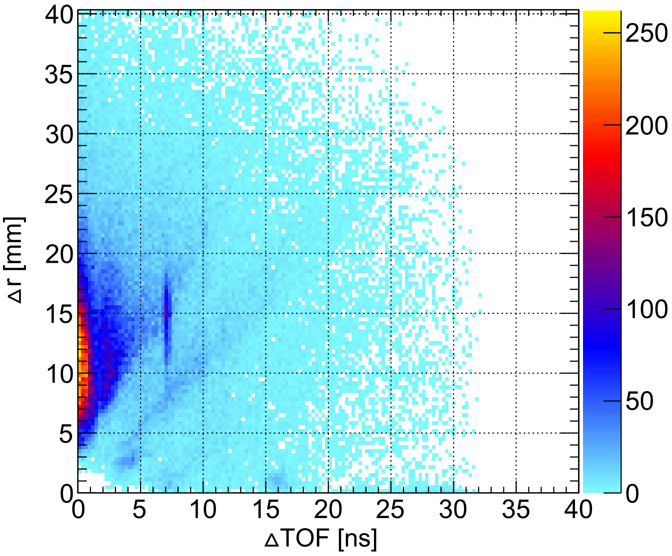

Figure 4.23: The relative ToF of both coincidently detected electrons versus their relative position. The white spot in the lower left corner of the diagram shows that due to the dead time of the detector electrons with a relative distance of $< 3\,\mathrm{mm}$ and a time sequence of $< 5\,\mathrm{ns}$ cannot be detected.

Chapter 5

Results and conclusions

In this thesis, the COLTRIMS method was used to investigate the ICD of the hydrogen bonded systems $NH_3 \cdots NH_3$ and $NH_3 \cdots H_2O$. As described in the preceding Chapter 4 the measured data was presorted and the background was reduced for all fragmentation channels that might have occurred. Beside the expected breakups 17/17, for $NH_3^+ + NH_3^+$, and 17/18, for $NH_3^+ + H_2O^+$, also the channel 18/18, likely for $H_2O^+ + H_2O^+$, was identified. However, it appeared with a comparably low rate. Other potential fragmentation channels, such as 16/17 and 16/18, were not found. The identified breakup channels are illustrated in Figure 5.1.

In the following chapter the results of the analysis are presented and discussed. For each fragmentation channel, the kinetic energy release is examined and the electron energy spectra, that contain important information about the decay process, are presented. In case a specific process can be identified, it is further explored by the inspection of the angular distribution of the electrons. The results are compared to either previous measurements or theoretical calculations. Furthermore, the possible effect of the chemical composition of the gas jet on the measured reactions is discussed. Finally, conclusions are drawn from the measured data.

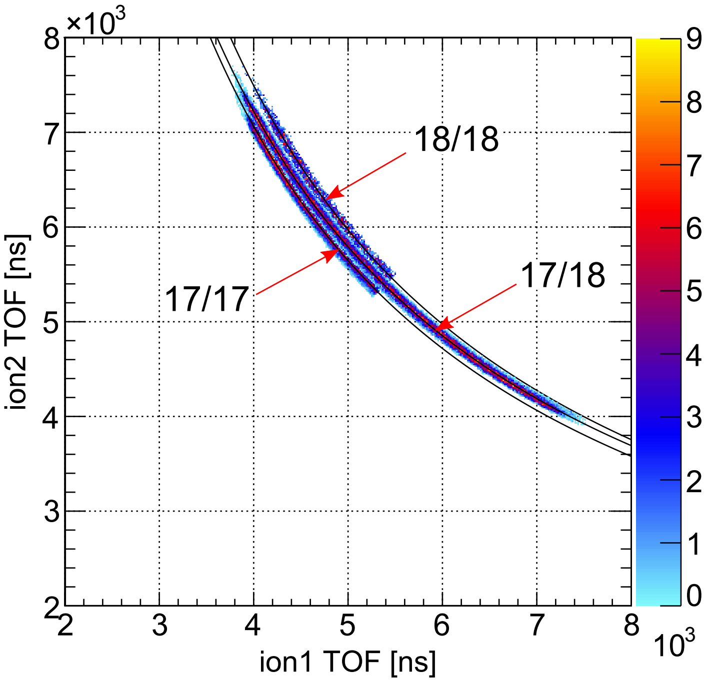

Figure 5.1: PIPICO spectrum of the identified breakup channels that are assigned to the ionic fragments with masses 17/17, 17/18 and 18/18. Due to the indistinguishability of the detected ions the symmetric breakups 17/17 and 18/18 form only half of a line. Containing ~90% less events than the other channels channel 18/18 is the weakest.

5.1 $H_2O^+ + H_2O^+$ breakup

Among the other molecular compositions, water dimers were likely candidates to be formed in the gas jet during the experiment. The data analysis showed the existence of a breakup into ionic fragments with masses each of 18 au corresponding to that of the water molecule. The breakup channel was, however, very weak as it only contains ~3000 events and ~1200 when requiring full coincidences. The kinetic energy release of this breakup shown in Figure 5.2 is found to be ~4.2 eV. This value corresponds to the results of a previous measurement performed by Jahnke et al. [30] who verified the existence of ICD in water dimers using synchrotron light.

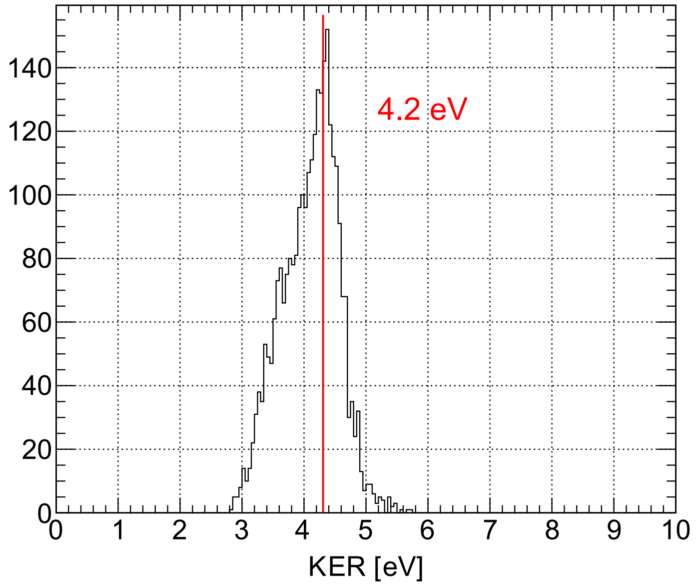

Figure 5.2: Measured kinetic energy release of both ionic fragments in channel 18/18.

Due to its complex electronic structure with various internal degrees of freedom, the water molecule has many single and double ionization potentials. According to the results of Stoychev, Kuleff, and Cederbaum, the single ionization potentials range from 30 eV to 36 eV for an equilibrium geometry of both O atoms having a distance of 2.1 Å or 2.91 Å, respectively. The lowest two-site double ionization potential[1] is at 28.3 eV [74]. Using photons with an energy of 43 eV, Jahnke et al. [30] recorded photoelectrons with energies between 4 eV and 13 eV which correspond very well to the theoretical results. In the same study by Jahnke et al., the ICD electrons were detected with an energy below 3.5 eV [30]. This is in line with the *ab initio* calculations by Stoychev, Kuleff, and Cederbaum [74] that suggest an energy distribution of the ICD electron mainly at low energies around 1 eV. Although the ICD electrons were most prominent at almost zero energy, also other combinations of photoelectrons and ICD electron occurred due to a manifold of orbitals involved in the decay process. However, the sum of the energy of both electrons remained below a threshold of ~14.5 eV determined by the double ionization potential and the photon energy.

---

[1] Two-site double ionization means that the electron holes are distributed on both molecules, whereas in a one-site double ionization the holes are created in only one molecule. In general the energetic threshold of a dicationic two-site state is lower than that of a one-site state.

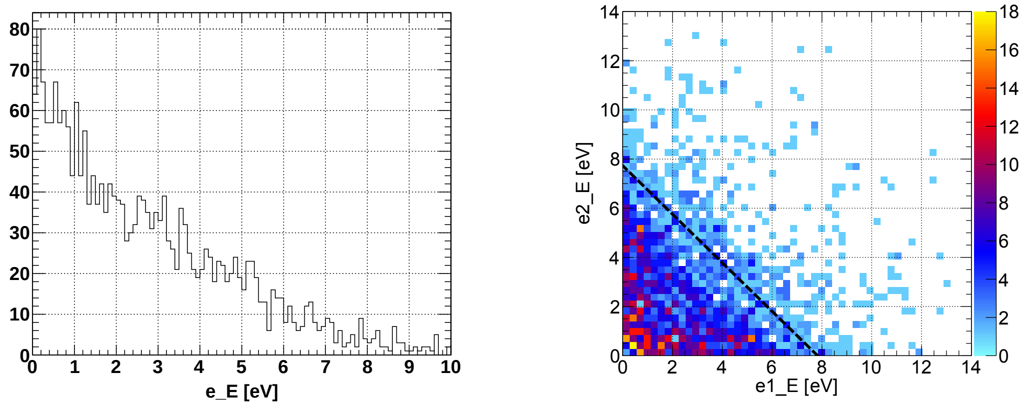

(a)

(b)

Figure 5.3: **(a)** Kinetic energy of both electrons stemming from the $H_2O^+ + H_2O^+$ breakup. The electrons have energies below ~8 eV. **(b)** Symmetrized spectrum showing the energy of electron 2 plotted against the energy of electron 1. The maximum sum of the energy of both electrons is 8 eV marked by the dashed diagonal.

In this experiment the used photon energy was 36 eV. Hence, given the lowest DIP of the water dimer at 28.3 eV, the sum of the energy of the photoelectron and ICD electron is capped at ~8 eV as seen in Figure 5.3a and 5.3b. As the inner-valence single ionization potentials of the O atoms lie in the range of 30 eV to 36 eV, electrons with an energy of 0 eV to 6 eV are likely to be photoelectrons. The energy of the ICD electron does not depend on the energy of the absorbed photon. Hence, similar to the results of Jahnke et al., they are predominantly attributed with energies below 1.5 eV. The majority of electron pairs stemming from ICD are presumed to lie in the more dense region of Figure 5.3b showing the kinetic energy of electron 2 plotted against the energy of electron 1. Unfortunately, it is not possible to distinctively distinguish the photoelectron from the ICD electron since their energy lie in the same range.

Electrons can also be created through double ionization. According to the work of Stoychev, Kuleff, and Cederbaum various double ionization thresholds lie below 36 eV [74]. For a Coulomb explosion to happen upon a one-site double ionization, the positive charge must be transferred to the partner monomer. Therefor the distance between the molecules must decrease which corresponds to a higher KER. Since an increased KER was not observed, one-site double ionization can be disregarded. The other mechanism leading to a Coulomb explosion is the two-site direct double ionization. However, this process is generally much more unlikely than ICD or one-site double ionization.

In conclusion, the breakup of water dimers is observed. Intermolecular Coulombic decay is presumed to be the responsible mechanism, yet no distinct evidence can be identified since photoelectron and ICD electron cannot be distinguished based on their kinetic energy.

5.2 $NH_3^+ + H_2O^+$ breakup

Beside the breakup channel of 18/18 discussed in the previous section, the breakup of molecules into ionic fragments of masses 17 au and 18 au could also be identified. Containing ~30,000 events and ~12,000 when requiring full coincidences, this channel is much stronger than the 18/18 fragmentation channel. There are different molecular clusters potentially existing in the gas jet that can break up into ionic fragments with masses 17 au and 18 au. Since the molecules NH_3 and H_2O where used to form the jet, the following three breakups need to be taken into consideration: $NH_3^+ + H_2O^+$, $NH_3^+ + NH_4^+$ and $OH^+ + H_2O^+$. The breakup $OH^+ + H_2O^+$ can be disregarded as the detected fragments stem from a three-body breakup and thus do not fulfill momentum conservation without the third particle. The breakup into $NH_3^+ + NH_4^+$ is also rather unlikely to be produced in the jet due to the necessary deprotonation that has to occur prior to the formation of the molecule. Even if it would exist in the jet, the chances for this molecule to break up are low. According to *ab initio* calculations by Stoychev, Kuleff, and Cederbaum [10], the core hole single ionization potential of nitrogen in $NH_3 \cdots NH_4$ lies below the lowest double ionization threshold meaning that ICD should be terminated. Moreover the energy of 36 eV is not sufficient to directly doubly ionize the system. The remaining possible candidate for a 17/18 breakup is $NH_3 \cdots H_2O$. Both molecules are abundant in the gas jet and according to theoretical calculation various double ionizing processes including ICD are energetically allowed [10].

5.2.1 Kinetic energy release

As mentioned in Section 2.3.2, both molecules, H_2O and NH_3, can function as proton donor or acceptor, respectively, when forming an intramolecular hydrogen bond. Depending on which molecule donates the proton, the geometry of the system varies leading to a different electronic and nuclear structure. According to numeric calculations by Stoychev, Kuleff, and Cederbaum, the KER of $NH_3 \cdots H_2O$ is 0.5 eV lower than that of $H_2O \cdots NH_3$ [10]. The KER of the ionic fragments of channel 17/18 is measured at 4.3 ± 0.2 eV as presented in Figure 5.4. Comparing this value with the calculated KER of $NH_3 \cdots H_2O$ and $H_2O \cdots NH_3$ as listed in Table 5.1, it can be concluded that NH_3 predominantly acts as the proton donor when forming a hydrogen bond in the gas jet.

The data shows a tail towards lower KER which might indicate a second weaker peak at around 3.9 eV. This structure might be created by ionic fragments with masses 17 au each stemming from a $NH_3^+ + NH_3^+$ breakup, which has a lower KER as presented in Section 5.3.1. Since the breakup channels lie very close to each other in the PIPICO spectrum as shown in Figure 4.14, it is possible that these ions form the 17/17 breakup were falsely assigned to the 17/18 breakup channel.

Table 5.1: Comparison of the measured KER with the KER calculated by Stoychev, Kuleff, and Cederbaum [10].

	Theory	**Experiment**
H_2O-NH_3	~ 4.9 eV	-
NH_3-H_2O	~ 4.4 eV	4.3 ± 0.2 eV

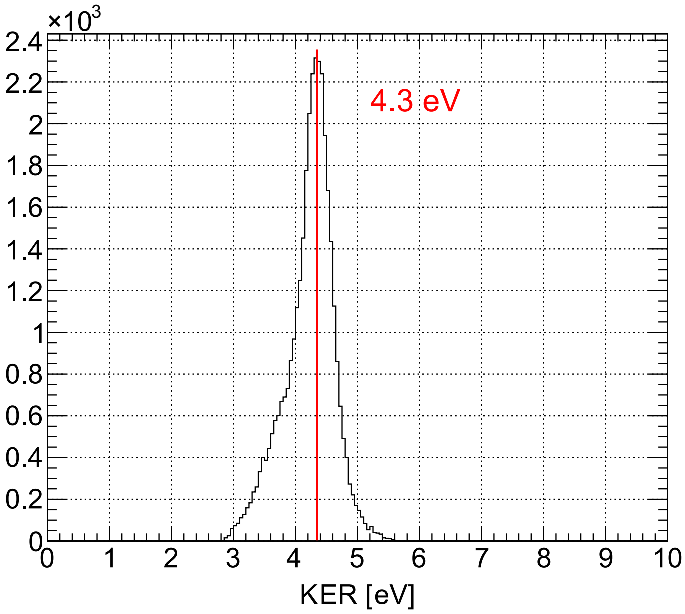

Figure 5.4: Measured kinetic energy release of both ionic fragments in channel 17/18.

5.2.2 Ionization processes

In order to emit two electrons prior to the Coulomb explosion, the $NH_3 \cdots H_2O$ molecule must gain a minimum energy higher than the two-site double ionization potential. For the identification of the different processes leading to the Coulomb explosion the electron energy spectra and the spectra combining the electron energy with the KER are examined. In addition the values of single and double ionization potentials, that are calculated based on an optimized geometry of the hydrogen bonded $NH_3 \cdots H_2O$, are used.

Double ionization

By absorbing a photon with an energy higher than the lowest double ionization threshold the system can be doubly ionized. As described in a previous chapter, there are two mechanism available for double ionization, the shake-off and the knock-off process. Since the shake-off process occurs only locally, thereby leaving the molecule in a one-site doubly ionized state, it can be disregarded. Consequently, the knock-off process is assumed to be the mechanism responsible for double ionization in $NH_3 \cdots H_2O$. However, as already mentioned in Section 5.1, the knock-off process usually occurs with relatively low probability.

After absorbing a photon with sufficient energy the residual energy above the double ionization threshold is continuously distributed to both electrons as their kinetic energy. Due to energy conservation the energy shared by the electrons must be constant. Hence, all events stemming from double ionization lie on a diagonal when plotting the electron energies against each other. Table 5.2 lists the two-site double ionization potentials ranging from 26 eV to 35 eV calculated by Stoychev, Kuleff, and Cederbaum [10]. Seven double ionization thresholds of $NH_3 \cdots H_2O$ lie below the photon energy of 36 eV. However, in the electron energy map shown in Figure 5.5 the diagonals are not distinctly visible but rather washed out. This might be due to the fact

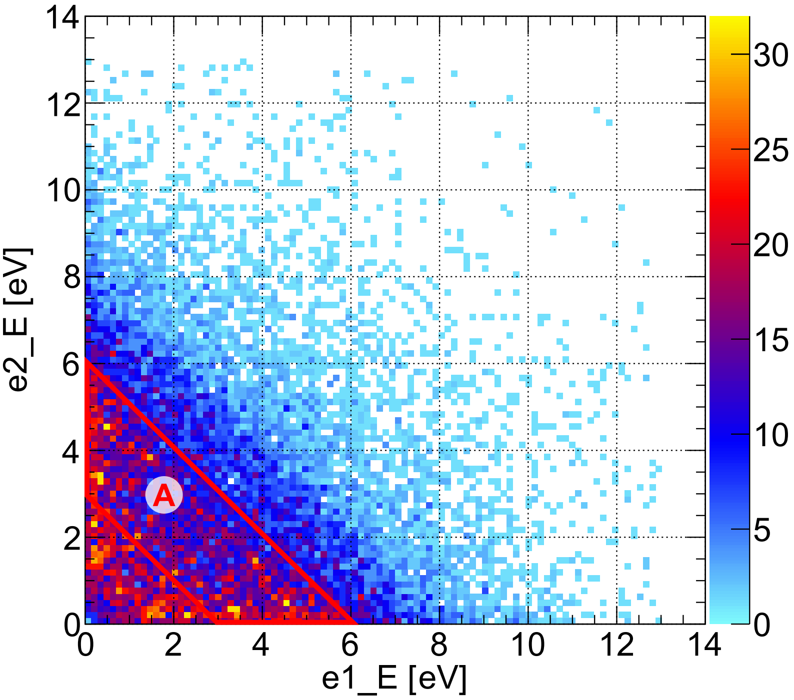

Figure 5.5: Energy of electron 2 plotted against the energy of electron 1 of the 17/18 breakup. Electron energy map is symmetrized. The electrons from region A are theoretically expected to stem from direct double ionization at the same time.

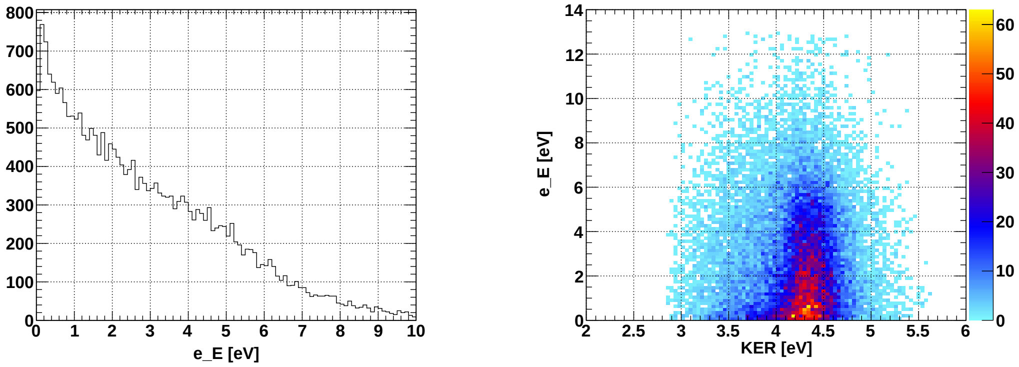

(a) **(b)**

Figure 5.6: **(a)** Kinetic energy of the electrons created in the 17/18 breakup. Most electrons have energies below 9 eV. **(b)** The spectrum of electron energies against the KER does not show any structure indicating a specific decay process.

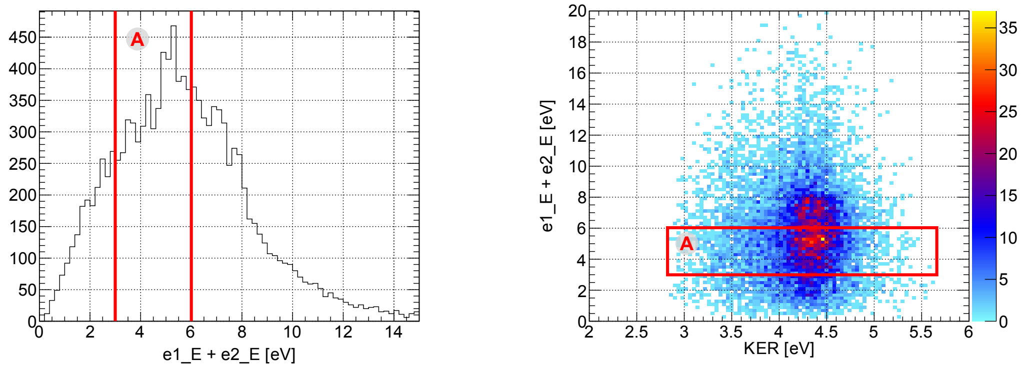

(a) **(b)**

Figure 5.7: (a) The sum of electron energies created in the 17/18 breakup shows a maximum at ~5 eV. **(b)** The sum of the electron energies plotted against the KER does not show any features which distinctly indicate a certain decay mechanism.

Table 5.2: Calculated double ionization potentials of $NH_3 \ldots H_2O$ below 36 eV and the resulting energy shared by emitted electrons [10].

	DIP [eV]	$E_{\mathrm{kin,e_1}} + E_{\mathrm{kin,e_2}}$ **[eV]**
two-site:		
$NH_3^+ + H_2O^+$	26.0	10
	28.5	7.5
	31.7	4.3
	32.1	3.9
	32.5	3.5
	34.5	1.5
	34.8	1.2
one-site:		
$NH_3^{++} + H_2O$	33.2	2.8
$NH_3 + H_2O^{++}$	39.1	-

that the ionization potentials are calculated only based on a optimized static geometry of the $NH_3 \cdots H_2O$ molecule. As illustrated in Figure 2.8, the DIPs include the KER. However, they do not consider the nuclear dynamics since they are calculated based on a static geometry. Under the condition of energy conservation the width of the KER distribution directly transfers to a broadening of the constant sum of electron energies. In addition to being blurred out, the diagonals lie very close to each other so that they might overlap. The electron energy map in Figure 5.6 does not show any structural features, although the sum of the electron energies shows a maximum between 3 eV and 6 eV as it can be seen in Figure 5.7a.

According to the calculated thresholds three double ionization diagonals should lie within the energy range of 3 eV to 6 eV. Setting a gate on the sum of the electron energies, which equals to cutting a diagonal in the energy map, and examining the distribution of the angle between the momenta of the electrons might reveal an indication for a direct process to be responsible for the double ionization. In the knock-off process the relative emission angle of the electrons depends on how the available energy is distributed among them after their collision. In general the emission of both electrons is preferentially back-to-back, i.e. with a relative angle of more than 90° [75]. Figure 5.8a shows that the emission of the second electron is more into the opposite hemisphere compared to the emission of both electrons into the same direction. In case of an asymmetric energy sharing shown in Figure 5.8c, the relative emission of the electrons does not have a preferred direction. If the available energy is more equally shared among the electrons the emission of both electrons into the same direction becomes less likely due to kinematic reasons. This phenomenon was shown in measurements with $C_2H_2F_2$ performed by Gaire et al. [75]. As seen in Figure 5.8b, the distribution of the relative angle of the electrons with roughly equal energy seems to show this phenomenon. However, it is not possible to interpret this indication as clear evidence for direct two-site double ionization. The more likely reason for the reduced emission of the electrons in the same direction is the detector inefficiency due to its dead time. If both electrons hit the detector within less than 5 ns they are not separately detected. In order to account for this multiple hit problem of the detector and to extract the real effect an advanced analysis of the event reconstruction is required.

In summary, it can be stated that although the $NH_3 \cdots H_2O$ molecule attributes many two-site double ionization potentials, direct double ionization cannot not be identified as the mechanism which is responsible for the break up. The electron energy map and the electron energies in combination with the measured KER do not give conclusive information on the decay process.

ICD

A system is energetically allowed to undergo ICD, if at least one DIP happens to lie below an inner-valence single ionization potential. The kinetic energy of the photoelectron is then given by the difference of the photon energy and the inner-valence single ionization potential. The ICD electron remains with the energy given by the difference between the IV SIP and the DIP which includes the KER. The ICD can be identified in the electron energy map as accumulation of events at the energies of the photoelectron and the ICD electron. Since the sum of KER and the energy of the ICD electron is constant, plotting the electron energy against the KER can also reveal ICD.

When examining the energy map of the electrons, that are created in breakups of $NH_3 \cdots H_2O$ shown in Figure 5.5, little information regarding ICD is obtained. Due to a manifold of states that are potentially involved in the ICD process the ICD electrons are emitted with different energies which in addition might overlap with the energies from the double ionization, as described above. According to the calculations by Stoychev, Kuleff, and Cederbaum $NH_3 \cdots H_2O$

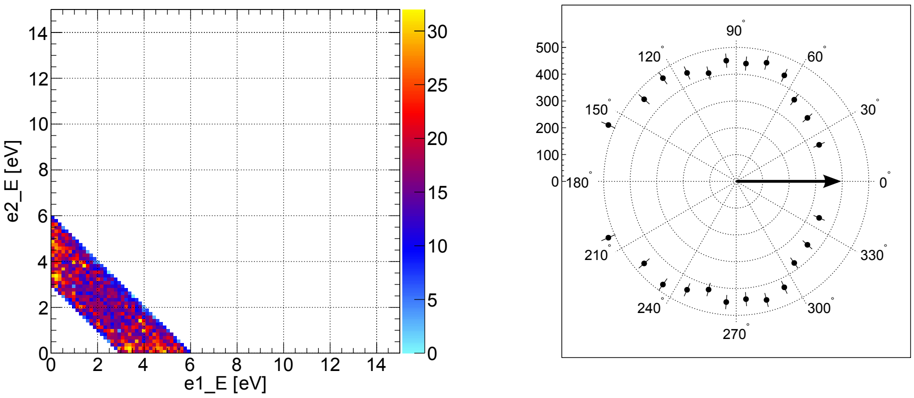

(a)

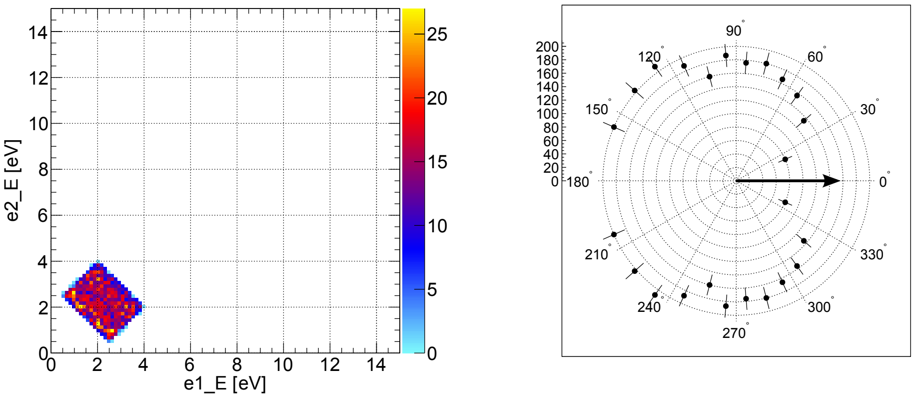

(b)

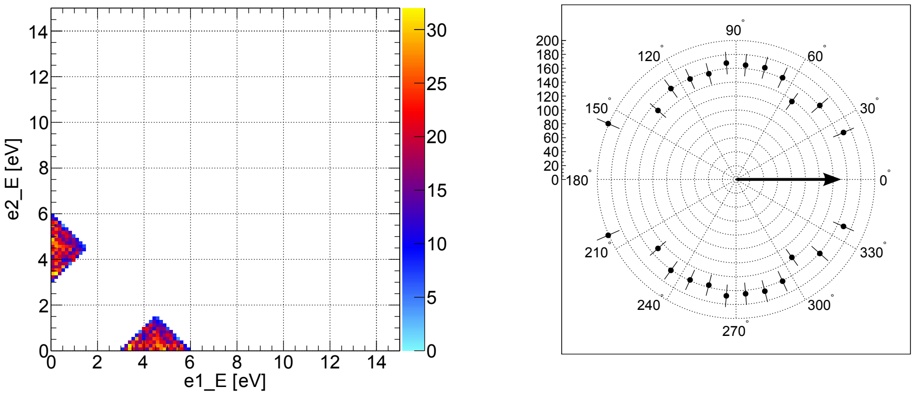

(c)

Figure 5.8: (a) Left: Energy map gated on electrons with an energy sum between 3 eV and 6 eV. **Right:** Cosine of the relative angle between the momenta of the two electrons. The angular distribution indicates a preference of a back-to-back emission. The direction of the first electron is indicated by the black arrow. **(b) Left:** Symmetric energy sharing among both electrons. **Right:** Distribution of relative angle indicates a lower probability of the emission into the same direction. **(c) Left:** Asymmetric energy sharing among the electrons. **Right:** The distribution of the relative emission angle is roughly isotropic, potentially due to a mix of direct and indirect double ionization process.

Table 5.3: One- and two-site double ionization potentials of $NH_3 \cdots H_2O$ with the resulting kinetic energy of the photoelectron and the ICD electron [10].

IV SIP [eV]	DIP [eV]	photoelectron [eV]	ICD electron [eV]
26.9	26.0	9.1	0.9
33.8	26.0	2.2	7.8
33.8	28.5	2.2	5.3
33.8	31.8	2.2	2.0
33.8	32.1	2.2	1.7
33.8	32.5	2.2	1.3

has various double ionization potentials lying above the inner-valence single ionization potential [10]. The potentials are listed in Table 5.3. Taking the variation of the KER of ±0.2 eV into account the energies of the ICD electron are described by a continuous distribution ranging from ~1 eV to ~8 eV. Due to the broad energy distribution of the ICD electrons and the overlap with the energy of the double ionization electrons, it is also challenging to distinctively identify ICD as a decay mechanism.

In conclusion, ICD is nevertheless assumed to be the main mechanism responsible for the $NH_3 \cdots H_2O$ breakup. The KER was measured in correspondence to the optimal equilibrium geometry of $NH_3 \cdots H_2O$, thus indicating that the decay occurs very fast. Furthermore the electron energy map shows that electrons pairs tend to consist of electrons each with high and low energy which is typical for ICD. Other decay mechanisms such as the knock-off process discussed in the previous Section 5.2.2 occur with lower probability than ICD.

5.3 $NH_3^+ + NH_3^+$ breakup

The third channel, that was identified from the measured data, is assigned to the breakup of molecules into ionic fragments, each of mass 17 au. With 26,000 events and respectively 8,500, when requiring full coincidence, it is almost as strong as the channel 17/18. Based on the original molecules, which were used to form the jet, the ammonia dimer $NH_3 \cdots NH_3$ is the system that is most likely to fragment into ions with masses 17 au. Other systems producing fragments such as OH^+ are less likely due to the proton transfer that is necessary prior to the Coulomb explosion. The hydrogen bonded system $NH_3 \cdots NH_3$ has been studied theoretically [9]. According to these studies the system is allowed to decay through different mechanisms subsequent to being doubly ionized due to its electronic structure.

5.3.1 Kinetic energy release

The kinetic energy release of $NH_3^+ + NH_3^+$, presented in Figure 5.9, was measured at 4.0 eV with a width of 0.3 eV FWHM. Based on the simple calculation of the static Coulomb potential of two ions, this KER corresponds to an initial distance of 3.6 Å between the two N atoms. As mentioned in Section 2.3.1, *ab initio* calculations suggest a distance in a range of 3.2 Å to 3.4 Å which corresponds to a KER greater than 4.0 eV. One possible explanation for the discrepancy between measured and calculated KER are rovibrational excitations that can occur during the decay process and lower the KER. Another possibility is that the distance between the two charges is not the same as the distance between the respective centers of mass.

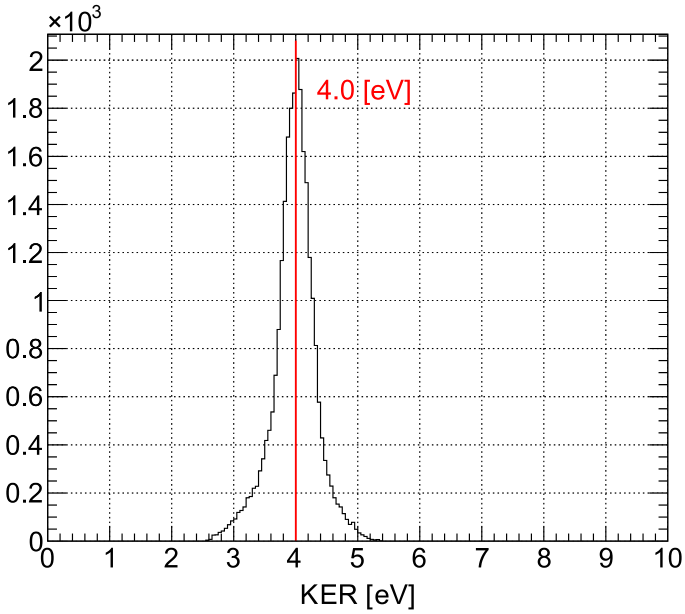

Figure 5.9: Kinetic energy release of two ionic fragments with mass 17 au and 17 au.

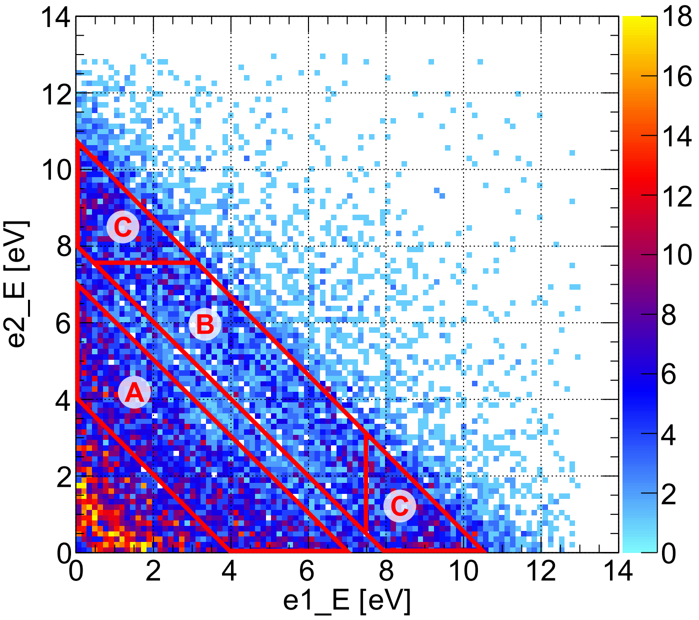

Figure 5.10: Energy of electron 2 plotted against the energy of electron 1 of the 17/17 breakup. Electron energy map is symmetrized. Electrons in region A and B presumably stem from direct double ionization, whereas region C contains electrons stemming from ICD.

5.3.2 Ionization processes

The ammonia dimers $NH_3 \cdots NH_3$ in the gas jet reacted with photons of 36 eV energy leading to double ionization with subsequent Coulomb explosion. In the following section the possible decay channels of the system are investigated by examining the measured electron energies and emission angles. For this purpose, the results of *ab initio* calculations of the electronic structure of $NH_3 \cdots NH_3$ are used.

Double ionization

As mentioned in the previous section, a molecular system can decay subsequent to direct double ionization, if the energy gained by absorbing a photon is higher than the lowest two-site double ionization potential. The distinct footprint of this decay mechanism is the constant energy, that is continuously distributed to the emitted electrons, appearing as a diagonal in the electron energy map. As can be seen in Figure 5.10, the electron energy map of channel 17/17 weakly indicates two diagonals, one in the range of 4 eV to 7 eV and the other between 9 eV and 11 eV. Furthermore, the sum of the kinetic energy of the electrons shown in Figure 5.12a features local maxima in the energy ranges which are associated with the two regions marked with A and B in the energy map. Other than that, no further features in the electron energy spectra can be identified. As seen in Figure 5.12b the KER itself does not show any visible substructure such as different vibrational modes or excited electronics states.

In order to determine the ionization process, in which the electrons from region A have been

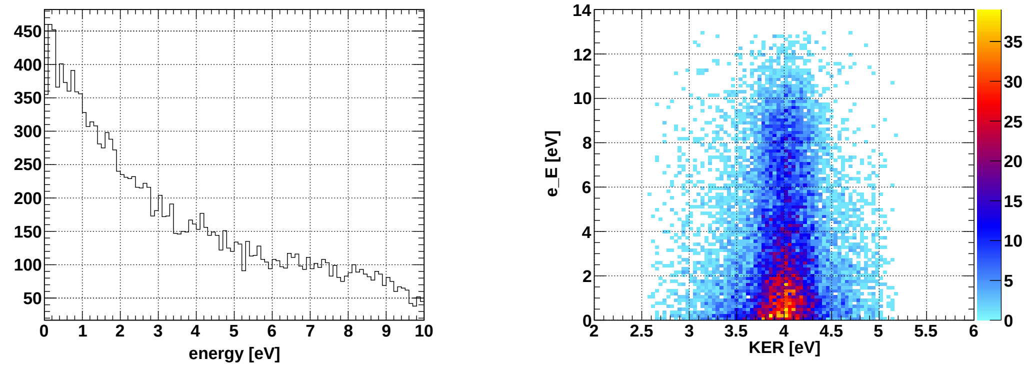

(a) **(b)**

Figure 5.11: **(a)** Kinetic energy release of electrons coincidently detected with a 17/17 breakup. **(b)** Electron energies plotted against the kinetic energy release of the ionic fragments.

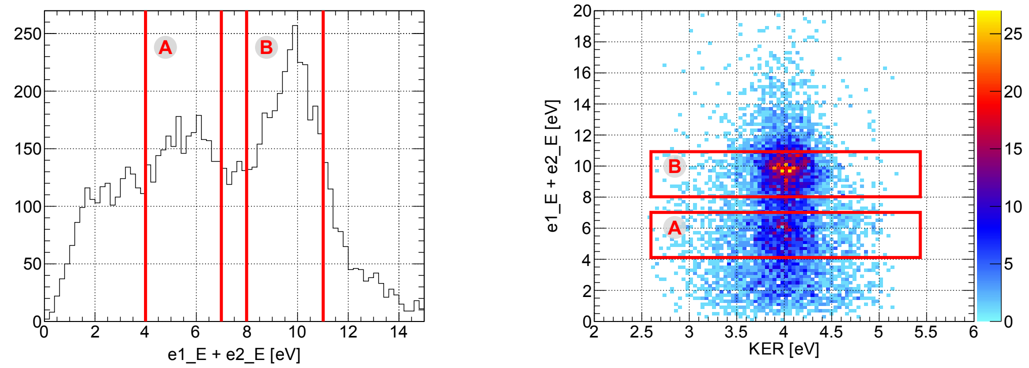

(a) **(b)**

Figure 5.12: **(a)** Sum of the energies of electron 1 and electron 2. **(b)** Sum of the energies of electron 1 and 2 plotted against the kinetic energy release.

Table 5.4: Calculated double ionization potentials of $NH_3 \ldots NH_3$ below 36 eV and resulting energy shared by the emitted electrons [9].

	DIP [eV]	$E_{\mathrm{kin,e_1}} + E_{\mathrm{kin,e_2}}$ **[eV]**
two-site:		
$NH_3^+ + NH_3^+$	24.7	11.3
	30.0	6.0
	30.5	5.5
	30.7	5.3
	35.3	0.7
one-site:		
$NH_3^{++} + NH_3$	33.9	2.1
	35.1	0.9
	35.3	0.7
	35.6	0.4
	35.9	0.1
	36.1	-
	36.3	-
	37.6	-

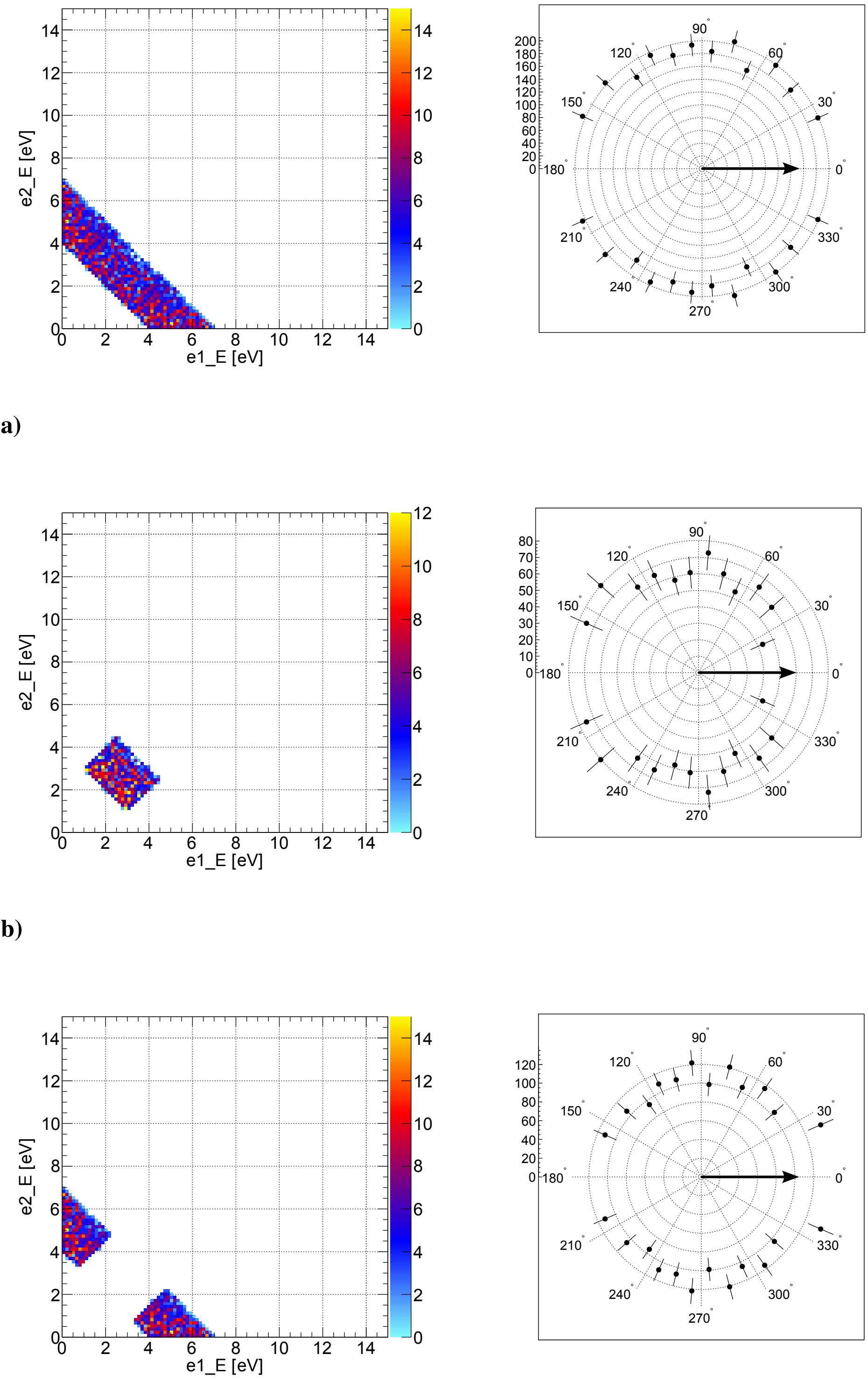

(a)

(b)

(c)

Figure 5.13: **(a) Left:** Energy map gated on electrons with an energy sum between 4 eV and 7 eV. **Right:** Cosine of the relative angle between the momenta of the two electrons. The angular distribution does not show a preferred direction of the electrons. The direction of the first electron is indicated by the black arrow. **(b) Left:** Symmetric energy sharing among both electrons. **Right:** Distribution of relative angle indicates a lower probability of the emission into the same direction which is likely due to the multiple hit inefficiency of the detector. **(c) Left:** Asymmetric energy sharing among the electrons. **Right:** The distribution of the relative emission angle appears isotropic.

created, the distribution of the relative angle between the momenta of the two electrons is examined. Unlike expected for a direct double ionization process, the electrons do not have a preferential emission direction relative to each other as seen in Figure 5.13a. For a symmetric energy sharing shown in Figure 5.13b, the distribution of the relative angle is less isotropic with a lower tendency of the electrons to be emitted into the same direction. This, however, is likely to be due to the multiple hit inefficiency of the detector. If the energy is unequally shared, the emission direction of the electrons seems again uncorrelated as shown in Figure 5.13c.

Although theoretical calculations of the ionization thresholds by Kryzhevoi and Cederbaum in $NH_3 \cdots NH_3$ suggest three two-site double ionization potentials between 30 eV and 31 eV leading to 5 eV to 6 eV shared by the electrons in the case of direct double ionization (see Table 5.4), the data does not clearly confirm direct double ionization as the dominant process responsible for the decay. As already mentioned with regards to the fragmentation of $H_2O \cdots H_2O$ and $NH_3 \cdots H_2O$, complex molecular systems have many internal degrees of freedom where the energy of the absorbed photon can be deposited. Hence, in addition to the direct effect of the width of the KER distribution, also vibrational, rotational and other electronic excitations might lead to an uncertainty of the double ionization potentials.

In conclusion, it cannot distinctly be ascertained that direct double ionization is the responsible process of creating electrons with an energy sum between 4 eV and 7 eV.

The second diagonal in the energy map marked as region B in Figure 5.10 is vaguely visible. Even though the diagonal is centered around the energy sum of ~10 eV it only partly contributes to the peak from Figure 5.12a. The other contribution to the peak stems from the noticeable clusters at both ends of the diagonal which are assumed to indicate ICD and are discussed in the next Section 5.3.2. Examining the relative angular distribution of the emission of the electrons from region B does not give viable information about direct double ionization as a responsible process. As seen in Figure 5.14, the electrons tend to be emitted back-to-back. However, the emission distribution remains the same regardless of the energy sharing. In addition to the fact, that gating on the electron energies significantly lowers the statistics, it is obvious form the energy map that region B overlaps with region C, which indicates another decay mechanism. Furthermore a comparison with the calculated double ionization potentials reveals that the diagonal is expected to appear at a slightly higher energy. The lowest DIP in $NH_3 \cdots NH_3$ lies at ~25 eV [9], so that after absorbing a photon with 36 eV an energy of ~11 eV is shared by the emitted electrons.

Due to all reasons mentioned so far, it is challenging to draw meaningful conclusions about the existence of direct double ionization creating electrons with an energy sum of 8 eV to 11 eV.

ICD

ICD is a very efficient decay process, that a system is allowed to undergo, if its IV SIP lies above one of its DIP. In general the likelihood of ICD increases with the number of allowed decay channels[2]. In $NH_3 \cdots NH_3$ two SIPs with considerable intensity lie above the DIP at ~25 eV [9]. The kinetic energy of the photoelectron is solely determined by the IV SIP, whereas the energy of the ICD electron depends on the OV SIP and the KER. Since the double ionization potential calculated by Kryzhevoi and Cederbaum already includes the KER, the expected energy of the ICD electron is obtained by subtracting the DIP from the higher IV SIP. Using photons with an energy of 36 eV to induce the reaction, the ICD electrons are expected to have relatively low

---

[2] One decay channel refers to one combination of IV and OV SIP that is involved in the process. Often, a core hole can be filled by more than one OV electron of the neighboring molecules. Thus each electron represents one possibility to decay which is referred as decay channel.

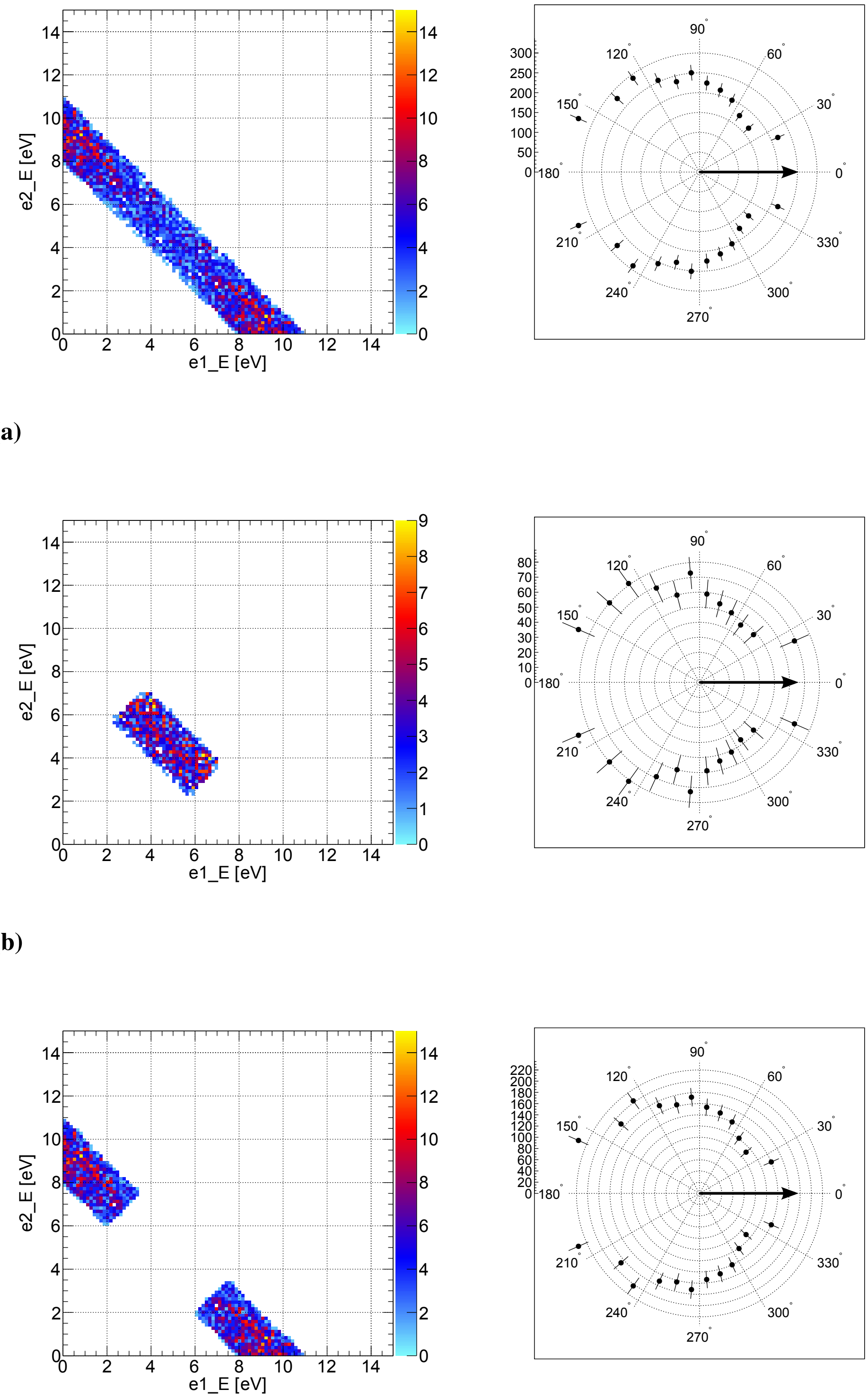

(a)

(b)

(c)

Figure 5.14: (a) Left: Energy map gated on electrons with an energy sum between 8 eV and 11 eV. **Right:** Cosine of the relative angle between the momenta of the two electrons. The angular distribution shows that preferential emission is back-to-back. The direction of the first electron is indicated by the black arrow. **(b) Left:** Symmetric energy sharing among both electrons. **Right:** The preferential emission direction of the electrons is back-to-back. **(c) Left:** Asymmetric energy sharing among the electrons. **Right:** The preferential emission direction of the electrons is back-to-back.

Table 5.5: One- and two-site double ionization potentials of $NH_3 \cdots NH_3$ with the resulting kinetic energy of the photoelectron and the ICD electron [9].

IV SIP [eV]	DIP [eV]	photoelectron [eV]	ICD electron [eV]
26.8	24.7	9.2	2.1
27.6	24.7	8.4	2.9

energy compared to the photoelectrons. Table 5.5 lists the electron energies depending on the involved SIP and DIP calculated by Kryzhevoi and Cederbaum.

As seen in Figure 5.11, the total electron energy itself as well as in relation to the KER does not show any noticeable structure. However, restricting the sum of the electron energy to the range of 8 eV to 11 eV (see region B in Figure 5.10) reveals two maxima in the electron energy as seen in Figure 5.15a.

In order to characterize the electrons in these two energy regions their emission direction in the laboratory system is examined. In Figure 5.15b the electron energy is plotted against the cosine of the angle between the electron momentum and the ToF-direction along the spectrometer axis. The preferential emission direction of electrons with energies from 7 eV to 10 eV is along the spectrometer axis whereas the emission of electrons with an energy smaller than 3 eV is more evenly distributed. The angular distributions become even more distinct when gating the electron energies on region C.

The emission of the high energy electron has a strong dipole like shape along the ToF-direction shown in Figure 5.16a. According to the theory of single photoionization, the emission angular distribution of the electron withdrawn from a $1s$-orbital by a linearly polarized photon is given by the differential cross section described by $\beta = 2$ (see equation 2.70 and Figure 2.4) which resembles a dipole shaped distribution along the direction of the polarization. Hence, in accordance with the expected energy of the photoelectron at 8.4 eV and 9.2 eV, respectively, and the angular distribution of a photoelectron, it can be concluded that the high energy electrons from region C stem from inner-valence photo ionization.

In the ICD process the second electron is removed from an outer-valence shell using the freed-up de-excitation energy. Since the emission of the ICD electron occurs independently from the preceding photoionization, its emission direction is primarily isotropic. The measured angular distribution of the low energy electron in Figure 5.16b shows emission in all directions, however with a small preference perpendicular to the ToF-direction. Taking the uncertainty of the KER and possible excitation of rovibrational modes into account the energy range 0 eV to 3 eV is considered as in accordance with the calculated energies of the ICD electron.

In summary, it can be concluded that the electrons measured at energies from region C most likely represent the photoelectron and the ICD electron produced in intermolecular Coulombic decay of the ammonia dimer $NH_3 \cdots NH_3$.

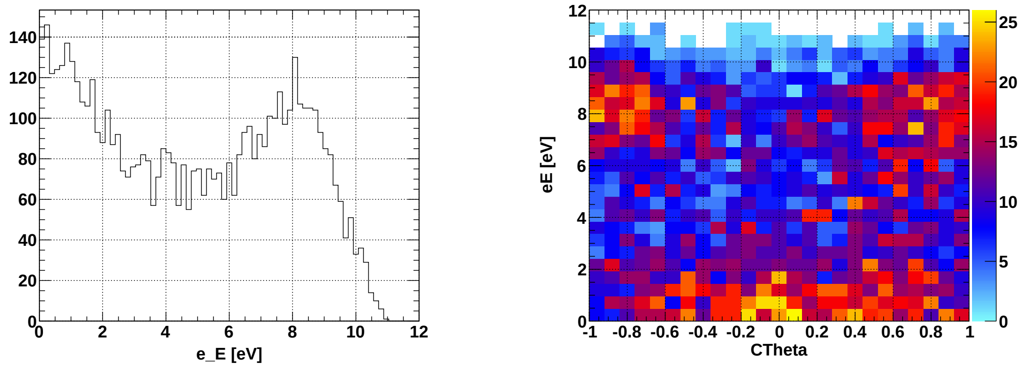

(a) **(b)**

Figure 5.15: **(a)** Energy of electrons from region B. **(b)** The energy of electrons form region B plotted against the cosine of the polar angle θ.

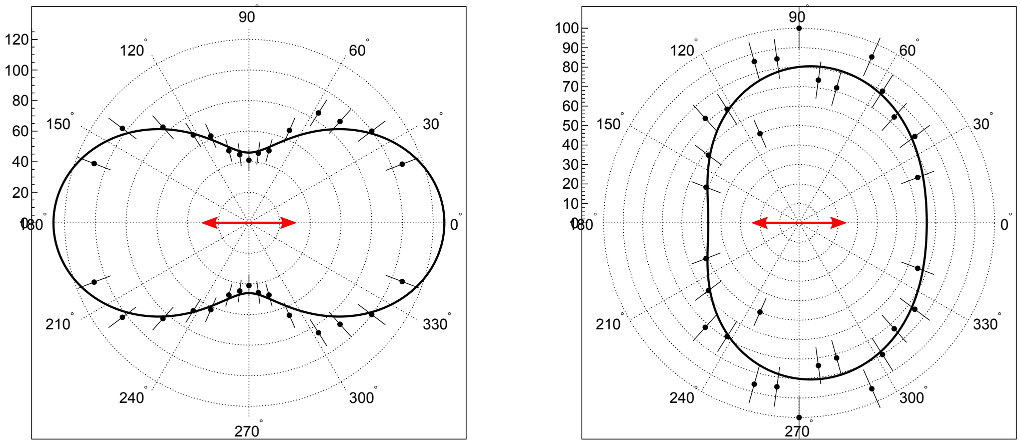

(a) **(b)**

Figure 5.16: **(a)** The angular distribution of the high energy electrons form region C is dipole shaped which is typical for photoelectrons. **(b)** The angular distribution of the low energy electrons from region C is rather isotropic.

5.4 Molecular composition of the gas jet

The occurrence of different ionization processes such as direct double ionization or ICD in molecular systems depends on the arrangement of the ionization potentials of the system, which are determined by its nuclear geometry and electronic structure. This structure, however, can be affected by the presence of neighboring systems, for example by establishing a hydrogen bond or Van-der-Waals bond, leading to altered ionization potentials with consequences for the allowed ionization processes. In their recent work, Kryzhevoi and Cederbaum demonstrated that protonation and deprotonation of ammonia dimers theoretically enhance or terminate ICD as a possible decay mechanism by altering the single and double ionization potentials [9]. Conceiving protonation and deprotonation as altering the pH-value they concluded that intra-molecular dynamics might be controllable by macroscopic parameters of the environment. With regards to the presented experiment the environment of the reacting target molecules is represented by the supersonic gas jet. Although in the beginning of the experiment conceived as a difficulty, the continuous alteration of the molecular composition of the gas jet turned out to be an interesting object to investigate. In the following section an approach of how to examine the molecular composition is presented. Furthermore, possible implications on the measured breaksups are discussed.

In the gas jet various molecular clusters of different sizes were formed. Although in the experiment it was aimed for optimal conditions (driving pressure of the ammonia, temperature of the water reservoir, the gas line and the nozzle) in order to achieve a maximum yield of dimers, the majority of the particles in the jet were single molecules NH_3 and H_2O. These molecules were ionized and detected as background particles. Compared to the fragments stemming from a Coulomb explosion, these ions have no initial momentum. Hence, they were detected within a small area on the MCP, the so called jet dot. Figure 5.17 shows the ion ToF spectrum plotted against an excerpt of the event counter. Since the count rates were very stable during the experiment, the event counter can be considered as an arbitrary unit of time. In the figure it can be seen that all masses from 18 u to 14 u are represented and their intensities fluctuate over time due to changes of experimental conditions. Integrating the area under each peak gives the number of detected ions per 1.5×10^6 events. Under the assumption that the single ionization cross sections of each molecules are constant, the number of detected ions are proportional to the concentration of the molecules in the gas jet. Hence, the ion ToF as a function of the event counter gives information about composition of the gas jet, yet only for single molecules.

This analytical approach shows that the data was taken under two different conditions regarding the concentration of water and ammonia in the jet. As seen in Figure 5.18 some measurement series show a high concentration of ammonia relative to water, whereas others show a lower concentration. Series I, E and J were taken during the first half of the beamtime when the experimental parameters were optimized for a maximum yield of $NH_3 \cdots H_2O$. The other data series J_30psi, K, L_30psi and N were taken thereafter with a focus on a higher yield of $NH_3 \cdots NH_3$ in the jet.

In Table 5.6 the counts of singly ionized molecules, of breakups in channel 17/18 and 17/17 as well as of ICD events (gated on region C in Figure 5.10) are listed for each measurement series. From these numbers, two conclusion that can be drawn.

Firstly, the data shows that the number of observed 17/18 breakups relative to 17/17 breakups increases with the concentration of water in the jet. Assuming a fixed probability for NH_3 and H_2O to form hydrogen bonds, this trend is in line with the expectation that a higher concentration of water leads to an increased number of $NH_3 \cdots H_2O$ in the jet. However, the high yield of 17/18 breakups despite a relatively low concentration of water in the jet is surprising. This might be

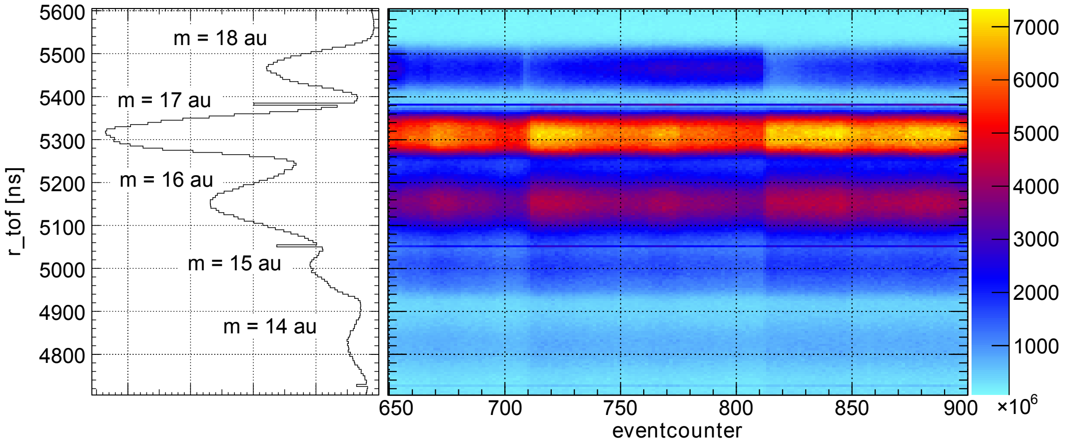

Figure 5.17: The ToF of singly charged ion without starting momentum, which are detected in the jet dot, plotted against the event counter. Each line corresponds to an ion mass.

either due to a higher probability of the formation of $NH_3 \cdots H_2O$ in the jet or due to a relatively high ionization probability of $NH_3 \cdots H_2O$ with subsequent Coulomb explosion. Unfortunately, without further specific information these explanatory approaches remain speculative.

Another interesting observation is the yield of ICD events in the breakup channel 17/17. As seen in Table 5.6 for the measurement series J_30psi, K, L_30psi and N, the share of ICD events in 17/17 breakups is significantly higher when the concentration of water in the jet is low. Solely based on these numbers this would mean that the probability for ICD of $NH_3 \cdots NH_3$ increased due to the altered molecular composition of the jet. However, there are various uncertainties that need to be taken into account before drawing any conclusion regarding the ICD probability of ammonia dimers. First of all, the validity of the obtained numbers is limited due to little statistics. The count rates of four-particle-coincidences in a COLTRIMS experiments are generally low. Thus, the number of ICD events for each measurement series is in the order of 10^2. Another uncertainty comes from the fact, that it is not possible to ultimately conclude the molecular composition in the jet from the measured fragments without making assumptions on single and double ionization cross sections as well as concentration of clusters. As discussed previously, for this purpose the information gained from counting singly ionized molecules and breakups is not sufficient.

Conclusively, it can be stated that the change of the experimental conditions during the experiment affected the concentrations of water and ammonia in the gas jet. As expected, the yield of the 17/18 breakup during measurement series with a high water concentration was accordingly higher. Although the yield of ICD events in the 17/17 breakup indicates little variation depending on the ratio between the water and ammonia concentration in the gas jet, no meaningful conclusion can be drawn due to little statistics and missing information on the cluster concentration.

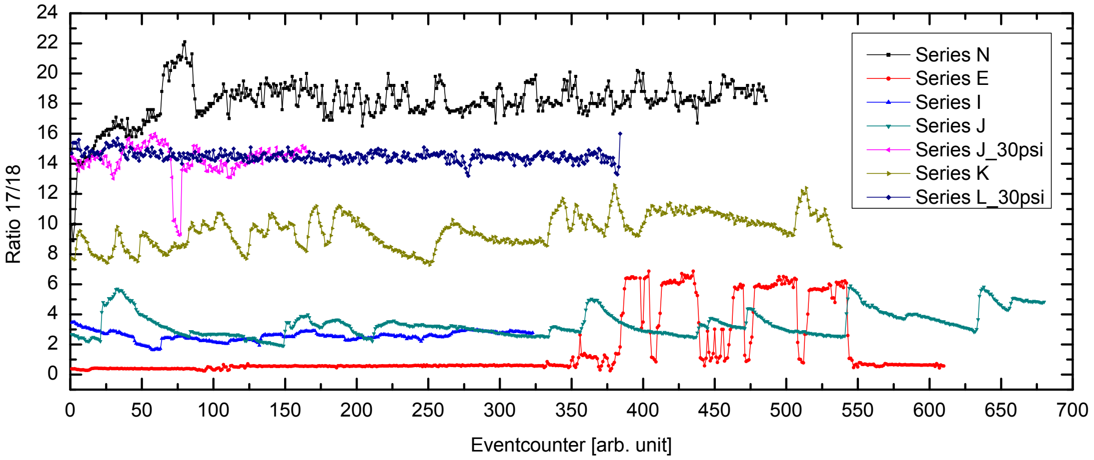

Figure 5.18: The count ratio of ions with mass 17 and 18 plotted against the event counter for different measurement series. The ratios vary greatly among the measurement series. In addition, they are not stable throughout each measurement series.

Table 5.6: Yields of the singly charged ions, 17/17 and 18/18 breakups as well as ICD events in the 17/17 channel for different measurement series.

	Single ionization			**Breakups**			
	Total	**17**	**18**	**Total**	**17/18**	**17/17**	**ICD in 17/17**
Low driving pressure							
Series E	1.0×10^8	45%	55%	2593	89%	11%	9%
Series I	4.7×10^7	72%	28%	1296	88%	12%	7%
Series J	1.0×10^8	76%	24%	2857	88%	12%	11%
High driving pressure							
Series J_30psi	2.3×10^7	93%	7%	1319	50%	50%	17%
Series K	7.9×10^7	90%	10%	4188	71%	29%	16%
Series L_30psi	5.5×10^7	94%	6%	3451	52%	48%	17%
Series N	6.0×10^7	95%	5%	5384	21%	79%	20%

Chapter 6

Summary

In the presented work the decay upon photon impact of small hydrogen bonded systems has been investigated using the COLTRIMS method. In the COLTRIMS experiment a supersonic gas jet of the molecules NH_3, H_2O and clusters of these two molecules was crossed with a beam of photons with an energy of 36 eV. The energetics of the thereby induced reactions were measured by calculating the 3d-momenta of the detected particles. In the data analysis several different molecular fragmentations were identified and analyzed.

The fragmentation into ions with masses of 18 au each was assigned to the breakup of water dimers into $H_2O^+ + H_2O^+$. Both, the measured KER at 4.2 eV and the range of the electron energies from 0 eV to 8 eV are in accordance with previous measurements by Jahnke et al. [30]. Although ICD is assumed to be the mechanism mainly responsible for the decay, it could not be distinctly identified in the data. Due to a manifold of states involved in the decay process the electron energy appeared washed out making it challenging to extract valuable information.

The breakup of ionic fragments with masses 17 au and 18 au was assigned to the ions NH_3^+ and H_2O^+. The comparison of the measured KER at 4.3 eV with the theoretical KER calculated by Stoychev, Kuleff, and Cederbaum [10] revealed that the cluster fragmenting into NH_3^+ and H_2O^+ is the hydrogen bonded $NH_3 \cdots H_2O$ with ammonia as the proton-donor. The KER of the cluster $H_2O \cdots NH_3$ with ammonia as proton-acceptor is expected to be 0.5 eV higher than the measured KER. Hence, $H_2O \cdots NH_3$ could be excluded as a candidate for the 17/18 breakup. According to the calculations some of the double ionization potentials in $NH_3 \cdots H_2O$ lie below the inner-valence single ionization potential of the N and O atom thereby allowing the system to undergo ICD. Although the energy range of the detected electrons in general corresponded to the calculated ionization potentials, no noticeable substructure indicating a specific decay mechanism was identified. In addition to a manifold of electronic transitions, the system features many other internal degrees of freedom so that the absorbed energy can be partly stored in rovibrational excitations thereby blurring the energetics of the decay process. Direct double ionization could not be identified from the electron energy map. Also, the distribution of the relative emission angle of the electrons did not reveal useful information. However, many electron pairs consisting of one electron with high and one with low energy were found. Since this energy sharing is typical for electron pairs created in ICD, it is assumed to be the mechanism mainly responsible for the decay of $NH_3 \cdots H_2O$.

The third channel, that was identified, was assigned to the break up of ammonia dimers into NH_3^+ and NH_3^+ with masses of 17 au each. The kinetic energy release was measured at 4.0 eV which corresponds to an initial distance between the nitrogen atoms of 3.6 Å. This distance is not in accordance with theoretical calculations suggesting a distance ranging from 3.2 Å to 3.4 Å in the optimal geometry of the dimer. According to *ab initio* calculations by Kryzhevoi and Cederbaum the ammonia dimer has several double ionization potentials lying below the inner-valence single ionization potential of the N atom [9]. Hence, the system is energetically allowed to undergo ICD. The examination of the electron energies revealed indications of double ionization and ICD as decay mechanisms. However, direct double ionization could not distinctively be confirmed. The distribution of the relative emission angle of the electrons with the expected energies was distorted by the multiple hit inefficiency of the detector, thus making it impossible to extract the real physical effect without further advanced analysis. ICD, indicated by electron pairs consisting of a photoelectron and an ICD electron, was identified. The energy of the high energy electron was measured in a range of 7 eV to 10 eV, which is in accordance with the theoretically expected energies of the photoelectron at 8.4 eV and 9.2 eV. The high energy electron was distinctively identified as the photoelectron based on its emission angular distribution which is dipole shaped and parallel to the polarization direction of the photons. The other electron was measured with an energy below 3 eV which is in line with the expected energies of 2.1 eV and 2.9 eV. Its angular distribution does not show a preferred emission direction in the laboratory system.

Finally, the molecular composition of the gas jet was examined. For this purpose, the yield of the singly ionized monomers was analyzed as a function of the event counter. Beside the fact that the concentrations of water and ammonia molecules in the jet did not remain stable during the measurements, two types of measurement series with different ammonia water ratios were identified. Changed experimental conditions, such as the driving pressure of the gas, are considered as a possible reason for the different ion ratios. The comparison of the 17/17 and 17/18 breakup yield for the different types of measurement series revealed, that the 17/18 breakup occurred more often when the concentration of water in the jet was higher. Reliable conclusions about the dependency of ICD probabilities on the molecular composition of the gas jet could not be drawn.

Appendix A

Atomic units

For convenience in atomic and molecular physics special units are used. These units are normalized to the dimensions of an electron in the ground state of a hydrogen atom. This means that the relevant physical constants are set to 1 thereby simplifying the numeric values of the physical units. The following table lists the conversion factors from atomic units to SI units.

Table A.1: Conversion from atomic units to SI units.

Physical unit	**Atomic unit**	**SI unit**
Length	$1\text{ au} = 0.529 \times 10^{-10}\,\text{m} = a_0$	$1\,\text{m} = 1.890 \times 10^{10}$ au
Time	$1\text{ au} = 2.419 \times 10^{-17}\,\text{s}$	$1\,\text{s} = 4.134 \times 10^{16}$ au
Velocity	$1\text{ au} = 2.188 \times 10^{6}\,\text{m/s} = c \cdot \alpha$	$1\,\text{m/s} = 4.571 \times 10^{-7}$ au
Mass	$1\text{ au} = 9.109 \times 10^{-31}\,\text{kg} = m_\text{e}$	$1\,\text{kg} = 1.098 \times 10^{30}$ au
Charge	$1\text{ au} = 1.602 \times 10^{-19}\,\text{A}\,\text{s} = e$	$1\,\text{A}\,\text{s} = 6.166 \times 10^{18}$ au
Energy	$1\text{ au} = 4.360 \times 10^{-18}\,\text{J} = 27.212\,\text{eV}$	$1\,\text{J} = 2.294 \times 10^{17}$ au
Momentum	$1\text{ au} = 1.993 \times 10^{-24}\,\text{kg}\,\text{m/s}$	$1\,\text{kg}\,\text{m/s} = 5.018 \times 10^{23}$ au
Angular mom.	$1\text{ au} = 1.055 \times 10^{-34}\,\text{kg}\,\text{m}^2/\text{s} = \hbar$	$1\,\text{kg}\,\text{m}^2/\text{s} = 9.482 \times 10^{33}$ au

Appendix B

Parameters of the experiment

Table B.1: Parameters of the experiment performed at the Advanced Light Source in Berkeley.

Photon beam		
Energy	36.0 eV	
Polarization	horizontal, along $\vec{z}$-axis	
Entrance slit	15 µm	
Exit slit	15 µm	
Bunch spacing	328.266 ns	
Bunchmarker shift	~−195.5 ns	
Gas jet		
Target	$NH_3 \cdots NH_3$ and $NH_3 \cdots H_2O$	
Driving pressure (NH_3)	0.1 bar to 1.0 bar	
Reservoir temperature (H_2O)	room temperature ~300 K	
Gas line temperature	~370 K	
Nozzle temperature	373 K to 400 K	
Nozzle diameter	50 µm	
Jet velocity	~850 m/s	
Vacuum (orders of magnitude only)		
Source stage	10^{-4} mbar to 10^{-5} mbar	
2nd stage	10^{-6} mbar to 10^{-7} mbar	
Main chamber	10^{-8} mbar	
Jet dump	10^{-8} mbar	
Spectrometer		
Magnetic field	6.81 gauss	
Acceleration field (uniform)	5.327 V/cm	
	Electron side	**Ion side**
Acceleration length	70.5 mm	36.5 mm
Drift length	137 mm	–
Boost length	5 mm	22 mm
Boost field	600 V/cm	906 V/cm
Detectors		
	Electron side	**Ion side**
Anode	HEX80	DLD120
Potential MCP front	200 V	−2150 V
Potential Anode holder	2629 V	199 V
Rate	~30 kHz	10 kHz to 15 kHz

Bibliography

[1] T. Ouchi et al. "Three-Electron Interatomic Coulombic Decay from the Inner-Valence Double-Vacancy States in NeAr". In: *Phys. Rev. Lett.* 107 (5 2011), p. 053401.

[2] LS Cederbaum, J Zobeley, and F Tarantelli. "Giant intermolecular decay and fragmentation of clusters". In: *Physical review letters* 79.24 (1997), p. 4778.

[3] T Jahnke et al. "Experimental Observation of Interatomic Coulombic Decay in Neon Dimers". In: *Physical review letters* 93 (2004), pp. 163401–163401.

[4] S. Marburger et al. "Experimental Evidence for Interatomic Coulombic Decay in Ne Clusters". In: *Phys. Rev. Lett.* 90 (20 2003), p. 203401.

[5] Badia Boudaïffa et al. "Resonant formation of DNA strand breaks by low-energy (3 to 20 eV) electrons". In: *Science* 287.5458 (2000), pp. 1658–1660.

[6] G Hanel et al. "Electron attachment to uracil: Effective destruction at subexcitation energies". In: *Physical review letters* 90.18 (2003), p. 188104.

[7] Joanna Berdys et al. "Damage to model DNA fragments from very low-energy (< 1 eV) electrons". In: *Journal of the American Chemical Society* 126.20 (2004), pp. 6441–6447.

[8] Robyn Barrios, Piotr Skurski, and Jack Simons. "Mechanism for damage to DNA by low-energy electrons". In: *The Journal of Physical Chemistry B* 106.33 (2002), pp. 7991–7994.

[9] Nikolai V Kryzhevoi and Lorenz S Cederbaum. "Using pH Value To Control Intermolecular Electronic Decay". In: *Angewandte Chemie International Edition* 50.6 (2011), pp. 1306–1309.

[10] Spas D Stoychev, Alexander I Kuleff, and Lorenz S Cederbaum. "Intermolecular Coulombic decay in small biochemically relevant hydrogen-bonded systems". In: *Journal of the American Chemical Society* 133.17 (2011), pp. 6817–6824.

[11] Wolfgang Nolting. *Grundkurs Theoretische Physik 5/1*. Springer, 2009.

[12] Wolfgang Demtröder. *Atome, Moleküle und Festkörper, Volume 3 of Experimentalphysik*. 2005.

[13] Jens Peder Dahl. *Introduction to the quantum world of atoms and molecules*. World Scientific, 2001.

[14] Ingolf V. Hertel and C.-P. Schulz. *Atome, Moleküle und Optische Physik 1: Atomphysik und Grundlagen der Spektroskopie*. Vol. 1. Springer-Verlag, 2008.

[15] Pierre Hohenberg and Walter Kohn. "Inhomogeneous electron gas". In: *Physical review* 136.3B (1964), B864.

[16] B.H. Bansden and C.J. Joachim. *Physics of Atoms and Molecules*. Pearson Education Limited, 2003.

[17] Volker Schmidt. *Electron spectrometry of atoms using synchrotron radiation*. Vol. 1. Cambridge University Press, 1997.

[18] Ingolf V. Hertel and C.-P. Schulz. *Atome, Moleküle und Optische Physik 2: Molekule und Photonen - Spektroskopie und Streuphysik*. Vol. 1. Springer-Verlag, 2008.

[19] Ivan Powis et al. "Photoion anisotropy in dissociative photoionization of CF3I". In: *The Journal of chemical physics* 92.3 (1990), pp. 1643–1652.

[20] Toshio Masuoka, Inosuke Koyano, and Norio Saito. "Anisotropic angular distribution of fragment ions in dissociative double photoionization of OCS". In: *Physical Review A* 44.7 (1991), p. 4309.

[21] Reinhard Dörner et al. "Double ionization by one and many photons". In: *Radiation Physics and Chemistry* 70.1 (2004), pp. 191–206.

[22] James AR Samson. "Proportionality of electron-impact ionization to double photoionization". In: *Physical review letters* 65.23 (1990), p. 2861.

[23] B Gaire et al. "Photo-double-ionization of ethylene and acetylene near threshold". In: *Physical Review A* 89.1 (2014), p. 013403.

[24] Alexandra Knapp et al. "Mechanisms of photo double ionization of helium by 530 eV photons". In: *Physical review letters* 89.3 (2002), p. 033004.

[25] T Havermeier et al. "Single photon double ionization of the helium dimer". In: *Physical review letters* 104.15 (2010), p. 153401.

[26] Pierre Auger. *Sur les rayons [beta] secondaires prodiuts dans un gaz par des rayons x*. Gauthier-Villars, 1925.

[27] VV Kuznetsov and NA Cherepkov. "Auger decay of fixed-in-space linear molecules". In: *Journal of electron spectroscopy and related phenomena* 79 (1996), pp. 437–440.

[28] Nestor Correia et al. "Theory of band shape formation in Auger and autoionization spectra of molecules. Numerical applications and new high-resolution spectra for CO". In: *The Journal of chemical physics* 83.5 (1985), pp. 2035–2052.

[29] Th Weber et al. "Auger electron emission from fixed-in-space CO". In: *Physical review letters* 90.15 (2003), p. 153003.

[30] T Jahnke et al. "Ultrafast energy transfer between water molecules". In: *Nature Physics* 6.2 (2010), pp. 139–142.

[31] T Jahnke. "Interatomic and intermolecular Coulombic decay: the coming of age story". In: *Journal of Physics B: Atomic, Molecular and Optical Physics* 48.8 (2015), p. 082001.

[32] T Jahnke et al. "Experimental separation of virtual photon exchange and electron transfer in interatomic Coulombic decay of neon dimers". In: *Physical review letters* 99.15 (2007), p. 153401.

[33] S Scheit, LS Cederbaum, and H-D Meyer. "Time-dependent interplay between electron emission and fragmentation in the interatomic Coulombic decay". In: *The Journal of chemical physics* 118.5 (2003), pp. 2092–2107.

[34] R Santra et al. "Intermolecular Coulombic decay of clusters". In: *Journal of Electron Spectroscopy and Related Phenomena* 114 (2001), pp. 41–47.

[35] Sudhir A Kulkarni and Rajeev K Pathak. "Ab initio investigations on neutral clusters of ammonia:(NH 3) n (n= 2–6)". In: *Chemical physics letters* 336.3 (2001), pp. 278–283.

[36] N Colin Baird. "Simulation of hydrogen bonding in biological systems: Ab initio calculations for NH3NH3 and NH3NH4+". In: *International Journal of Quantum Chemistry* 8.S1 (1974), pp. 49–54.

[37] William L Jorgensen and Mustafa Ibrahim. “Structure and properties of liquid ammonia”. In: *Journal of the American Chemical Society* 102.10 (1980), pp. 3309–3315.

[38] DD Nelson Jr, GT Fraser, and W Klemperer. “Ammonia dimer: A surprising structure”. In: *The Journal of chemical physics* 83.12 (1985), pp. 6201–6208.

[39] DD Nelson Jr et al. “Ammonia dimer: Further structural studies”. In: *The Journal of chemical physics* 87.11 (1987), pp. 6364–6372.

[40] Tianhai Zhu and Weitao Yang. “Structure of the ammonia dimer studied by density functional theory”. In: *International journal of quantum chemistry* 49.5 (1994), pp. 613–623.

[41] Jennifer G Loeser et al. “Multidimensional hydrogen tunneling dynamics in the ground vibrational state of the ammonia dimer”. In: *The Journal of chemical physics* 97.7 (1992), pp. 4727–4749.

[42] M Havenith et al. “Measurement of the intermolecular vibration–rotation tunneling spectrum of the ammonia dimer by tunable far infrared laser spectroscopy”. In: *The Journal of chemical physics* 94.7 (1991), pp. 4776–4789.

[43] Michael J Frisch, John A Pople, and Janet E Del Bene. “Molecular orbital study of the dimers (AHn) 2 formed from ammonia, water, hydrogen fluoride, phosphine, hydrogen sulfide, and hydrogen chloride”. In: *The Journal of Physical Chemistry* 89.17 (1985), pp. 3664–3669.

[44] David M Hassett, Colin J Marsden, and Brian J Smith. “The ammonia dimer potential energy surface: resolution of the apparent discrepancy between theory and experiment?” In: *Chemical physics letters* 183.5 (1991), pp. 449–456.

[45] Jonathan Tennyson et al. “IUPAC critical evaluation of the rotational–vibrational spectra of water vapor. Part I—Energy levels and transition wavenumbers for H 2 17 O and H 2 18 O”. In: *Journal of Quantitative Spectroscopy and Radiative Transfer* 110.9 (2009), pp. 573–596.

[46] Jonathan Tennyson et al. “IUPAC critical evaluation of the rotational–vibrational spectra of water vapor. Part II: Energy levels and transition wavenumbers for HD16O, HD17O, and HD18O”. In: *Journal of Quantitative Spectroscopy and Radiative Transfer* 111.15 (2010), pp. 2160–2184.

[47] Jonathan Tennyson et al. “IUPAC critical evaluation of the rotational–vibrational spectra of water vapor, Part III: Energy levels and transition wavenumbers for H 2 16 O”. In: *Journal of Quantitative Spectroscopy and Radiative Transfer* 117 (2013), pp. 29–58.

[48] Jonathan Tennyson et al. “IUPAC critical evaluation of the rotational–vibrational spectra of water vapor. Part IV. Energy levels and transition wavenumbers for D 2 16 O, D 2 17 O, and D 2 18 O”. In: *Journal of Quantitative Spectroscopy and Radiative Transfer* 142 (2014), pp. 93–108.

[49] Piotr Skurski and Maciej Gutowski. “Theoretical study of the dipole-bound anion (H2O-NH3)-”. In: *The Journal of chemical physics* 108.15 (1998), pp. 6303–6311.

[50] Geoffrey Andrew Yeo and Thomas Anthony Ford. “Ab initio molecular orbital calculations of the infrared spectra of hydrogen bonded complexes of water, ammonia, and hydroxylamine. Part 6. The infrared spectrum of the water-ammonia complex”. In: *Canadian journal of chemistry* 69.4 (1991), pp. 632–637.

[51] GT Fraser and RD Suenram. “Perturbations in the infrared spectrum of the NH3 umbrella mode of HOH—NH3”. In: *The Journal of chemical physics* 96.10 (1992), pp. 7287–7297.

[52] J Sadlej et al. “Structure and Energetics of the Weakly Bound NH3-H2O Complex”. In: *The Journal of Physical Chemistry A* 103.42 (1999), pp. 8528–8536.

[53] Joseph R Lane, Veronica Vaida, and Henrik G Kjaergaard. “Calculated electronic transitions of the water ammonia complex”. In: *The Journal of chemical physics* 128.3 (2008), p. 034302.

[54] Andrew K Mollner et al. “Imaging the State-Specific Vibrational Predissociation of the Ammonia- Water Hydrogen-Bonded Dimer”. In: *The Journal of Physical Chemistry A* 113.38 (2009), pp. 10174–10183.

[55] Robert Moshammer and Reinhard Dörner. “Die ganze Welt aus Bruchstücken”. In: *Physikjournal* 14.8/9 (2015), pp. 61–64.

[56] unknown. *ALS photon source parameters*. 2015. URL: `https://www-als.lbl.gov/index.php/beamlines/photon-source-parameters` (visited on 01/30/2016).

[57] Roy Kaltschmidt. *Berkeley Lab’s Advanced Light Source and the San Francsico Bay Area*. 2015. URL: `http://photos.lbl.gov/viewphoto.php?imageId=28221209` (visited on 01/29/2016).

[58] unknown. *ALS beamclock*. 2015. URL: `https://www-als.lbl.gov/index.php/beamlines/beamlines-directory` (visited on 01/29/2016).

[59] Thorsten Weber. “Untersuchung der verschränkten Bewegung freier Elektronenpaare emittiert aus Ein-und Zweizentren Coulomb-Potentialen in Photoabsorptionsprozessen”. In: *Doktorarbeit. Frankfurt am Main: Johann Wolfgang Goethe-Universität* (2003).

[60] Wolfgang Demtröder. *Experimentalphysik 1–Mechanik und Wärme. 5. neu bearbeitete und aktualisierte Auflage*. 2008.

[61] David R Miller. *Free jet sources*. 1988.

[62] Matthias Hillenkamp, Sharon Keinan, and Uzi Even. “Condensation limited cooling in supersonic expansions”. In: *The Journal of chemical physics* 118.19 (2003), pp. 8699–8705.

[63] G Brusdeylins and HD Meyer. “Speed ratio and change of internal energy in nozzle beams of polyatomic gases”. In: *Rarefied Gas Dynamics*. Vol. 1. 1979, pp. 919–923.

[64] WC Wiley and Ii H McLaren. “Time-of-flight mass spectrometer with improved resolution”. In: *Review of Scientific Instruments* 26.12 (1955), pp. 1150–1157.

[65] unknown. *MCP Delay Line manual*. 2015. URL: `http://www.roentdek.com/manuals/MCP%20Delay%20Line%20manual.pdf` (visited on 02/03/2016).

[66] unknown. *Microchannel plate (MCP) detectors*. 2015. URL: `https://www.atom.uni-frankfurt.de/research/coltrims/mcp/` (visited on 02/02/2016).

[67] unknown. *THE RoentDek DELAY LINE DETECTOR WITH HEXANODE*. 2015. URL: `http://www.roentdek.com/info/Delay_Line/` (visited on 02/03/2016).

[68] O Jagutzki et al. “A broad-application microchannel-plate detector system for advanced particle or photon detection tasks: large area imaging, precise multi-hit timing information and high detection rate”. In: *Nuclear Instruments and Methods in Physics Research Section A: Accelerators, Spectrometers, Detectors and Associated Equipment* 477.1 (2002), pp. 244–249.

[69] unknown. *CoboldPC Software*. 2015. URL: `http://www.roentdek.com/software/software/` (visited on 02/03/2016).

[70] Felix Paul Sturm. “Photo and Auger Electron Angular Distributions of Fixed-in-Space CO2”. In: (2009).

[71] Ottmar Jagutzki et al. “Multiple hit readout of a microchannel plate detector with a three-layer delay-line anode”. In: *Nuclear Science, IEEE Transactions on* 49.5 (2002), pp. 2477–2483.

[72] M Lundqvist et al. “Doppler-free kinetic energy release spectrum of”. In: *Journal of Physics B: Atomic, Molecular and Optical Physics* 29.8 (1996), p. 1489.

[73] National Institute of Standards and Technology. *NIST Atomic Spectra Database*. 2016. URL: `http://www.nist.gov/pml/data/asd.cfm` (visited on 02/15/2016).

[74] Spas D Stoychev, Alexander I Kuleff, and Lorenz S Cederbaum. “On the intermolecular Coulombic decay of singly and doubly ionized states of water dimer”. In: *The Journal of chemical physics* 133.15 (2010), p. 154307.

[75] B Gaire et al. “Hydrogen and fluorine migration in photo-double-ionization of 1, 1-difluoroethylene (1, 1-C 2 H 2 F 2) near and above threshold”. In: *Physical Review A* 89.4 (2014), p. 043423.